2016

Shock Tube and Mid-infrared Laser Absorption Measurements of Ignition Delay Times and Species Time-histories

Batikan Koroglu
University of Central Florida

SHOCK TUBE AND MID-INFRARED LASER ABSORPTION MEASUREMENTS OF IGNITION DELAY TIMES AND SPECIES TIME-HISTORIES

by

BATIKAN KOROGLU

M.Sc. University of Nevada Reno, 2012

B.Sc. Middle East Technical University, 2010

A dissertation submitted in partial fulfillment of the requirements
for the degree of Doctor of Philosophy
in the Department of Mechanical and Aerospace Engineering
in the College of Engineering and Computer Science
at the University of Central Florida
Orlando, Florida

Spring Term
2016

Major Professor: Subith S. Vasu

ABSTRACT

Energy consumption has increased dramatically as the world advances and becomes more industrialized. Over the next twenty five years, the U.S. Department of Energy expects the energy demand to increase by 29% with majority of the new energy coming from natural gas (methane). Another promising fuel source for power generation and transportation is the biofuels. The biofuel use in the US is shown to have increased substantially in the last decade. There are serious environmental concerns associated with greenhouse (e.g. carbon-dioxide) and toxic gas emissions (e.g. nitrogen oxides and aldehydes such as propanal) due to deriving energy from natural gas and biofuel combustion. In this doctoral study, a shock tube experimental setup was designed, assembled, and tested in order to study the ignition as well as thermal decomposition characteristics of two types of fuels: methane (the major natural gas component, which is also a major intermediate during higher order hydrocarbon ignition and pyrolysis) and propanal (an oxygenated hydrocarbon found in the exhaust emissions of biofuels). A laser diagnostics using semi-conductor type laser diodes in the infrared region for measurements of methane and propanal gas concentrations was developed and used with the shock tube. This diagnostics also enabled the interference-free detection of methane during the course of propanal pyrolysis. The experimental measurements highlighted the areas in which refinement of reaction kinetic models was required. The current research provided information on the ignition delay times as well as concentration time-histories of fuels (e.g. propanal or methane) and intermediates (e.g. methane). The knowledge gained during this doctoral study is vital for the accurate modeling of emissions due to combustion of fuels.

The dissertation discusses the details of the four following items: 1) design, assembly, and testing of a shock tube setup as well as a laser diagnostics apparatus for studying ignition characteristics of fuels and associated reaction rates, 2) measurements of methane and propanal infrared spectra at room and high temperatures using a Fourier Transformed Infrared Spectrometer (FTIR) and a shock tube , 3) measurements of ignition delay times and reaction rates during propanal thermal decomposition and ignition, and 4) investigation of ignition characteristics of methane during its combustion in carbon-dioxide diluted bath gas. The main benefit and application of this work is the experimental data which can be used in future studies to constrain reaction mechanism development.

To my mom, dad, and brother

ACKNOWLEDGMENTS

First and foremost, it is with immense gratitude that I acknowledge the support and help of my advisor professor, Dr. Subith Vasu, for his steadfast encouragement. This study would not have been possible without his valuable insights and help. I also would like to thank to my dissertation committee members, Dr. Robert Peale, Dr. Jayanta Kapat, and Dr. Alan Kassab for their willingness to be in my thesis committee, their time and effort to serve on my dissertation.

I wish to thank my past and present lab mates Ghazal Barari, Zach Loparo, Kyle Thurmond, Owen Pryor, Bader Almansour, Joseph Lopez, Luke Thompson, and Leigh Nash for their valuable discussions throughout my doctorate study.

Last but not the least, I would like to thank my dear mother and brother for supporting me by all means throughout my life. Their spiritual encouragement always helped me overcome the hard times and complete my doctoral study. I would like to dedicate this dissertation to my beloved family including my dear late father.

TABLE OF CONTENTS

LIST OF FIGURES

LIST OF TABLES

CHAPTER 1: INTRODUCTION

1.1 Motivation

Biofuels, which are oxygenated hydrocarbons, are increasingly being used in combustion systems for power generation and transportation. The biofuel use in the US is shown to have increased from 3 million tons of oil equivalent (Mtoe) in 2004 to more than 25 Mtoe in 2010 [1]. On the other hand, there is a decreasing trend in the use of oil. Over the last decade, researchers have examined a variety of biofuels that could be readily blended with fossil fuels [2-5]. These oxygenated hydrocarbons are involved in the combustion of several fossil fuels either as additives or as stable intermediate species. There are various chemical species inherent in biofuels that have different functional groups, which could be, for example, alcohols, aldehydes, and alkyl esters. Some of these oxygenates are stable intermediates and can survive until the end of combustion and appear as pollutants at the exhaust [6]. In fact, due to the oxygenated emissions, the increased biofuel usage have been linked with increased photochemical smog, cancer mortality, and air pollution concerns [7-15] and could contribute to more than 2 million premature mortalities in the world every year [16]. Aldehydes, for instance, are being considered as regulated emissions in some regions of the world. Formaldehyde, acetaldehyde, acrolein, propanal, and butanone are the most common aldehydes at the exhaust emissions of biofuels that are included in the list of the hazardous air pollutants (HAP) by the United States Environmental Protection Agency (USEPA, 2012a) [17]. Also, formaldeyhde (CH_2O), acetaldeyhde (CH_3CHO), acrolein (C_3H_4O or C_2H_3CHO), and propanal (C_2H_5CHO) are reported to be the most abundant aldehydes in the exhaust emissions of biodiesel or diesel fuels [18].

Some studies showed a significant increase of emissions of these aldehydes with the use of biodiesel blends in diesel fuel [19]. On the other hand, some studies reported that all aldehyde emissions except for acrolein and formaldehyde decreased with the use of B2 to B100 (2 percent biodiesel to 100 percent biodiesel). The increase of acrolein, for example, was up to three folds with the use of 100 percent biodiesel [20]. Some studies pointed out this inconsistency of different studies and showed percent changes of emissions for various biodiesel blends derived from different sources such as rapeseed, palm oil, and food stock [21]. Also, some studies focused on diesel engine fuelled with diesel and ternary blends containing diesel, ethanol and biodiesel or vegetable oils. The use of 10 percent ethanol in diesel, for example, resulted in increases of formaldehyde (79%), acrolein (900%), propanal (29%), and acetaldehyde (30%), and various other carbonyl compounds [22]. Among these aldehydes there is a significant amount of increase (up to 9 folds) in the emission of acrolein with the use of biodiesel or ethanol and diesel blends. The acrolein emission increase by the use of biodiesel is attributed to the glycerol or glycerides in [22,23] because glycerides are formed during the transesterification process. The transesterification is the process of forming biodiesel (fatty acid methyl ester or fatty acid ethyl ester) through the reaction of triglycerides with an alcohol (methanol or ethanol).

There are several chemical kinetic studies [24-28] that compare the modeling and experimental results for the concentration of major and minor species of combustion of biofuel surrogates. Although the mole fraction profiles of major combustion reaction products (H_2O, CO_2, CO, etc.) as well as the hydrocarbons were reasonably approximated by these mechanisms, the modeling results for the aldehydes do not match with the experimentally obtained values. In

addition, the diagnostic methods used in some studies cannot distinguish between acrolein and propanal and thus reports their concentration results as a sum.

The study by P. A. Glaude et al. [24] investigates the oxidation kinetics of methyl decanoate, n-decane, and n-hexadecane in a jet stirred reactor and compares the experimental data with simulation results obtained from the CHEMKIN PRO [29] (Perfectly Stirred Reactor) PSR model. It was noted in this study that, during the combustion of methyl decanoate, the oxidation of esters leads to the formation of hydroperoxide. The decomposition of hydroperoxide unsaturated methyl esters ($C_nH_{(2n\_2)}O_4PZS$) leads to the formation of acrolein (C_2H_3CHO), an _OH radical, and a $\_C_{(n\_3)}H_{(2n\_7)}O_2S$ ester alkyl radical. Although the kinetics model of methyl deconate given in [24] shows a good match for acetaldehyde between the experiment and model results, there is a big difference for the other aldehydes; namely, propanal and acrolein. It is also important to note here that the concentration results are given for the sum of acrolein and propanal because of not being able to experimentally separate their mole fractions with the use of a gas chromatograph. As a result, the modeling and experimental results were compared for the sum of acrolein and propanal.

Another study that shows the experimental and model results discrepancies is conducted by J. Biet et al. on the oxidation of n-decane and a 65% (mol) n-decane/35% n-hexadecane blend in a jet-stirred reactor at atmospheric pressure between temperatures of 550 and 1050 K [25]. The mole fraction profiles are shown in the study for the reactants and the main light products; namely, carbon oxides, methane, ethylene, ethane, propene, acetaldehyde, and C3 aldehydes. The propanal and acrolein could not be distinguished with the used gas chromatographic method. The comparison of experimental and computed profiles of speciation

was shown for the oxidation of n-decane in a jet-stirred reactor at atmospheric pressures and stoichiometric mixtures containing in helium bath gas. It was seen that the production of acetaldehydes was well simulated above 800 K, but considerably overestimated below 750 K. The formation of C3 aldehydes was overestimated both below 750 K and above 800 K. The simulation indicated that below the NTC zone, propanal, which was obtained by decomposition of keto hydroperoxides, was the major C3 aldehyde.

Although the mole fraction profiles of major combustion reaction products (H_2O, CO_2, CO, etc.) as well as the hydrocarbons were reasonably approximated by these mechanisms, the modeling results for the aldehyde profiles did not match the experimental values. Even though there are recent laser absorption schemes in the literature such as given in [30], which is developed through shock tube kinetic studies for the detection of the formaldehyde and acetaldehyde, there are very few studies on the acrolein detection through laser absorption diagnostics [31,32], and none for propanal. These studies on the acrolein detection were conducted with two lead-salt tunable diode lasers with emissions at 958.8 cm^{-1} and 891.0 cm^{-1} for the simultaneous measurement of acrolein and 1,3-butadiene, respectively, in each puff of mainstream cigarette smoke in real time. There is no study on the interference free detection of acrolein or propanal in a combustion environment.

Due to the considerable discrepancies between the model and experiment results, the aforementioned studies suggest investigating the reactions involving the aldehydes and determining the reaction rates correctly to input these data into the models so that more accurate representation of the experimental data by models can be achieved. It is important to understand the formation and destruction pathways of the aldehydes in combustion and atmospheric systems

because these chemicals are carcinogenic and/or toxic. The shock tube experiments with line-of-sight laser absorption detection schemes are intended to be carried out to obtain an interference free absorption and thus mole fraction measurements of propanal. Since the aldehydes have the same carbonyl functional group (C=O carbonyl group with C-H bond), the absorption transitions for these molecules occur around similar spectral ranges; namely, the transitions occur between 1710 and 1740cm^{-1} wavenumbers due to the (C=O) vibrational stretching and between 2690-2840cm^{-1} due to the common (C-H) bond.

In this dissertation the ignition delay time characteristics of methane in carbon-dioxide diluted gas mixtures is also investigated using the mid-infrared laser diangostics. Over the next twenty five years, the U.S. Department of Energy expects the energy demand to increase by 29% with almost all of the new energy from natural gas [33]. A problem is that current methods for the combustion of natural gas result in large amounts of CO_2 and NO_x emissions. In order to reduce the greenhouse gases, one possible solution is the oxy-methane combustion with large CO_2 dilution. By using pure oxygen instead of air, resulting products can be reduced to mainly CO_2 and H_2O. CO_2 can then be captured and returned to the combustor to dilute the mixture again or store underground. The major concern with this nascent technology is the difference in methane oxidation in air vs CO_2 diluted mixtures. It has been shown that the reactions behave differently as the properties of nitrogen and carbon-dioxide differ [34] in terms of participation in combustion reactions directly or as a third-body collision partner. As a result, more analysis of oxy-methane combustion with high CO_2 addition needs to be conducted.

There are some studies of CO_2 diluted oxy-methane combustion in the literature. Heil et al. investigated the methane burning rates for flameless combustion and compared the results to

nitrogen diluted mixtures [35]. Di Benedetto et al. and Liu et al. looked at the chemical effects (flammability and burning velocity) of methane combustion in CO_2 versus N_2 [36,37]. The laminar flame speeds have also been studied for various conditions [38-41]. In addition, Vasu et al. examined the effect of CO_2 dilution on the ignition delay times of syngas mixtures of hydrogen and carbon monoxide [42]. However, there are very few studies in the literature that probed the effects of excess CO_2 dilution on the ignition delay times of methane. Holton et al. conducted ignition delay time measurements of natural gas blends, including methane and ethane mixtures, with small amounts of CO_2 addition (5 and 10%) [43]. They found out that methane and ethane blends at $\Phi = 0.5$ and T=1137 K diluted with 5% CO_2 increased the ignition delay time by only 2%, whereas 10% CO_2 addition to the same mixture resulted in longer times by 46% . This increase was attributed to the third-body collision efficiencies of CO_2 being an order of magnitude greater than those of N_2. However, they suggested carrying out further experiments in order to better quantify the effect of CO_2 addition on the ignition delay time.

1.2 Scope and Organization of Dissertation

Chapter 2 includes the theory behind the use of a shock tube to study the combustion reactions and the design considerations for the shock tube experimental setup based on the literature review. Chapter 3 gives information on the shock tube experimental setup, which was designed and assembled at the University of Central Florida by the current author during his doctorate study at UCF. The assembly stages of the shock tube as well as information on its various components, such as its sensors and other auxiliary equipment, are also mentioned.

Chapter 4 lists information on a Fourier Transform Infrared Spectrometer, which is an experimental setup that was used to record the spectra of the aldehyde called propanal. Chapter 4 also provides the details of the propanal spectral features with regard to its vibrational transitions. After that Chapter 5 continues with the infrared absorption spectra of propanal and methane at high temperatures (1200 < T < 2000 K). Also, the concentration time-histories of methane and propanal during propanal pyrolysis by means of interference-free line of sight laser absorption diagnostics behind reflected shock waves were measured at 1 atm and temperatures between 1200 and 1400 K. These experimental results were compared to three different reaction mechanisms developed specifically for aldehyde pyrolysis and ignition; namely, POLIMI [44], NUIG [44], and McGill [6] mechanisms.

In Chapter 6 the ignition delay time measurements for mixtures of CH_4, CO_2, and O_2 in argon bath gas at temperatures between 1577 and 2144 K and pressures between 0.5-4 atm, were shown and discussed. Experimental data were compared to the predictions of two kinetic models: GRI 3.0 and AramcoMech 1.3 mechanisms [45,46]. The ignition delay time measurements showed the influence of CO_2 dilution on the oxidation of methane. Chapter 7 compares the absorption cross section values of methane measured at two different wavelengths (λ_{peak} = 3403.4 nm and λ_{valley} = 3403.7 nm) with three non-reactive gas mixtures: 2% CH_4 in argon and 2% CH_4 in argon diluted with 30% CO_2, and 2% CH_4 in CO_2. Present experiments were performed behind the reflected shock waves at high temperatures (1200 < T < 2000 K) and around atmospheric pressures (0.7 < P < 1.5 atm).

Chapter 8 gives the conclusions of the main findings of this doctoral study in regards to the ignition and thermal decomposition characteristics of propanal and methane. In addition, the

papers published during this doctoral study [47-50] are listed. Finally, recommendations for future work are summarized.

CHAPTER 2: SHOCK TUBE THEORY

A shock tube is an ideal tool for studying physical and chemical processes at high temperatures, because it can bring the test gas to predetermined temperatures and pressures almost instantaneously and keep the gas at steady conditions for a few milliseconds. The test gas inside the shock tube might be investigated by optical or other methods along its length so that the progress of chemical reactions and physical processes can be followed during the course of the experiment. Figure 2.1 shows a typical shock tube setup that consists of high and low pressure sections, which are referred to as the driver and driven sections, respectively. A diaphragm separates these two regions and a normal shock wave is created by a sudden rupture of the diaphragm. After the diaphragm rupture a shock wave forms and moves into the driven section, while an expansion fan propagates into the driven section. The shock tube can be divided into five main regions as shown in figure 2.1

The change in the static pressure, temperature, and density across a normal shock wave can be determined from the continuity, momentum and energy conservation equations. The derivation of the ideal shock relations is given in [51]. The equation relating the strength (Mach number) of the shock wave to the initial pressure ratio across the diaphragm is given by

$$\frac{P_4}{P_1} = \frac{2\gamma_1 M_s{}^2 - (\gamma_1 - 1)}{\gamma_1 + 1}\left[1 - \frac{\gamma_4 - 1}{\gamma_1 + 1}\frac{a_1}{a_4}\left(M_s - \frac{1}{M_s}\right)\right]^{-\left(\frac{2\gamma_4}{\gamma_4 - 1}\right)} \qquad (2\text{-}1)$$

where $[M_s]$ is the Mach number of the shock wave, $[P_4 / P_1]$ is the ratio of driver and driven sections pressures, and $[\gamma_1]$ and $[\gamma_4]$ are the specific heat ratios, $[a_1]$ and $[a_4]$ are the speeds of sound in the driven and driver sections, respectively. Therefore, the strongest shock

waves are obtained as the initial pressure ratio goes to infinity [$P_4 / P_1 \to \infty$], in which case [$M_s \to \frac{\gamma_1 + 1}{\gamma_4 - 1}\frac{a_4}{a_1}$]. As a result, the strength of the shock wave increases as the driver gas has a higher speed of sound and a lower specific heat ratio. Thus, low density gasses such as helium or hydrogen are used in the driver section for a shock tube experiment.

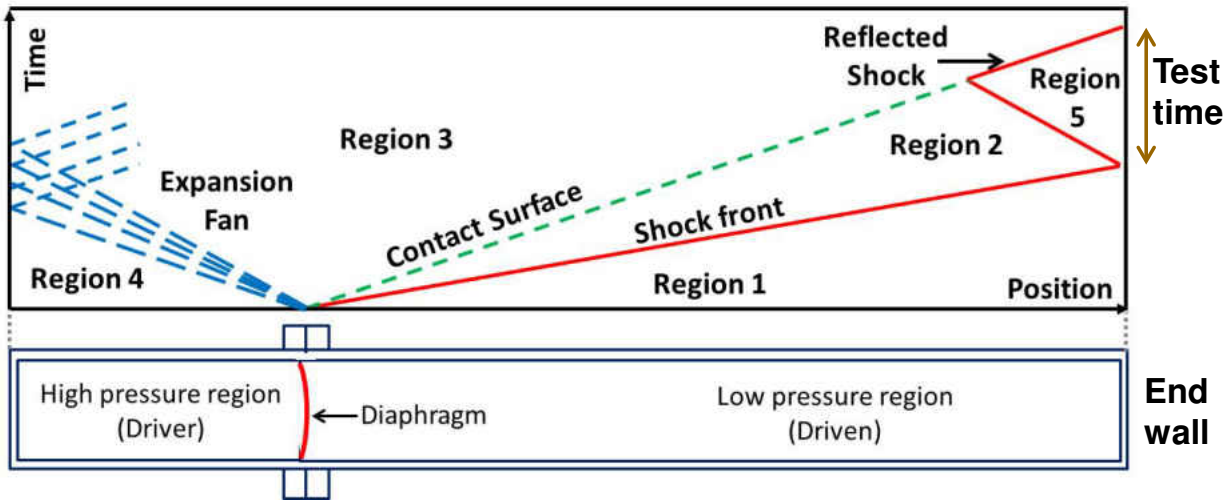

Figure 2-1- A shock tube experimental setup

As the shock wave moves through the quiescent gas in region 1, the gas is compressed. This compression results in an increase in the gas temperature, pressure and density in region 2. Also, the propagation of the incident shock wave imparts to the gas in this region a velocity. However, the gas in region 1 is still stationary until the shock wave hits the end wall. After a normal shock reflection from the end wall of the shock tube, the gas velocity must be zero again. Therefore, the gas gives up all of its kinetic energy on passing through the shock front into the reflected shock region referred to as the region 5, thus raising the temperature and pressure of the gas in region 5 over those in region 2. The reflected shock region contains a static gas at high

temperature, density, and pressure. This state continues until the reflected shock meets the oncoming contact surface. The temperature and pressure of the gas in the reflected shock region (region 5) can be determined from the knowledge of the gas properties in region 1 as follows

$$\frac{P_5}{P_1} = \left[\frac{2\gamma M_s^{\,2} - (\gamma - 1)}{\gamma + 1} \right] \left[\frac{(3\gamma - 1) M_s^{\,2} - 2(\gamma - 1)}{(\gamma - 1) M_s^{\,2} + 2} \right] \tag{2-2}$$

$$\frac{T_5}{T_1} = \frac{\left(2(\gamma - 1) M_s^{\,2} + (3 - \gamma)\right)\left((3\gamma - 1) M_s^{\,2} - 2(\gamma - 1)\right)}{(\gamma + 1)^2 M_s^{\,2}} \tag{2-3}$$

where the specific heat ratios are assumed to be constant. Detailed derivation of the above equations is provided in [51].

CHAPTER 3: SHOCK TUBE EXPERIMENTAL SETUP

3.1 Introduction

There are many applications of the shock tube experimental setup in chemistry, physics, and engineering. The measurement of ignition delay time is one of them. The ignition delay time is one of the key parameters used in characterizing the auto ignition of a specific fuel and oxidizer mixture. A shock tube suits well for measuring the ignition delay time as it brings the fuel and oxidizer mixture to the desired experimental conditions almost instantaneously and it also enables the control of temperature and equivalence ratio of the mixture independently. In addition, applying the knowledge of spectroscopy in the field of combustion by means of shock tube experiments has served as a valuable tool for determining the concentration of chemical species and thus reaction rate coefficients [30,52,53].

3.2 The Design Considerations in Manufacturing a Shock Tube

The test gas in the driven section of the shock tube can be brought to the desired high temperature and pressure conditions by means of the reflected shock wave. One of the most important design parameters is the time during which measurements can be made behind the reflected shock wave on the test gas at these elevated conditions. This depends on the driver and driven section lengths as well as the initial conditions. Long shock tubes are favorable for obtaining longer test times. However, this does not mean that a tube of sufficient length will enable any test time desired. The main reason is that the rarefaction waves will reach the contact surface after being reflected from the end wall of the driver side. This will cause the decay of the

incident shock wave. The reason why the rarefaction wave reaches the contact surface is that the rarefaction wave, after being reflected from the driver section's end wall, will move in the same direction as the flow of the gas expanding into the driven section. Therefore, the rarefaction wave will move with the sum of the local sound speed and particle speed (a_3+v_3). However, the contact surface moves at a speed of v_3. As a result, the reflected rarefaction wave will catch up with the contact surface. The rarefaction waves would always be transmitted through the contact surface and arrive in the region 2 and eventually result in the shock wave to decay. Therefore, the test time would be limited by the arrival of the reflected head of the rarefaction wave at the contact surface.

If the driven section is not too long or the driver section is not too short, then the incident shock wave would be reflected from the driven section's end wall before it is overtaken and decayed by the reflected rarefaction wave. After that, the reflected shock will collide with the oncoming contact surface. Therefore, the test time is defined as the time interval between the arrival of the reflected shock wave at the measuring position and the arrival of pressure waves at the same position resulting from the interaction of the reflected shock wave with the contact surface as shown in Figure 2-1. The interaction of the contact surface and the reflected shock wave can result in three possible outcomes. In each case, a shock would be transmitted into region 3; however, the reflected wave might be a shock, rarefaction or Mach wave depending on the values of the a_2 and a_3. [51,54]. A special case occurs when a_2 is equal to a_3. In this case, the reflected shock passes through the contact surface and the contact surface comes into rest. A highly improved test time is obtained in this case because the elevated region 5 conditions persist until the rarefaction wave from the driver section's endwall arrives at the interface. This

condition is called the tailoring condition and it is obtained by matching the acoustic impedance between the driver gas and the shocked gas [55]. Very long test times have been reported in the literature. For example, 25ms of test time was obtained with the use of 40% Nitrogen in Helium by using 7.12 m driver and 8.54 m driven sections with region 5 temperature of 1000K, whereas only 2 ms of test time was able to be obtained with pure Helium by using 3.35 m long driver and 8.54 m driven sections. The shock tube used had 14.13cm inside diameter [56].

There are non-idealities involved in a shock tube experiment. A boundary layer is formed behind the incident shock wave due to viscous effects [57-61]. After the reflected shock wave moves into this flow field and comes into contact with the growing boundary layers, changes in pressure at this region occur that penetrates into the reflected shock region. As a result, increases of pressure and temperature have been observed during the ignition delay time measurements. This results in uncertainties in the ignition delay time measurements, because the slight pressure and temperature increases occurring during the pre-ignition process cause acceleration in the ignition, leading to shorter ignition delay times than the actual values. For example, 7 ms of difference in ignition delay time in the oxidation of propane has been reported by Lam et al. [56]. To eliminate this boundary layer effect, use of larger diameter shock tubes are suggested because boundary layer would be small compared to the bulk test gas inside the shock tube. Heufer and Olivier [54] used 140mm inside diameter shock tube and obtained much smaller pressure and temperature increases (2% P&T gradient) compared to an earlier study by Petersen et al. [62] (%12 P&T gradient) in which a 50mm diameter shock tube was used. Note that the boundary layer effects also result in the incident shock wave to decelerate and the contact surface to accelerate, leading to shorter test times.

There are other design aspects required to be taken into account before manufacturing a shock tube. Stotz et al. [63] explains some of these details in their design of the double diaphragm shock tube. A special vacuum valve was used between the vacuum line going to the rotary vane pump and the shock tube. The valve was machined in such a way that it completely matched the inner contour of the shock tube. This design was used so that the shock wave propagation would not be perturbed. In addition, Stotz et al. [63] used diaphragms which were scored on their surface with grooves to facilitate the diaphragm rupture as well as to make sure that the diaphragms open cleanly without any jagged edges. A similar diaphragm design was used by Tranter et al. [64] for a shock tube used for chemical kinetic investigations. They additionally made a small cut into the driven section's wall so that the petals of the diaphragm, after the diaphragm rupture, bend into this small cut. In this way, the petal was prevented to bounce back off the shock tube wall. Furthermore, they used conflat type flanges (CF) which utilize metal gaskets in between. These flanges make use of a sharp edge machined on the flange surface that bites into the metal gasket to form a high vacuum sealing. The conflat flanges are leak proof to 10^{-9} Torr of pressure based on the helium leak detector test results. The evacuation of their shock tube was done by means of a turbo molecular pump and a rotary pump. The vacuum pressure they were able to go down to was 1 mTorr. Similar and even lower vacuum pressure values have been reported for other shock tube studies. An ultimate vacuum of 0.5mTorr was obtained for an aerosol shock tube [65]. Vasu et al. reported in their jet fuel ignition delay time measurements that before the test mixtures were introduced into shock tube, they vacuumed the tube down to 10^{-5} Torr at a leak rate of 10^{-4} Torr/min by using a turbo molecular pump together with a rotary vane pump [66]. These vacuum levels point out the

importance of having a clean shock tube experimental setup. In fact, due to similar reasons, Herbon [67] mentioned in his dissertation that electro-polishing of the shock tube was applied to passivate the inner surface of the shock tube.

A shock tube setup usually makes use of piezoelectric pressure transducers which are capable of measuring high speed fluctuations. Usually five of these transducers are placed at certain distances along the length of the tube to accurately measure the shock speed. These transducers are connected to time interval counters. Based on the time intervals and the pressure transducer spacing, the shock velocity can be determined. The obtained shock speed is then substituted into Eqs. (2-2) and (2-3) to find out the pressure and temperature in the reflected shock region [17]. The details of the shock tube experimental setup at UCF are given in section 3.3.

3.3 Shock Tube Experimental Setup at UCF

The aforementioned studies [30,52,53] show the importance of using a shock tube as well as the knowledge of spectroscopy for developing interference-free laser absorption schemes for detecting species of interest in combustion applications. During the course of this doctoral study, similar laser absorption detection schemes were developed and utilized for detecting methane and propanal. These schemes were implemented using the shock tube setup designed and assembled by the current author during his doctorate study at UCF.

A high-purity, kinetics shock tube experimental setup was designed and built by means of six stainless steel pipes with inside and outside diameters of 14.17 and 16.8 cm, respectively. The driver and driven sections lengths are 4.88m and 8.54m, respectively. The inside surface of

the driven section was electro-polished. There are three important parts of the shock tube: the diaphragm, end wall test and tee sections. The diaphragm section separates the high pressure driver side from the low pressure driven side. The test section of the shock tube is located at the end wall of the driven section of the shock tube. This part accommodates total of 8 ports which are mainly to be used for optical access or for other sensors such as the pressure transducers. These ports are located 2cm away from the end wall of the driven section. These ports serve as the measurement location behind the reflected shock wave. All of these ports are opposing each other for the purpose of line of sight laser measurements. As well, there are two additional ports located at 10cm for other measurements, for example, determining initial fuel concentration or measurements behind incident shock waves. The tee section of the shock tube is dedicated for vacuuming the driven section.

Figure 3-1 shows the schematic of the tee section of the shock tube. There is a 5-way cross with CF type flanges connected to the tee section. This entire section uses either CF or KF type flanges due to their ultra-high vacuum ratings. The first flange of the 5-way cross is connected to a gate valve that is controlled pneumatically with a solenoid valve. The gate valve is connected to a turbo molecular pump (Agilent model V301). The turbo pump is backed up by a rotary vane pump (Agilent DS102). The second flange of the 5-way cross is connected to a linear feedthrough (MDC Vacuum 661052). The feedthrough is connected to a valve. The valve surface has a contour that is machined to match the inside surface of the shock tube. The feedthrough is also actuated pneumatically with a solenoid valve. When the feedthrough is actuated, the contour valve closes the tee section opening that goes to the shock tube. This valve has a contour to prevent any perturbation when the shock wave propagates through the tube.

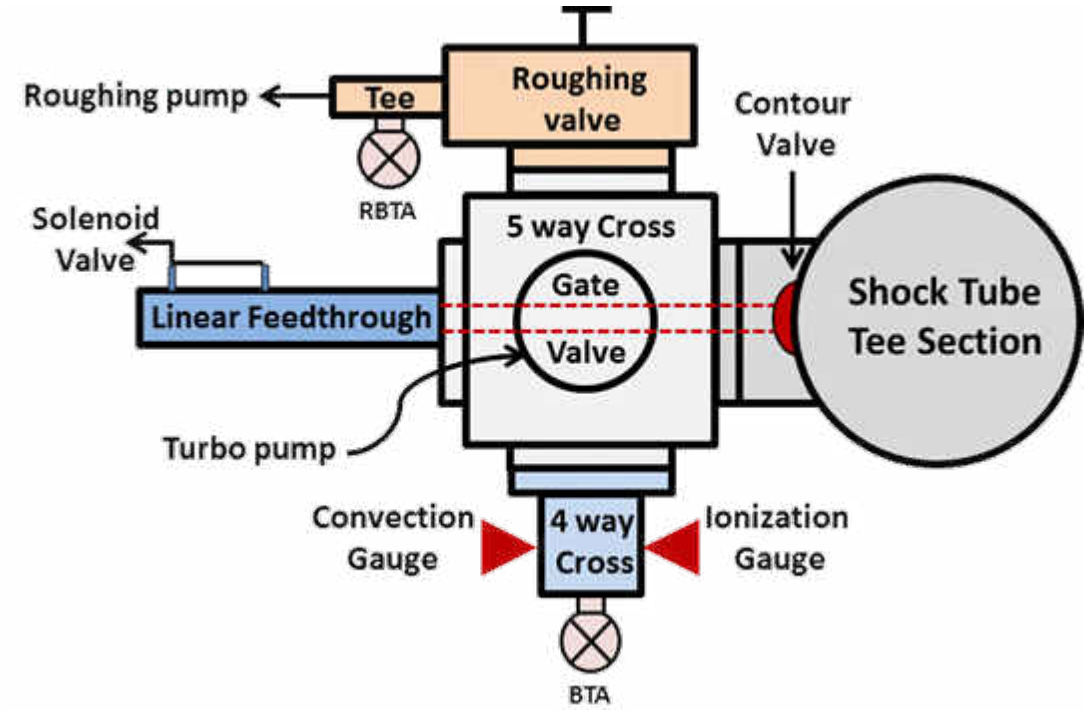

Figure 3-1- The schematic of the tee section of the shock tube used for vacuuming the setup

The third flange of the 5-way cross is connected to a 4-way cross, which has an ionization gauge (Lesker KJLC354401YF), convection gauge (Lesker KJL275804LL), and a valve (BTA) attached. The convection gauge is capable of measuring pressures between $1x10^{-4}$ and 1000 Torr. The ionization gauge is applicable for measuring pressures between $1x10^{-9}$ and $5x10^{-2}$ Torr. The valve is used to expose the 5-way cross to atmospheric pressure after each shock tube test so that any pressure differential across the contour valve can be eliminated. Therefore, it is named as the back-to-air (BTA) valve. The fourth flange of the 5-way cross is connected to another tee connection. This tee connection has a similar purpose back-to-air valve, an ultra-high vacuum roughing line valve, and a roughing pump (Agilent DS102). Before the gate valve can be opened to allow the turbo pump to vacuum the shock tube, the roughing pump should bring the pressure low enough for the proper operation of the turbo pump, which is

normally around $1x10^{-3}$ Torr. Note that the convection gauge is used for this pressure measurement. After that, the gate valve is opened and the turbo molecular pump vacuums the shock tube. At this point, the ionization gauge can be operated to make the low pressure measurements. The ionization gauge should not be exposed to pressures higher than $5x10^{-2}$ Torr during its operation; otherwise, its filament will break down.

The six pipes of the shock tube have flanges welded on them and the sealing between them was ensured by means of o-rings. The vacuum tests were carried out to determine the minimum pressure level of the driven section. It was seen that the roughing pump was able to bring the shock tube driven section pressure down to $5x10^{-3}$ Torr. After the operation of the turbo pump, the pressure was further decreased to $1x10^{-5}$ Torr. The leak rate was determined to be $1x10^{-5}$ Torr/min. Note that similar vacuum levels were obtained by Refs. [65,66] (see chapter 2). Furthermore, the driver section of the shock tube has to be capable of keeping the high pressure gas without any significant amount of leak. Therefore, a high pressure test was applied to the driver side and it was seen that the leak rate was $1.2x10^{-2}$ Torr/min. This leak rate was sufficiently good for the driver section.

3.3.1 Shock Velocity Measurements

The shock velocity measurement plays a crucial role in determining the properties (T_5 and P_5) of the test gas behind the reflected shock waves because these properties are directly related to the shock Mach number. Five piezoelectric pressure transducers (PCB 113B26) are placed along the shock tube to monitor the normal shock wave passage and thus to measure the shock speed. These transduces are capable of measuring high-speed fluctuations but they cannot

measure DC or constant pressure. They are located 30.5cm distance apart from each other. Four time-interval counters (Agilent 53220A) with 0.1ns time resolution are connected to PCB pressure transducers to obtain the time elapsed between the shock passages. The shock speed is determined from the time interval values as wells as the known distances between each transducer. What is critical for determining the reflected shock parameters (T_5, P5) is the incident shock velocity at the endwall, which can be determined from linear extrapolation. Furthermore, another piezoelectric pressure transducer (Kistler 603B1) is located at the end section of the shock tube to give the pressure trace during the course of the experiment. Since this pressure transducer is located at 2 cm away from the end wall, one of its main purposes is to determine the ignition delay time. An 8 channel analog input data acquisition board (NI PCI-6133) capable of making measurements at 2.5 MS/s/ch is available for measuring the pressure traces. The DAQ is also used with a laser placed at the end section of the shock tube for measuring methane and propanal concentration time histories.

The shock tube theory was described in Chapter 2. A shock wave is produced by raising the pressure in the driver section until the diaphragm bursts, sending a normal shock wave down the shock tube into the driven section and simultaneously sending an expansion wave into the driver section. Diaphragms of various thicknesses are required to change the pressure ratio [P_4 / P_1] across the driver and driven sections. In this way, shock waves at different Mach numbers can be obtained. Polycarbonate diaphragms having 0.005 and 0.020 inch thicknesses were used in the current work.

3.3.2 Fuel/oxidizer Mixture Preparation

The test gases for the experiments were prepared in a 0.033 m^3 teflon-coated stainless steel high purity mixing facility. Different mixtures were created manometrically and then mixed overnight with a magnetically driven stirrer to ensure homogeneity. Pressures were measured using a 100 Torr (MKS Instruments/Baratron E27D, accuracy of 0.12% of reading) and 10,000 Torr (MKS Instruments/Baratron 628D, accuracy of 0.25% of reading) full scale range capacitance manometers. Research grade argon (99.999%), helium (99.999%), oxygen (99.999%), carbon dioxide (99.999%), and methane (99.99%) were supplied by Air Liquide. High purity propionaldehyde (>99.6%), supplied by Fisher Scientific, was also used in this study. The prepared test mixtures were introduced into the electro-polished driven section of the shock tube before the experiments were conducted.

3.3.3 Test Time Measurements

The test time during which measurements behind the reflected shock waves can be conducted is an important parameter. At low temperatures (around 1000K) ignition delay times longer than 10ms have been reported [56]. Therefore, it is important to have sufficient amount of test time to determine the ignition delay time of the fuels. The test times can be estimated from the shock tube simulation program KASIMIR. [54,68]. This program assumes one dimensional and inviscid flow. It involves equilibrium real-gas effects such as the vibrational excitation. The initial conditions and the gas composition in the driver and driven sections were inputted to obtain the test times. Initially, the shock speed [v_s], driven pressure [P_1], driven temperature [T_1], and driver temperature [T_4] have to be input the software to determine the driver pressure, [P_4],

and the temperature and pressure in the reflected shock region [P_5] and [T_5], respectively. The driver gas can be taken as helium and the [T_1] and [T_4] are usually taken as the room temperature. An iterative approach is followed in which the desired T_5 and P_5 are to be obtained based on the chosen input parameters. Therefore, the shock velocity which results in the desired T_5 should first be determined. After that, the P_1 that gives the desired P_5 is determined because these two pressures are related to the shock speed through Eq. (2-2).

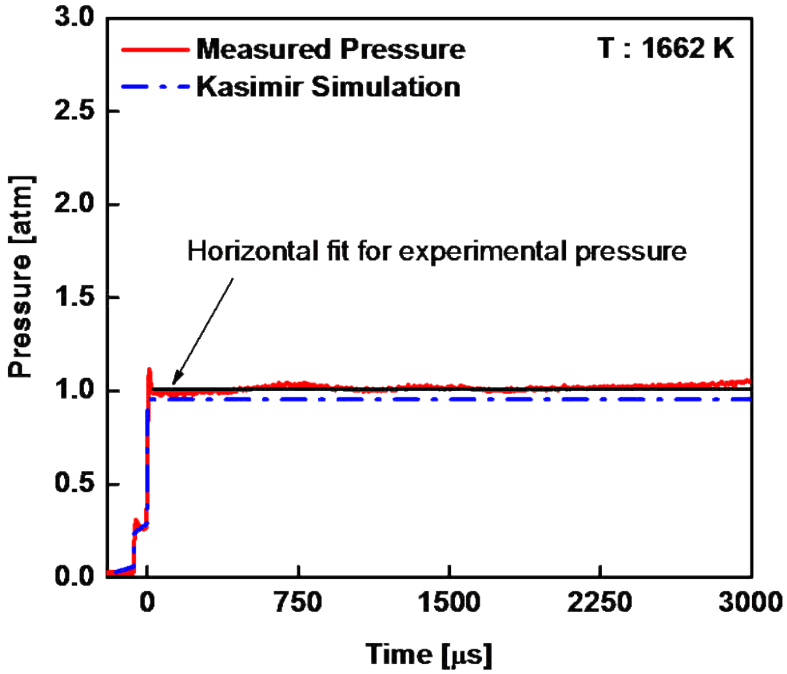

Figure 3.2 The comparison of measured and KASIMIR simulated pressure for reflected shock conditions of T = 1662 K and P ~ 1.0 atm. The experimental test time was more than 3000 μs. The driver and driven gasses were helium and argon, respectively.

Figure 3.2 provides the comparison of the measured and simulated pressure for reflected shock conditions of T = 1662 K and P ~ 1.0 atm. The driver and driven gasses were helium and argon, respectively. The experimentally obtained test time was more than 3000 μs. The experimental result of the pressure in the reflected shock region matched well with the

simulation result obtained from KASIMIR. Due to the boundary layer effects the incident shock wave decelerated (shock attenuation) and the contact surface accelerated which was mainly the reason for the experimental test times being shorter than the simulated ones. Also, since the contact surface is not a sharp discontinuity, multiple pressure waves are reflected at the contact surface as a result of the interaction with the reflected shock wave. This results in a small pressure increase instead of a sharp step as shown by the KASIMIR simulation [54]. Furthermore, the diaphragm rupture and shock formation in reality is not instantaneous as assumed in KASIMIR. However, the horizontal fit shown in Figure 3.2 indicates that the non-ideal shock tube effects did not cause the experimental pressure to rise dramatically with time ($dP_5/dt \sim 0$) during the tests because of the large diameter of the current shock tube employed (hence minimizing boundary layer influences). Hence driver inserts [69] were not used in the current study.

3.3.4 Ignition Delay Time Measurements

The ignition delay time was defined as the time interval between the arrival of the reflected shockwave and the onset of ignition at the measurement location (2 cm away from the end wall), which were determined from the pressure (or laser schlieren spikes) and emission measurements, respectively. The schematic is shown in Figure 3.3. The emissions were measured using a GaP transimpedance amplified detector (Thorlabs PDA25K) operating in the wavelength range between 150 and 550 nm. A band pass filter at 430 ±2 nm (Thorlabs FB430-10) for detecting the ($A^2\Delta$-$X^2\Pi$) transitions of the CH* radical was placed between a variable Slit (Thorlabs VA100/M) and the detector. The slit size was set to 1mm aperture for achieving

adequate time resolution. The onset of ignition from the CH* emission history was determined by finding the time of steepest rise and linearly extrapolating back in time to the pre-ignition baseline. This method was already described in a previous study of Vasu et al. [66].

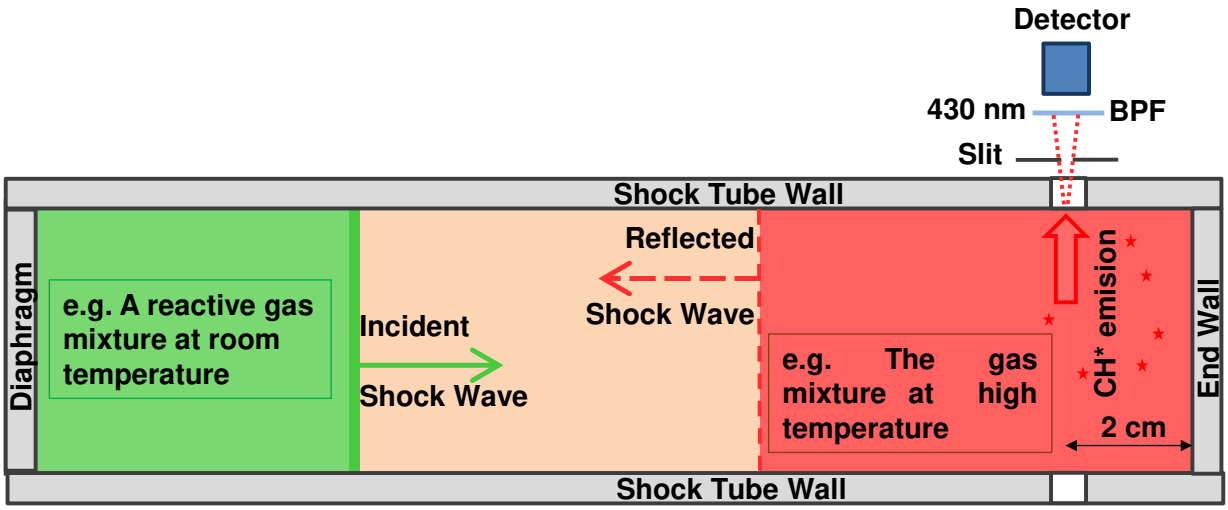

Figure 3.3 The setup for the ignition delay time with UCF shock tube

3.3.5 Concentration Time-history Measurements

One of the most important applications of the shock tube is the use of gas spectroscopy to determine the concentration of chemical species of interest. The theory behind the gas spectroscopy is given in chapters 4 and 7. In this doctoral study, shock tube chemical kinetic experiments with methane and propanal were carried out. The hydrocarbons share the same CH_2 or CH_3 structural groups which give rise to vibrational transitions around 3.4µm wavelength [70,71]. In the present study, a distributed feedback interband cascade laser at 3403 nm with +/- 2nm tunability (Nanoplus DFB ICL) was used.

The end section of the shock tube with the laser and the optical components are shown as a schematic in Figure 3.4. A continuous wave distributed feedback inter-band cascade laser

(Nanoplus DFB ICL) was collimated using a lens (Thorlabs C036TMEE) and a laser beam profiler (Spiricon Pyrocam-III). The laser diode was mounted on a heat sink (Nanoplus TO66 mount) which was also connected to temperature (Thorlabs TLD001) and injection current (Thorlabs TTC001) controllers. A wavelength meter (Bristol 771 Spectrum Analyzer) was used to determine the variation of the output wavelength with temperature and current settings. The laser beam was split into two parts; a reference beam (I_o) and the transmitted light (I) that passes through the shock tube. Each beam was incident on a focusing mirror (Thorlabs CM254-050-P01), which helped minimize the beam-steering effects. Two thermoelectrically cooled HgCdTe (MCT) detectors (Vigo Systems PVI-2TE-3.4) were used. A fixed wavelength laser absorption measurement conducted in this study used the vacuum measurement to report the I_o value. The transmitted beam was passed through an iris (Thorlabs ID25), neutral density filter (Thorlabs NDIR10A), and band pass filter (Thorlabs FB3500-500) to attenuate and minimize the interference on the detectors due to emission of gas species at high temperatures.

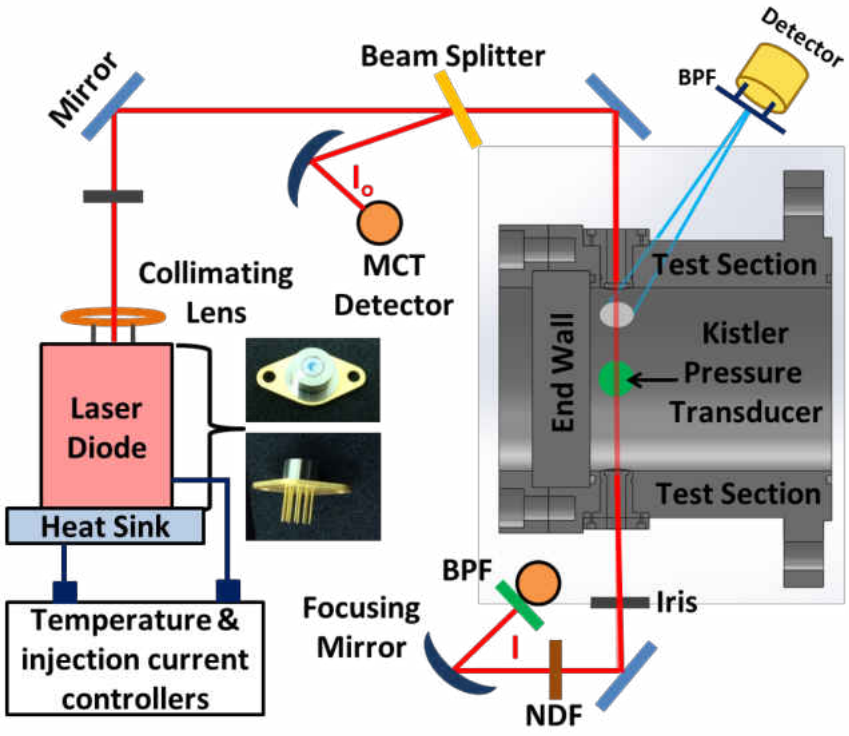

Figure 3.4 The setup for the laser absorption measurements in a shock tube

CHAPTER 4: FTIR MEASUREMENTS OF PROPANAL ABSORPTION CROSS-SECTIONS AND BAND STRENGHTS

4.1 Introduction

Critical to the development of laser absorption diagnostics is the accurate characterization of the absorption features of chemical species of interest. The absorption cross section of acrolein, propanal, and acetaldehyde are available in the PNNL database [72] at atmospheric pressure and at three different temperatures (5, 25, and 50^{o}C). The formaldehyde spectrum can be obtained from the HITRAN database [73]. Figure 4.1 (a) and (b) show the spectra for these four aldehydes at 296K in 1650-1850cm^{-1} and 2600-3100cm^{-1}, respectively. These four aldehydes share the same carbonyl group (C=O) vibrational stretching which gives rise to the absorption transition between 1710 and 1740cm^{-1}. In addition, the common (C-H) bond found in the aldehydes results in transitions between 2690-2840cm^{-1}. During combustion of fuels, other major species also form and they also have absorption features in the infrared (IR) region. Figure 4.1 (c) shows the spectra of CO_2, H_2O, and CO within 1650-3100cm^{-1}. Although, neither CO_2 nor CO has any common features with the aldehydes in the mid IR, H_2O is a possible interfering species in the development of laser absorption schemes for detecting aldehydes. Therefore, it is important to accurately determine the spectral parameters such as absorption cross sections, line strengths, and broadening coefficients of aldehydes so that calibration free sensors could be developed.

In the literature, there are some studies on the microwave [74,75] and infrared [76-80] spectra of propanal. The fundamental vibrational band assignments were done for normal propanal (propanal -d0) as well as its three isotopomers (propanal -d1, d2, and d5). One of the

most recent studies was conducted by Guirgis et al. [76] in which they recorded the mid IR spectrum of propanal from 400 to 3500 cm^{-1} at resolution of 1 cm^{-1} and the far IR spectrum of propanal from 50 to 360 cm^{-1} at resolution of 0.1cm^{-1}. They reported the 24 fundamental vibrational bands and also indicated the discrepancies in the assignments of 6 of the fundamentals between the previous studies. They performed ab initio calculations and reassigned some of these bands with the help of the infrared and Raman data taken for gaseous, liquid, and solid propanal.

In this study a Fourier Transform Infrared Spectrometer (FTIR) is used to determine the absorption cross section of propanal as well as its band strengths in the wavenumber regions between 750 and 3300 cm^{-1}. In order to accurately determine the cross section of propanal, the measurements were carried out at room temperature (295K) and at seven different pressures (6, 8, 10, 12, 14, 22, and 33 Torr). The absorption cross section was recorded at resolutions of 0.08 and 0.096 cm^{-1} for the wavenumber regions from 750 to 1900 cm^{-1} and 1900 to 3300 cm^{-1}, respectively. The results were compared with the spectral data of PNNL database taken at a temperature of 296K and resolution of 0.112 cm^{-1}. The integrated band intensities were calculated to compare the current study results with the PNNL database. The current study results also give the 19 fundamental frequencies that fall within 750-3300 cm^{-1} and the assignments shown here are based on the previous works of Guirgis et al [76].

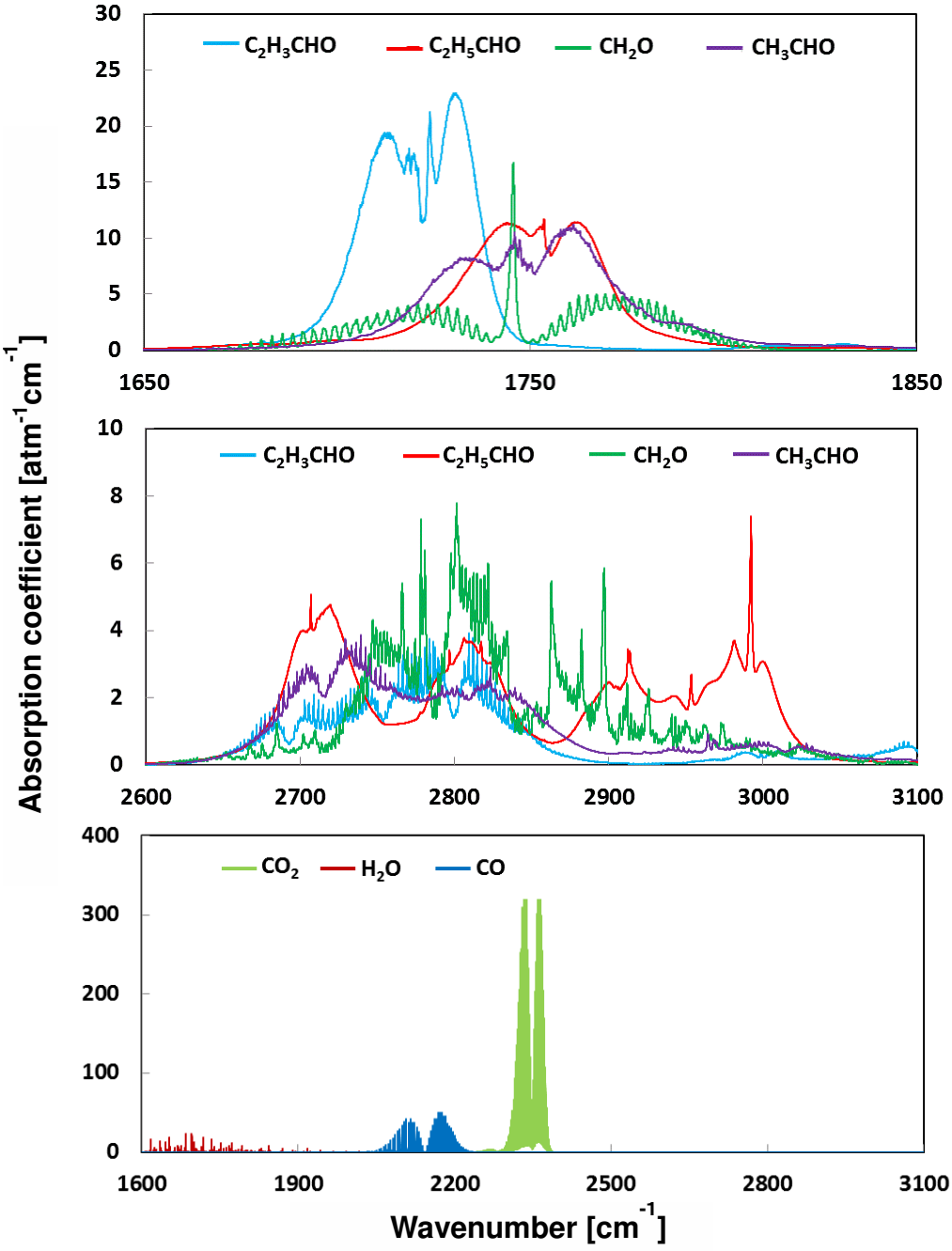

Figure 4.1 Absorption spectra of (a), (b) aldehydes: Acrolein (C_2H_3CHO), propanal (C_2H_5CHO), Formaldehyde (CH_2O), and Acetaldehyde (CH_3CHO); and (c) interfering species: Carbon dioxide (CO_2), water (H_2O), and Carbon monoxide (CO). Data is taken from PNNL and HITRAN databases.

Table 4-1- FTIR configuration for the measurements of propanal spectroscopic parameters

FTIR Spectrometer Configuration	
Resolution	0.08 and 0.096 cm^{-1}
Beamsplitter	Potassium bromide (KBr)
FTIR input aperture	3.5 mm
Detector	MCT HgCdTe
Lightsource	Globar (mid-infrared)
Optical path length (stainless-steel cell)	10 cm
Zero-filling	2× and 4× zero-filling
Pressure gauge	Baratron (1000 Torr FSR, ±0.05% accuracy)

4.2 Fourier Transform Infrared Spectrometer and Experimental Procedure

The absorption spectra of propanal was recorded over the wavenumber range of 750-3300 cm^{-1} using a vacuum bench Bomem DA8 Fourier Transform Infrared spectrometer described in [81]. Figure 4.2 shows the schematic of the FTIR setup. The spectrometer has a maximum resolution of 0.017 cm^{-1} and can be operated within the wavenumber range of 400-6500cm^{-1}. In this study the highest resolution used was 0.08cm^{-1} due to the relatively broad linewidth feature of the analyte [72]. The FTIR was configured as described in Table 4-1. A potassium bromide (KBr) beam splitter was used with the globar light source to make the measurements along a 10 cm path length stainless steel cell with NaCl windows. An MCT detector was used for the spectral measurements. Pressure in the sample cell was monitored using a Baratron capacitance gauge (1000 Torr full-scale range, 0.05% uncertainty). The manifold and the sample cell, located inside the FTIR compartment, were evacuated to less than $1x10^{-5}$ Torr with a turbo molecular pump system (Edwards T11213302) before the start of every experiment. The FTIR chamber was evacuated to pressures of less than 0.1Torr with a rotary vane pump in order to minimize the interference by atmospheric air. The average leak rate of the

cell was 3.0×10^{-3} Torr/min. The spectral measurements were done at seven different pressures (6, 8, 10, 12, 14, 22, and 33 Torr) and at room temperature (295K) to accurately determine the absorption cross section and the band strength. To account for the spectral drift in the data, reference scans were taken before and after the transmission data. This drift was taken into account in determining the uncertainty of propanal absorption cross section. No spectral subtraction was done, since the absorbance data did not show any trace of interfering species (H_2O or CO_2).

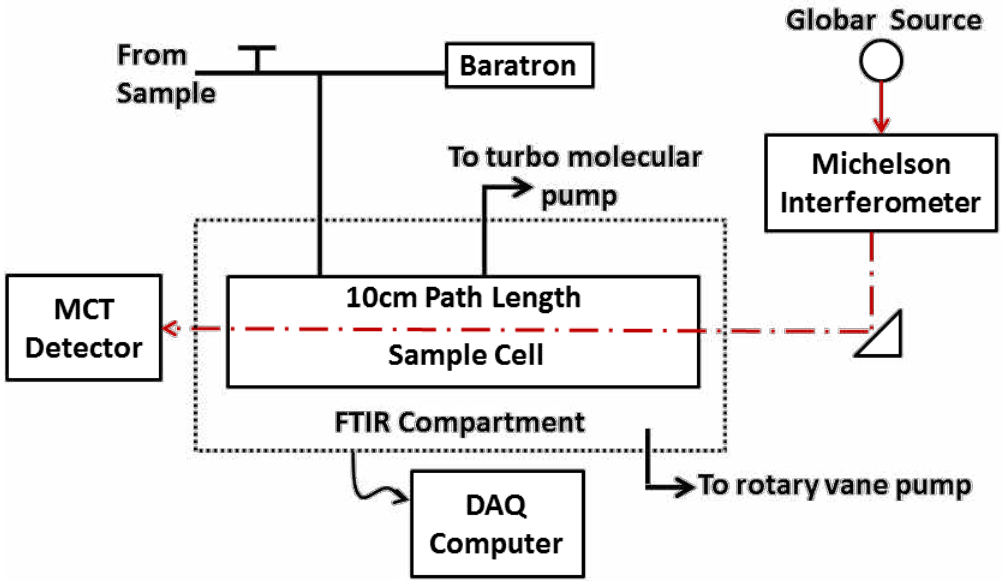

Figure 4.2 Experimental setup for the FTIR measurements of propanal

To achieve the desired resolution, the aperture size, wavenumber, and the signal to noise ratio (SNR) were controlled. An increase in the aperture size improves the SNR but also limits the highest resolution achievable. In addition, at higher wavenumbers (~3300cm^{-1}), it becomes difficult to obtain the desired resolution. Therefore, the aperture size was set to 3.5mm for all wavelength regions of interest and total of 300 scans were taken at each pressure to obtain a

good SNR. The data within the regions of 750-1900cm^{-1} and 1900-3300 cm^{-1} were taken at 0.08, and 0.096cm^{-1} resolution, respectively. These spectra were then zero filed by a factor of 2 for the 0.096 cm^{-1} resolution scans and by a factor of 4 for the 0.08 cm^{-1} resolution scans. The high resolution spectra were taken at these spectral regions because all the aldehydes have strongly absorbing features due to their common C=O and C-H stretching. High purity propanal (>99.6%), supplied by Fisher Scientific, was used in this study. Samples were prepared by transferring the propanal into a test tube that was connected to the gas manifold via a Swagelok Ultra-Torr vacuum fitting.

4.3 Data Analysis

4.3.1 Absorption Cross-section of Propanal

The rotational and vibrational transitions of the gas molecules through absorption of the incident light at frequency, ν follow the Beer Lambert law given by

$$-\log\left(\frac{I}{I_o}\right)_\nu = S\phi_\nu PL = \beta_\nu PL = \alpha_\nu \qquad (4\text{-}1)$$

where I and I_o are the spectral intensity of the light passing through the analyte propanal and the empty cell, respectively; S [cm^{-2} atm^{-1}] is the line strength; ϕ_ν [cm] is the frequency-dependent lineshape function; β_ν [cm^{-1}atm^{-1}] is the frequency-dependent absorption coefficient; P [atm] is the pressure of the gas inside the cell; L[cm] is the optical path length; and α_ν is the absorbance.

The integrated absorbance removes the normalized contribution of the lineshape and thus reduces Eq. (4-1) to

$$A = \int \alpha_\nu d\nu = S_{band} PL \tag{4-2}$$

The integrated absorbance given by Eq. (4-2) was plotted in Figure 4.4 for different bands of propanal to show the linearity of the integrated absorbance with the product, *PL,* and thus to obtain the S_{band} through the slope of the linear fit.

4.3.2 Comparison of Current Study Results with PNNL Database

To compare the current study results with those from PNNL, the dependence of absorption coefficient on temperature and pressure must be eliminated. Therefore, the absorption cross-section σ_ν [cm^2/molecule] is used for comparison purposes, which can be obtained through the knowledge of β_ν as follows

$$\sigma_\nu = \left(\frac{T}{273.15}\right)\left(\frac{\beta_\nu}{N}\right) \tag{4-3}$$

where T [K] is the temperature of the gas and N= 2.6867 x 10^{19} [molecule/cm^{3}atm] is the Loschmidt number at standard temperature (273.15K) and pressure (1 atm).

The PNNL data was recorded at a total pressure of 1 atm with ten different propanal mole fractions in pure N_2 at 296 K [72]. The optical path length of the cell was 100 cm. These values were used in Eqs. (4-1) and (4-3) to obtain the σ_ν values of propanal from PNNL. In this study, the absorption spectrum was recorded at seven different pressures to accurately determine the absorption cross sections [σ_ν]. A data reduction scheme described by Sharpe et al. [72] was

used to report the PNNL database and subsequently was implemented in the current work to compare the results with those of PNNL. In this scheme, the recorded absorbance, *A*, from each different pressure measurements was plotted against the burden [*PL*], defined as the pressure [*P*] multiplied by the optical path length [*L*]. A weighted least squares fit with zero intercept was then performed in which the data points with an absorbance of $\alpha_\nu \geq 1.6$ were assigned a weight of zero. The slope of the fit was the absorption coefficient [β_ν] given in Eq. (4-1). The weighting scheme favors higher burden measurements for weakly absorbing features and lower burden measurements for strongly absorbing features. The main reason for applying this scheme was to remove the transmission data points which show saturation at certain wavenumbers due to the strong absorption of propanal. The overall effect of this fit is to reduce the inherent nonlinearities of the FTIR measurements and also to improve the SNR.

4.4 Results and Discussion

4.4.1 Absorption Cross-sections and Vibrational assignments

Figure 4.3 shows the current study results of the absorption cross-section of propanal (CH_3-CH_2-CHO) as well as the vibrational assignments for different spectral regions of interest at room temperature (295 K). Figure 4.3 also includes the data of PNNL taken at 296 K for comparison purposes. The spectra shown in Figure 4.3 (a), (b), and (c) were recorded at 0.08 cm^{-1} resolution, whereas Figure 4.3 (d) data was recorded at 0.096 cm^{-1} resolution. Figure 4.3 demonstrates that the discrepancy between the current study results and PNNL database is very small. The exact difference is given in the next section; however, it is clear from the figure that

the sharp rovibrational Q transitions have higher absorption cross sections in the current study than those given by PNNL database. The difference becomes more pronounced especially for v_7, v_{13}, and v_{16} transitions. This result is attributed to the fact that the spectral lines are better resolved in the present study. Propanal shows strong absorption bands in the mid IR region. Various vibrational modes of propanal given in Figure 4.3 were based on the assignments of previous study by Guirgis et al. [76] which recorded the spectrum at 1 cm^{-1} resolution using Fourier Transform Spectrometer from 400 to 3500 cm^{-1} and at 0.1 cm^{-1} resolution from 50 to 380 cm^{-1}. Propanal has 24 vibrational modes.

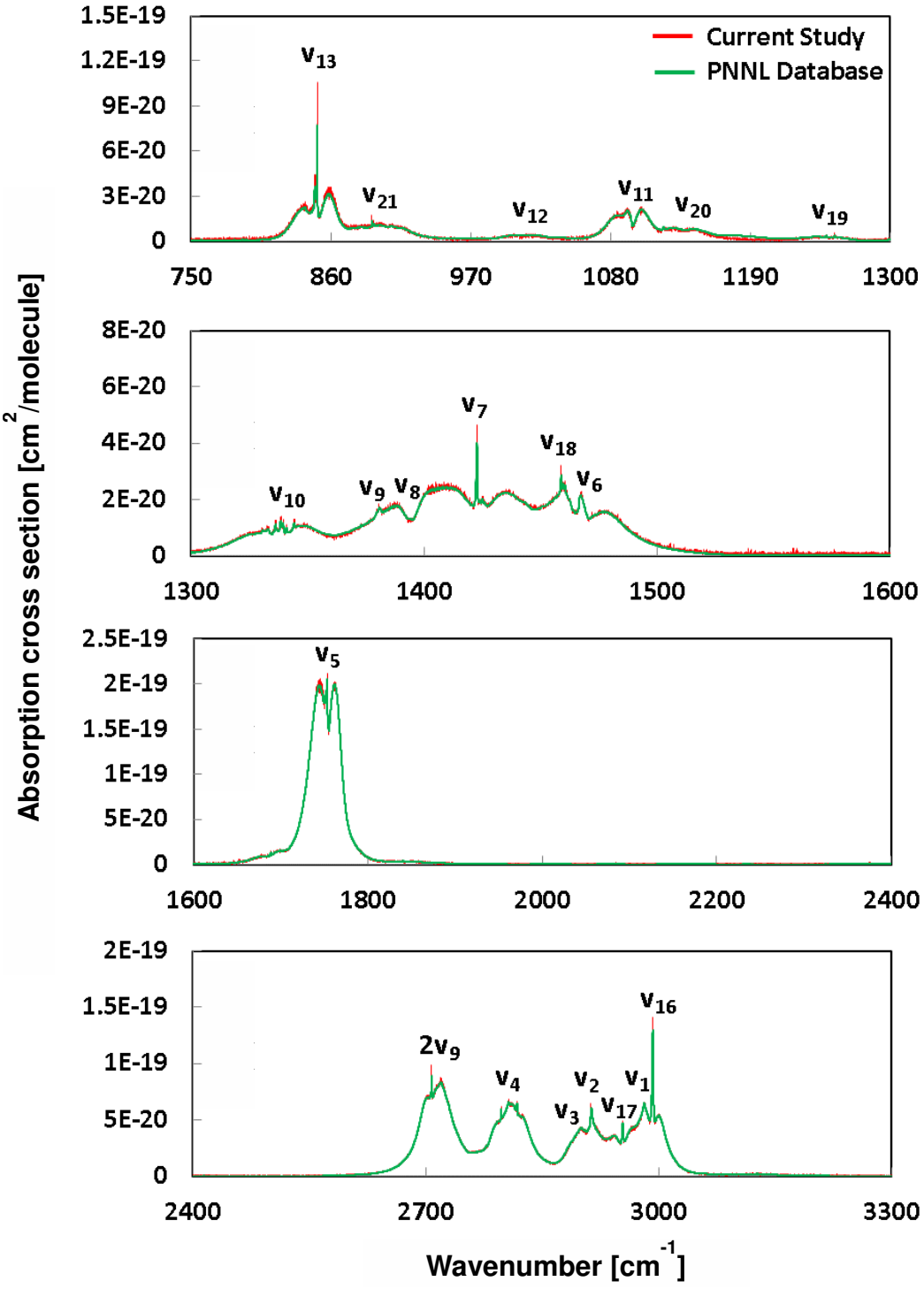

Figure 4.3 IR absorption spectra of propanal at 295K in the regions of (a) 750-1300 cm^{-1}, (b) 1300- 1600 cm^{-1}, (c) 1600-2400 cm^{-1}, and (d) 2400 -3300 cm^{-1}

Table 4-2- Vibrational Assignments for the IR bands of propanal

Band	Fundamental wavenumber [cm^{-1}] (Guirgis et al.)	Fundamental wavenumber [cm^{-1}] (current study)	Vibrational Assignment
$\nu_1(a')$	2981	2980.83	CH_3 antisymmetric stretch
$\nu_2(a')$	2914	2913.88	CH_2 symmetric stretch
$\nu_3(a')$	2905	2905.80	CH_3 symmetric stretch
$\nu_4(a')$	2818	2817.60	CH stretch
$\nu_5(a')$	1754	1753.57	C=O stretch
$\nu_6(a')$	1467	1467.42	CH_3 antisymmetric deformation
$\nu_7(a')$	1423	1422.71	CH_2 deformation
$\nu_8(a')$	1395	1394.75	CH_3 symmetric deformation
$\nu_9(a')$	1381	1380.49	CH bend
$\nu_{10}(a')$	1339	1338.49	CH_2 wag
$\nu_{11}(a')$	1098	1098.33	CH_3 rock
$\nu_{12}(a')$	1009	1009.71	CCC antisymmetric stretch
$\nu_{13}(a')$	849	849.14	CCC symmetric stretch
$\nu_{14}(a')$	661	---	OCC bend
$\nu_{15}(a')$	264.1	---	CCC bend
$\nu_{16}(a'')$	2992	2992.28	CH_3 antisymmetric stretch
$\nu_{17}(a'')$	2954	2953.53	CH_2 antisymmetric stretch
$\nu_{18}(a'')$	1459	1458.87	CH_3 antisymmetric deformation
$\nu_{19}(a'')$	1250	1249.96	CH_2 twist
$\nu_{20}(a'')$	1127	1127.29	C-H bend
$\nu_{21}(a'')$	892	891.95	CH_3 rock
$\nu_{22}(a'')$	658	---	CH_2 rock
$\nu_{23}(a'')$	219.9	---	Methyl torsion
$\nu_{24}(a'')$	135.1	---	C(O)H torsion

Table 4-3- The band strengths of propanal at various infrared regions and comparison of integrated absorption cross sections between PNNL database and current study

Wavenumber [cm^{-1}]	Current study		PNNL	% difference
	S_{band} [cm^{-2} atm^{-1}]	$\int \sigma_\nu d\nu$ [cm/molecule]	$\int \sigma_\nu d\nu$ [cm/molecule]	
750-1300	82.45	3.30 x10^{-18}	3.35 x10^{-18}	-1.27
1300-1600	70.46	2.72 x10^{-18}	2.77 x 10^{-18}	-1.96
1600-1900	240.13	9.87 x10^{-18}	9.70 x 10^{-18}	1.75
2400-3300	368.03	1.49 x10^{-17}	1.49 x 10^{-17}	0.25

Table 4-2 shows the positions of these fundamental bands and the vibrational assignments based on the results of the current study and those of Guirgis et al. [76]. There are mainly two vibrational modes of propanal which are common to all the aldehydes. These are the very strong C=O stretch and the strong C-H stretch. The very strong C=O stretch of propanal is assigned as the v_5 band. It has the three main peaks (P, Q, and R rotational lines) and is centered at 1753.57 cm^{-1}. The strong CH stretch of propanal is centered at 2817.60 cm^{-1} and is assigned as the v_4 band. In the 750-1290 cm^{-1} spectral region, propanal has also a very strong CCC symmetric stretch assigned as the v_{13} band. In this region, there are other weaker vibrational modes, v_{21}, v_{12}, v_{11}, v_{20}, and v_{19}. In the 1290-1530 cm^{-1} spectral region, the relatively strong v_7 band centered at 1422.71 cm^{-1} involves CH_2 deformation. In the 2650-3050 cm^{-1} spectral range, there is a very strong CH_3 antisymmetric stretch at 2992.28 cm^{-1}. Note that the current study results do not include five of the fundamentals (v_{14}, v_{15}, v_{22}, v_{23}, and v_{24}) that fall in the far IR region, because the MCT detector is unusable below 500 cm^{-1}. Even between 500 and 750 cm^{-1} the SNR for the given spectrometer resources was relatively low. A lower resolution of ~0.25 cm^{-1} was needed to obtain adequate SNR below 500 cm^{-1}. However, this range of data is not included here.

4.4.2 Integrated Absorbance and Band Strengths of Propanal

The absorption spectrum was divided into four different regions, (750-1300 cm^{-1}), (1300 -1600 cm^{-1}), (1600-2400 cm^{-1}), and (2400-3300 cm^{-1}). The integrated absorbance, *A,* given by Eq. (4-2) was calculated for each spectral region. The integrated absorbance values for each region were then plotted against the pressure multiplied by the optical path length [*P.L*]. A linear regression line with zero intercept was fit to each region. The results are presented in Figure 4.4. The fits for each of the regions had a correlation coefficient of R^2~0.99. The linear behavior of the integrated absorbance for each spectral region indicates that the intensities did not approach saturation and thus the Beer-Lambert law was applicable. The slope of the fitted line is the band strength, S_{band}, and is reported for each of the spectral regions in Table 4-3.

The absorption cross section data of propanal obtained in this study has a higher wavenumber resolution than the PNNL database. The PNNL data was recorded at 0.112 cm^{-1}, whereas the current study results were recorded at 0.08cm^{-1} within 750-1900cm^{-1} and at 0.096cm^{-1} within 1900-3300 cm^{-1}. Therefore, a comparison approach as described in Es-sebbar et al. [82] was used in which the integrated IR cross sections ($\int \sigma_\nu d\nu$) of propanal, rather than the absorption cross section at each wavenumber, were calculated and compared between the current study results and PNNL database. The comparison results are also outlined in Table 4-3. There was a very good agreement between the current experimental data results and PNNL database, the maximum deviation being 1.96% for the 1300-1600cm^{-1} region. The difference between the two measurements decreased as the wavenumber is increased and was only 0.25% in the 2400-3300 cm^{-1} region.

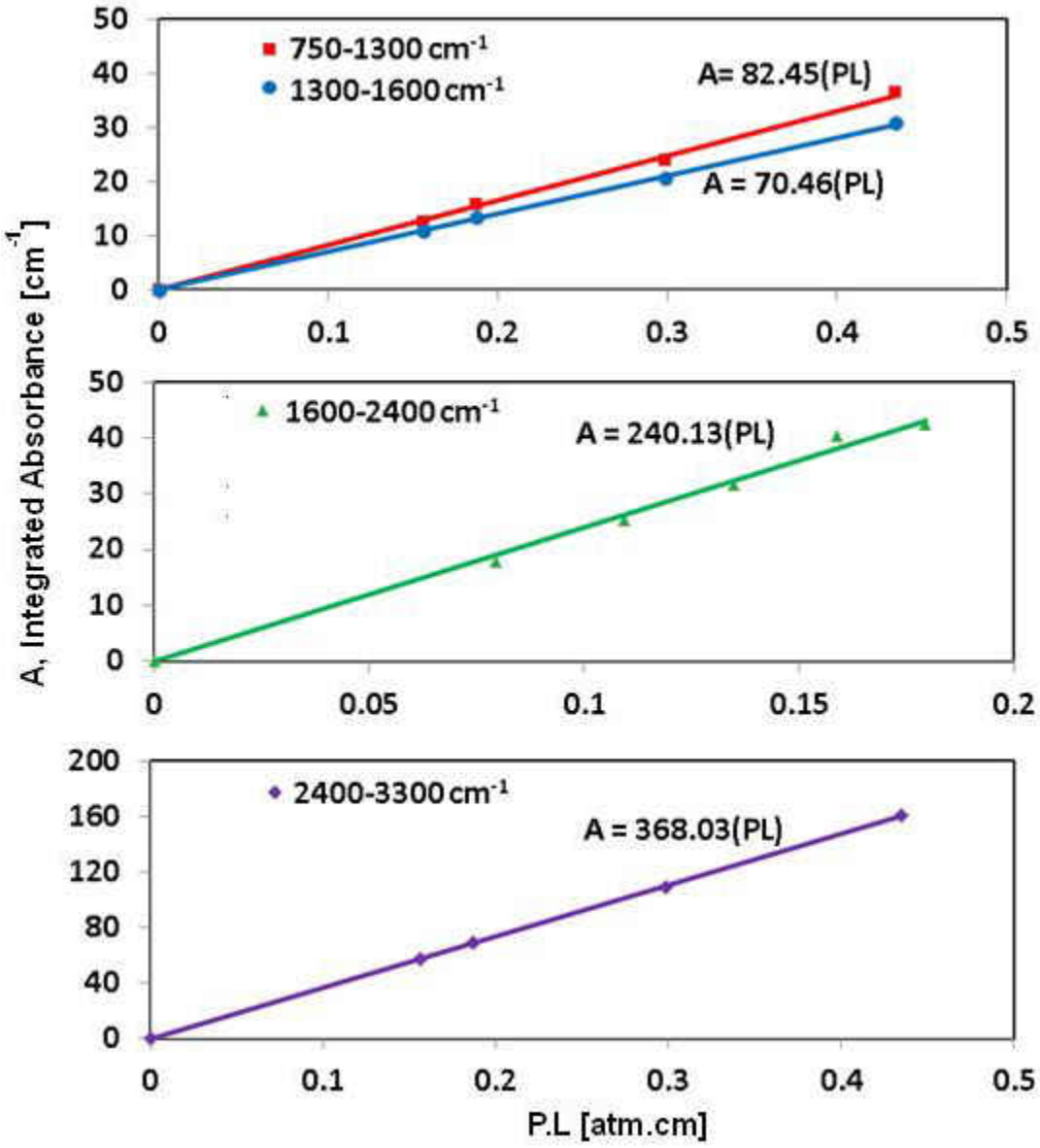

Figure 4.4 Linear dependence of propanal integrated absorbance on *PL* for various IR bands (a) 750-1300 cm^{-1} and 1300- 1600 cm^{-1}, (b) 1600-1900 cm^{-1}, and (c) 2400-3300 cm^{-1}

4.4.3 Uncertainty

Based on Eqs. (4-1) to (4-3) there is uncertainty in the calculation of absorption cross section [σ_ν], band strength [S_{band}], and integrated intensity [$\int \sigma_\nu d\nu$] due to the errors in the

measurements of pressure [P], temperature [T], and absorbance [α_ν]. The uncertainty of the pressure measurement resulted from the Baratron pressure gauge, which has an accuracy of 0.05%, as well as from the variation in the pressure of the sample cell due to the adsorption of molecules on the cell walls. The room temperature measurement had an uncertainty of $\pm 0.5^{\circ}\mathrm{C}$. The background (vacuum) measurements were taken before and after the sample measurements to account for the drift of the signal.

Table 4-4 shows the results of the uncertainty analysis for different wavenumber regions of the spectra. The background measurement drift was the main source of error that contributed to the uncertainty of the absorbance. The maximum uncertainty in the cross section was estimated to be ±9.15%, which occurred for lower wavenumber regions (750-1300 cm^{-1}) where the absorption of the propanal was very small. The maximum uncertainty in the other wavenumber regions was smaller. Note that the uncertainty varies by wavenumber; therefore, the resulting maximum uncertainty in the band strength and integrated intensity are weighted averages of the uncertainties in the cross section calculation.

4.5 Conclusions

The current study used a high-resolution Fourier Transform Infrared Spectrometer to measure the IR absorption cross-sections of propanal at room temperature (295K) and at spectral resolutions of 0.08 and 0.096 cm^{-1} within the spectral regions of 750-1900cm^{-1} and 1900-3300cm^{-1}, respectively. The absorption spectra as well as the fundamental line positions were presented. The band strengths were reported for various spectral regions and the integrated band intensities were compared with the PNNL database, which were recorded at a lower resolution of

0.112 cm^{-1}. There was a very good agreement between the current experimental data results and PNNL database, the maximum deviation being 1.9645% for the 1300-1600cm^{-1} region. The difference between the two measurements decreased as the wavenumber was increased and was only 0.25% in the 2400-3300 cm^{-1} region. This part of the doctorate study aided in the development of quantitative absorption detection schemes for the concentration measurements of propanal, which is a major biofuel combustion intermediate that is also found in the exhaust emissions. The results can also be incorporated in atmospheric models. The details of the propanal detection scheme during its pyrolysis are given in chapter 5.

Table 4-4- Uncertainty analysis results for the absorption cross section, band strength, and integrated intensity of propanal

		Wavenumber Range [cm^{-1}]			
		750-1300	1300-1600	1600-2400	2400-3300
Measured Variables	P [atm]	$\pm 0.05\,\%$			
	T [K]	$\pm 0.5^{\circ}C$			
	α_ν	$\pm 9.15\,\%$	$\pm 4.71\,\%$	$\pm 0.03\,\%$	$\pm 0.87\,\%$
Calculated Variables	σ_ν [cm^2/molecule]	$\pm 9.15\,\%$	$\pm 4.72\,\%$	$\pm 0.18\,\%$	$\pm 0.93\,\%$
	S_{band} [cm^{-2} atm^{-1}]	$\pm 4.21\,\%$	$\pm 3.41\,\%$	$\pm 0.74\,\%$	$\pm 2.85\,\%$
	$\int \sigma_\nu d\nu$ [cm/molecule]	$\pm 6.11\,\%$	$\pm 3.58\,\%$	$\pm 4.23\,\%$	$\pm 2.95\,\%$

CHAPTER 5: MEASUREMENTS OF PROPANAL IGNITION DELAY TIMES AND SPECIES TIME-HISTORIES

5.1 Introduction

Biofuels, which are oxygenated hydrocarbons, are increasingly being used in combustion systems for power generation and transportation [1]. Biofuels are present as either additives to fossil products or as standalone fuels. Inherent in these oxygenated species are various functional groups such as, alcohols, alkyl esters, furans, etc. and aldehydes are relatively stable intermediates produced during their combustion. Aldehydes can survive until the end of combustion and appear as pollutants at the exhaust. Formaldehyde (CH_2O), acetaldehyde (CH_3CHO), acrolein (C_2H_3CHO), and propanal (CH_3CH_2CHO) are reported to be the most abundant aldehydes - listed as hazardous air pollutants (HAP) by the United States Environmental Protection Agency (USEPA, 2012a) - in the exhaust emissions of biofuels [19]. Thus it is important to understand the combustion kinetics of these aldehydes for wide deployment of biofuels and development of cleaner engines. While lower aldehydes have been the focus of many literature studies, propanal received scant attention until recently. Studies in the literature for propanal include ignition delay times, pyrolysis, and flame speeds [6,44,83-91].

Pelucchi et al. [44] conducted the most recent shock tube ignition delay times measurements of propanal at 1-3 atm. Also, they developed two detailed chemical sub-mechanisms (referred here as POLIMI [44] and NUIG [44] Mechanisms) in two different kinetic schemes for normal C_3-C_5 aldehydes. Their modeling and experimental results for ignition delay times had larger deviations at atmospheric conditions compared to those at 3atm. A similar discrepancy at 1 atm was reported by Akih-Kumgeh and Bergthorson [6] in an earlier study of

modeling and shock tube data. It was shown that the measured ignition delay times of propanal were well predicted by their kinetic mechanism (referred here as McGill [6] Mechanism) at high pressures around 12 atm.

Table 5-1- Summary of propanal studies in the literature

Propanal Study	Setup	T [K]	P [atm]	Reference
Propanal Pyrolysis	Shock tube	972–1372	1.4 - 2.8	Pelucchi et al. (2015) [44]
		970–1300	2.0 - 2.7	Lifshitz et al. (1990) [84]
Propanal+O_2+Ar	Shock tube	1170–1750	1.0, 3.0	Pelucchi et al. (2015) [44]
		1150–1560	1.0, 12.0	Akih–Kumgeh (2011) [6]
	Jet stirred reactor	500–1100	10.0	Veloo et al. (2013) [85]
	Mass Spectrometer	553–713	0.06-0.16	Kaiser (1983) [86]
Propanal+OH	Shock tube	958-1288	1.0, 2.0	Wang et al. (2014) [83]
	PLP-LIF	243-372	1.0	Thévenet et al. (2000) [87]
	Flash Photolysis	295	1.0	Le Crâne et al. (2005) [88]
Propanal flame speed	Premixed flame	343	1.0	Veloo et al. (2013) [85]
		314–2000	0.05	Kasper et al. (2009) [89]
	Cylindrical bomb	343, 393	1.0	Gong et al. (2014) [90]
	Spherical bomb	298	1.0	Burluka et al. (2010) [91]

The current literature on the propanal ignition and pyrolysis is summarized in Table 5-1. There exists two experimental/modeling studies on the pyrolysis of propanal [44,84]. These

shock tube speciation studies indicated that the thermal decomposition of propanal and chain radical initiation happened via unimolecular decomposition through C-C bond cleavage. Also, propanal decomposition mainly occurred through H-atom abstraction reactions by H atoms and CH_3 radicals, the latter reaction leading to methane formation. Lifshitz et al. [84] reported that the gas chromatography analysis of propanal decomposition products around 1200K measured behind the reflected shock waves included CO, C_2H_4, and CH_4 (in order of decreasing abundance). It is clear that methane is an important product of propanal pyrolysis, however, both experimental studies [44,84] pointed out that the predictions underestimated the measured methane concentration values by more than 50 %.

While ignition delay times are an important design parameter, species time-history measurements can provide validation and refinement of detailed kinetic models, which in turn leads to more accurate ignition time and intermediate species mole fractions predictions. Therefore, in this doctoral study the concentration time-histories of methane and propanal during propanal pyrolysis were measured by means of interference-free line of sight laser absorption diagnostics behind reflected shock waves at 1 atm and temperatures between 1192 K < T < 1388 K. In addition, ignition delay times of propanal were measured at 1 and 6 atm and between 1129 K< T < 1696 K. Current experimental results were compared to literature data as well as predictions of three kinetic mechanisms (POLIMI, NUIG, and McGill Mechanisms). In addition, reaction rates improvements for accurate predictions were suggested based on a sensitivity analysis.

5.2 Experimental Setup and Procedure

Details of UCF shock tube facility including fuel/oxidizer mixture preparation, ignition delay time measurements, and species mole fraction diagnostics are provided in chapter 3.

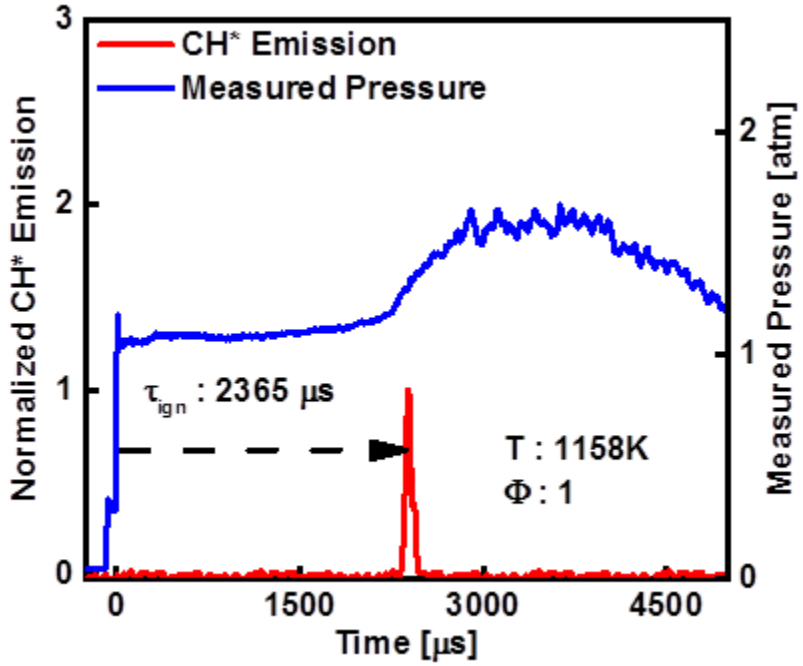

Figure 5.1 Pressure and normalized CH* emission traces during stoichiometric ignition of 1% propanal in O_2/Ar (P_5 ~ 1.0 atm, T_5=1158 K).

5.2.1 Ignition Delay Time Measurements

Temperature (T_5) and pressure (P_5) in the reflected shock region were calculated based on the extrapolated end wall incident shock velocity with uncertainties estimated to be less than ±1.5%. The uncertainty in the ignition delay time was estimated to be less than ±20%. Figure 5.1 shows a sample ignition data during stoichiometric ignition of 1% propanal in O_2/Ar (P_5 ~ 1.0 atm, T_5=1158 K). The CH* emission output from the detector was normalized to its peak (maximum) voltage.

5.2.2 CH4 Mole Fraction Measurements

A cascade laser (Nanoplus DFB ICL) was used for determining methane concentration time-histories during propanal pyrolysis. A peak-minus-valley laser absorption scheme was implemented near the P (8) line of methane's v_3 band (λ_{peak} = 3403.4 nm and λ_{valley} = 3403.7 nm). The same wavelength pair was first suggested by Pyun et al. for interference-free detection of methane during n-heptane pyrolysis [53,92]. The ratio of the transmitted and reference light intensities (I_{tr}/I_{ref}) was measured in order to obtain CH_4 mole fraction from Beer-Lambert law:

$$\alpha = -\ln(\frac{I_{tr}}{I_{ref}})_{\nu} = \sigma(\nu, T, P)\frac{P_{tot}}{RT}\chi L \tag{5-1}$$

where α_{ν} is absorbance, σ [cm^2/molecule] is absorption cross section, P [atm] is pressure, and T [K] is temperature, L [cm] is path length, and χ is the mole fraction of the absorbing species. By subtracting absorbance measurements at the valley wavelength from those at the peak value, interference was eliminated and only the absorbing species (i.e., CH_4) remained:

$$\chi_{CH_4} = \frac{(\alpha_{CH_4,peak} - \alpha_{CH_4,valley})}{\frac{(\sigma_{CH_4,peak} - \sigma_{CH_4,valley})P_{tot}L}{RT}} \tag{5-2}$$

Methane absorption cross sections at high temperatures (1200K < T < 2000 K) near 1 atm were measured in order to obtain an empirical correlation for the absorption cross section. These measurements had uncertainties of less than ±6% and are discussed in Chapter 7. The empirical correlation that relates the absorption cross-section of methane to temperature and pressure are used here to obtain methane mole fraction during propanal pyrolysis. Propanal absorption cross section measurements at room temperature [47] indicated that propanal has a differential

absorption cross section of 0.06 m^2/mol at the chosen peak and valley wavelength pair. In addition, methane time-histories data (Figure 5.2) revealed that the differential methane absorbance after the arrival of the reflected shock wave was zero, indicating negligible interference from propanal.

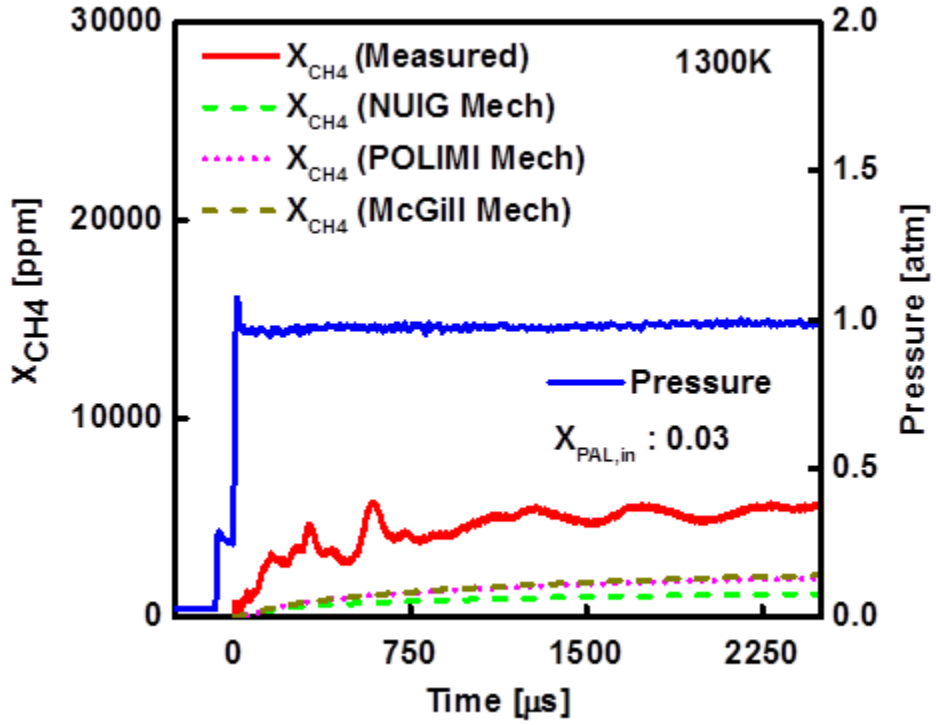

Figure 5.2 Measured methane mole fraction (XCH4) and pressure time-histories behind reflected shock waves at 1300 K and 1 atm during 3% propanal pyrolysis in argon. Predictions by NUIG [7], POLIMI [7] and McGill [17] Mechs are also shown.

5.2.3 Propanal Mole Fraction Measurements

In this study, propanal mole fraction measurements were carried out at the valley wavelength, λ_{valley} = 3403.7 nm during the initial stages of its pyrolysis. In order to identify the interfering species at this wavelength, the NUIG Mechanism was used to determine mole fractions of the top 15 species formed during 3% propanal pyrolysis (in argon) at 1300 K and 1

atm. Absorbance values for each species were calculated in order to quantify their interference using the predicted mole fraction profiles. Figure 5.3 shows the results of major absorbance contributions during the first 150 μs after the start of propanal pyrolysis. Only the species having absorbance values higher than 10^{-5} are plotted in Figure 5.3 for clarity. The absorption cross sections of major interfering species such as CH_4, C_2H_4, C_2H_6, and CH_2O, etc. at high temperatures and 1atm are available in the literature [52,73,93-96]. The room temperature spectra at 1atm were taken from PNNL database for other interfering species (e.g.C_4H_6, C_3H_8) [97]. Note that the absorption cross sections of these hydrocarbons were reported to decrease as temperature was increased [52,73,93-96]. Hence using the room temperature absorption cross sections at 1 atm (in Figure 5.3) was a significantly conservative assumption to quantify the interference at the chosen wavelength. It was seen that most species had very low or no absorbance features at the chosen valley wavelength- all these interfering species accounted for 1.72% of the total absorbance. Methane absorbance became prominent at later times (after 150μs). Therefore, propanal time-histories were determined with negligible interference based on the valley wavelength measurements during the first 150 μs of its pyrolysis as shown in Figure 5.4.

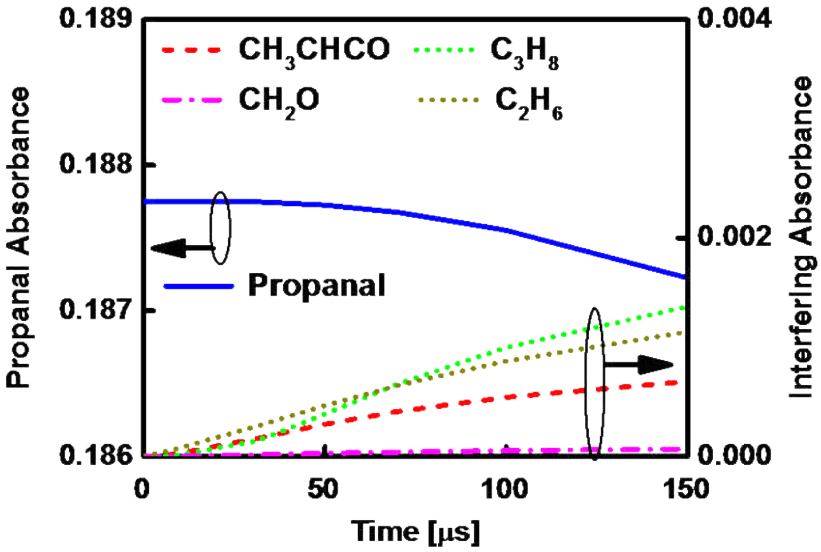

Figure 5.3 The absorbance time-histories of major interfering species determined based on the NUIG Mech [7] predictions (see text) at 1300 K and 1 atm during 3% propanal pyrolysis in argon.

5.3 Results and Discussion

5.3.1 Methane and Propanal Time-Histories

Figure 5.4 shows the measured propanal mole fraction time-histories for 3% propanal pyrolysis in Ar at 1388 K (1 atm) along with predictions by NUIG [44], POLIMI [44], and McGill [6] mechanisms. Simulations were carried out using the homogeneous batch reactor model of CHEMKIN PRO [18] with constant internal energy and constant volume assumptions. It was seen that the measured propanal concentrations decreased gradually as pyrolysis progressed. Comparison with predictions revealed that both NUIG [44] and POLIMI [44] mechanisms provided the propanal decomposition rate better than the McGill mechanism [6]. Note that the error bars included at two locations clearly displayed the excellent agreement between current measurements and the POLIMI [44] mechanism predictions.

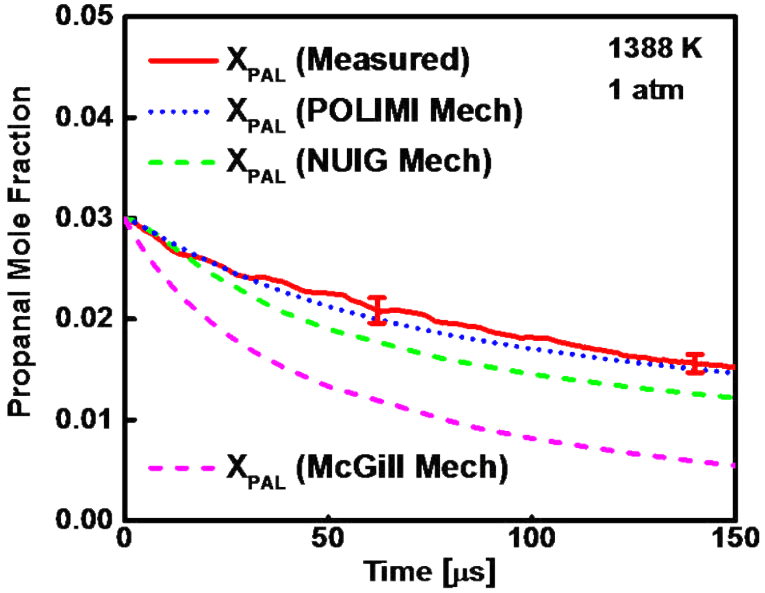

Figure 5.4 The measured propanal mole fraction (X_{PAL}) time- histories at 1388 K and 1 atm during 3% propanal pyrolysis in argon. Predictions by NUIG [7], POLIMI [7] and McGill [17] Mechs are also shown.

Measured mole fraction time-histories of methane shown in Figure 5.2 started rising after the arrival of the reflected show wave and slowly reached a plateau value within the first 1000 μs at 1300K (3% propanal+Ar, 1atm). The concentration predictions obtained from three recent aldehyde mechanisms (NUIG [44], POLIMI [44], and McGill [6] Mechs) are also plotted in Figure 5.2. Predictions by the McGill and POLIMI mechanisms were closer to the experimental data than those by the NUIG mechanism. However, all three mechanisms under predicted current data and there was a considerable discrepancy (Figure 5.2) with experimental profile. Note that there is no pressure rise in the reflected shock region. Because of its reasonable performance against propanal molefraction data, the POLIMI [44] mechanism was chosen for detailed

examination of propanal pyrolysis kinetics in order to understand the deviation seen in methane mole fraction comparisons.

5.3.2 Sensitivity Analysis

A sensitivity analysis was carried out using the POLIMI [44] mechanism (using the CHEMKIN PRO [18] sensitivity tool) for both propanal (Figure 5.5 a) and methane (Figure 5.5 b) during pyrolysis of 3% propanal in argon at 1388 K and 1 atm. Note that most of the dominant reactions were the same for both species. The reaction pathway shown by PAL (+M) = products included two unimolecular decomposition reactions given by R_1 and R_2 in Table 5-2. Pelucchi et al. [44] obtained the rates of R_1 and R_2 from RRKM/ME and QRRK/MSC calculations. The other important group of reactions involved the H abstraction product channels of reaction between methyl radical and propanal leading to methane formation. These are denoted by R_3, R_4, and R_5 in Table 5-2 and shown as CH_3+PAL = CH_4+products in Figure 5.5 (a) and (b). Note that the POLIMI mechanism uses a semi-lumped approach for part of their kinetic scheme. In addition, there were two other H abstraction reactions in the system denoted by R_6 and R_7 in Table 5-2 and demonstrated as H+PAL = H_2+products in Figure 5.5 (a) and (b). The rates of the H abstraction reactions of the acyl H-atom at the alfa position of propanal (R_5 and R_7) were estimated by Pelucchi et al. [44] based on an analogy with the same site in formaldehyde and acetaldehyde. The rate constants for abstractions from the remaining secondary (R_4 and R_6) and primary (R_3) H-atoms were adopted by Pelucchi et al. [44] according to the values used for n-alkanes by Ranzi et al. [98].

Since none of the reactions listed in Table 5-2 were experimentally determined before, mechanistic adjustments to their rates were implemented so that the experimentally obtained methane and propanal mole fraction profiles can be better predicted by the POLIMI [44] mechanism. These changes are given in Table 5-2 as a multiplication factor from the original values used in POLIMI [44] Mechanism. The discrepancy with the current experimental methane concentration results indicated that the branching ratio had to be modified in favor of the methyl radical forming channel, R_2. Hence the rate of R_2 was increased and that of R_1 was decreased. This was to keep the total propanal decomposition rate unchanged (due to the excellent agreement with POLIMI [44] Mechanism predictions and current propanal mole fraction data). Although, this procedure decreased the discrepancy in predictions for methane mole fractions, it deteriorated the agreement between modeled and measured propanal mole fraction profiles. Therefore, similar mechanistic reaction rate changes were adopted on the H abstraction reactions to favor methane formation through R_3, R_4, and R_5. Again, increasing these reaction rates accelerated the consumption of propanal, hence the rates of the remaining dominant reactions in the system (R_6 and R_7) were decreased.

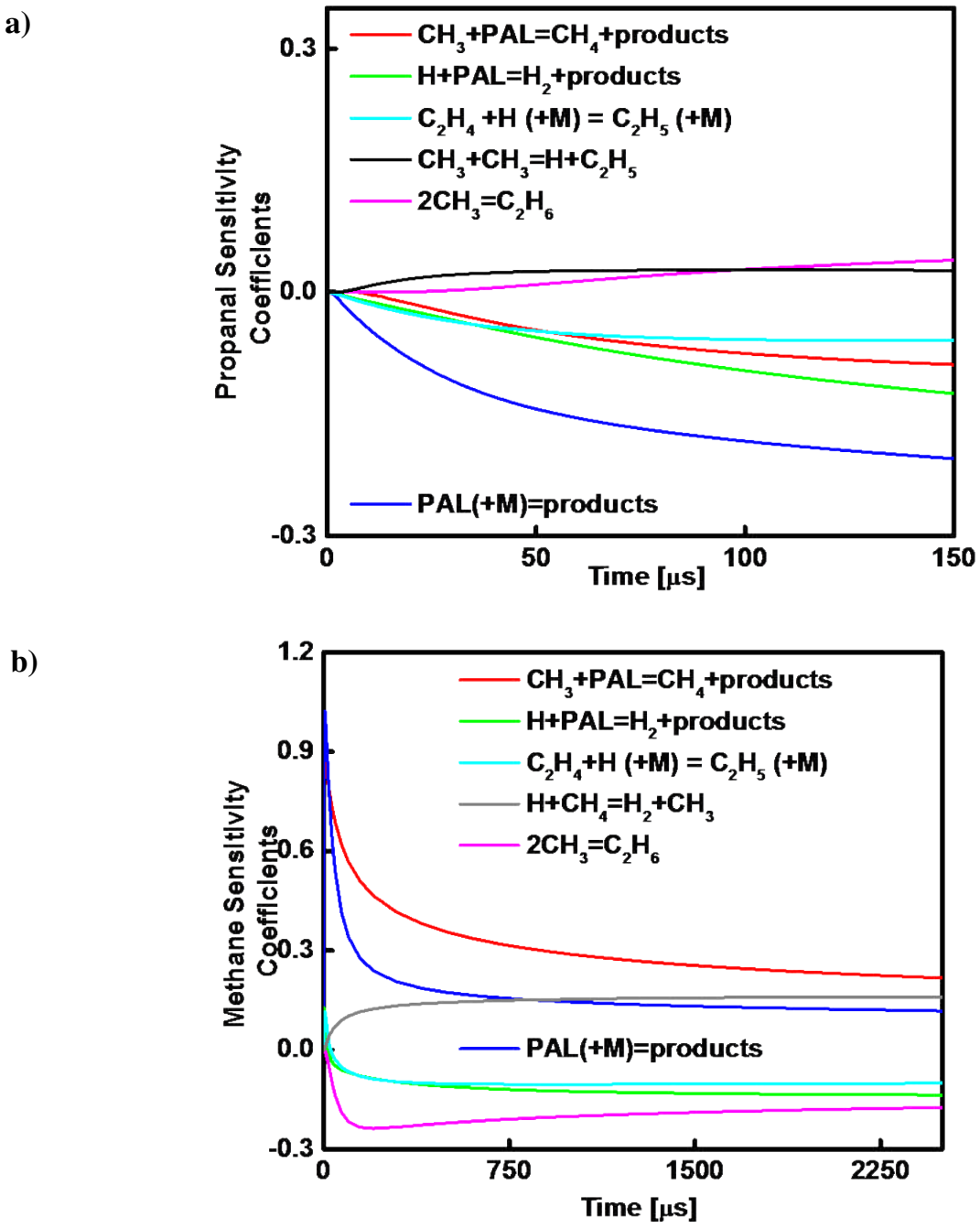

Figure 5.5 The sensitivity analysis results for **(a)** propanal and **(b)** methane during 3% propanal pyrolysis in argon bath gas at 1388 K and 1 atm using the POLIMI [7] mechanism.

Table 5-2- The modified reaction rates in the adjusted POLIMI mechanism

Reaction ($k = A T^b \exp(E_a/R_u T)$)	**Multiplication Factor**	**No.**
$C_2H_5CHO \Leftrightarrow HCO + C_2H_5$	1/2	(R 1)
$C_2H_5CHO \Leftrightarrow CH_3 + CH_2CHO$	2	(R 2)
$CH_3 + C_2H_5CHO \Leftrightarrow CH_4 + C_2H_4 + HCO$	10	(R 3)
$CH_3 + C_2H_5CHO \Leftrightarrow CH_4 + C_2H_3CHO + H$	10	(R 4)
$CH_3 + C_2H_5CHO \Leftrightarrow CH_4 + .9C_2H_5 + .9CO + .1CH_2CO + .1CH_3$	10	(R 5)
$H + C_2H_5CHO \Leftrightarrow H_2 + C_2H_3CHO + H$	1/10	(R 6)
$H + C_2H_5CHO \Leftrightarrow H_2 + .9C_2H_5 + .9CO + .1CH_2CO + .1CH_3$	1/10	(R 7)

All the above reaction rate modifications were incorporated into an adjusted POLIMI mechanism (referred here as Adjusted POLIMI Mechanism). Note that the intention was not to provide a new propanal kinetic mechanism but rather to call further attention to those reaction rates and branching ratios listed in Table 5-2 for future studies. Figure 5.6 (a) and (b) indicates comparison of experimental methane and propanal mole fraction time-histories with the two forms of the POLIMI mechanism. The experimental measurements were obtained behind the reflected shock waves around 1 atm and at three different temperatures (1192 K, 1300 K, and 1388 K). Very good agreements were obtained using the adjusted POLIMI mechanism for both propanal and methane time-histories at all three temperatures compared to the original POLIMI [44] Mechanism predictions.

a)

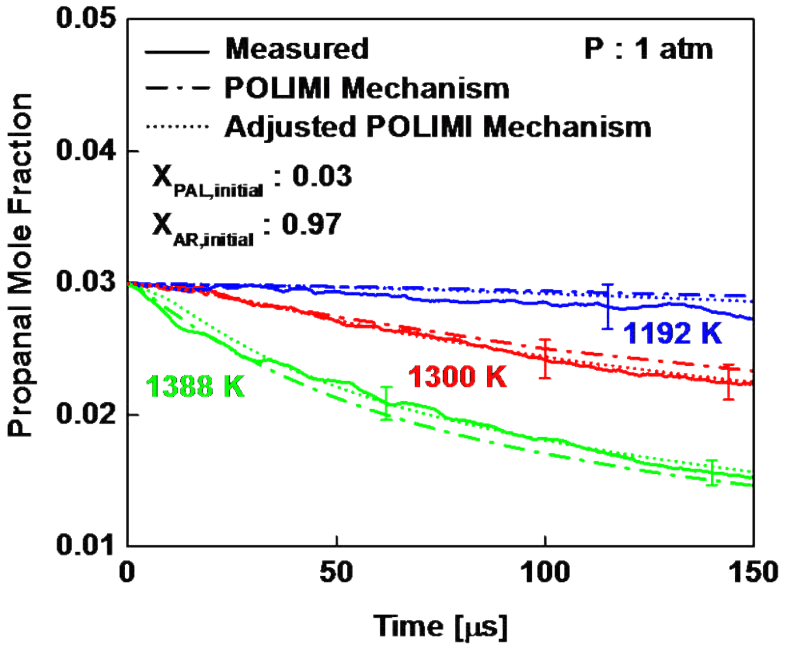

b)

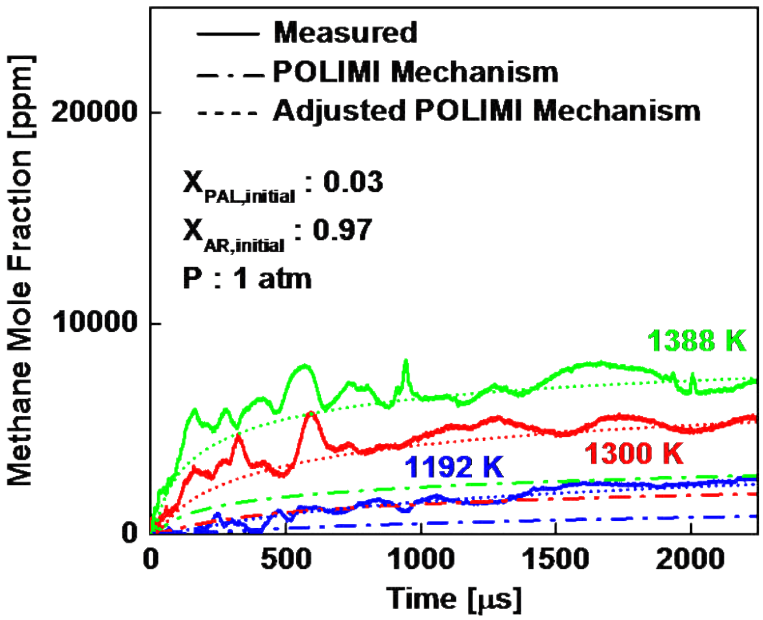

Figure 5.6 The comparison of experimental concentration time-histories with model predictions for **(a)** propanal and **(b)** methane at three temperatures 1192 K, 1300 K, and 1388 K around 1 atm.

5.3.3 Ignition Delay Time Results

Plotted in Figure 5.7 (a) is the current ignition delay time data along with results from literature shock tube studies by Akih-Kumgeh and Bergthorson [6] and Peluchi et al. [44]. All three studies are for a stoichiometric mixture of 1% propanal in argon bath gas. Note that the current study exhibited lower scatter and the experimentally obtained curve fit equation at 1 atm had a correlation coefficient (R^2) greater than 0.99. Figure 5.7 (a) displays propanal ignition delay times at three other pressures: 3 atm (ref. [44]), 6atm (current data), and 12 atm (ref. [6]). Current experiments at 6 atm exhibited similar activation energies as seen in 1 atm data. As expected, ignition delay times decreased as both pressure and temperature were increased.

Figure 5.7 (b) compares current ignition delay time results at 1 atm with predictions of three literature kinetic mechanisms (NUIG [44], POLIMI [44], and McGill [6] Mechanisms) and the adjusted POLIMI Mech. In general, all three literature kinetic mechanisms reasonably captured current data, however, the adjusted POLIMI Mechanism predictions are within the experimental uncertainties at both the highest and lowest temperature region. Also, the adjusted POLIMI Mechanism estimated the experimental activation energy with a better agreement. When Figure 5.7 (a) and (b) are compared, it is clear that ignition delay time values according to all three literature mechanisms are closer to current data than those measurements by previous authors [6,44] at 1 atm. A very recent study by Yang et al. [99] reported an empirically obtained ignition delay time correlation for propanal ignition. The measurements were taken using a shock tube. The experimental measurement results of the current study matched these values quite well as shown in Figure 5.7 (b).

a)

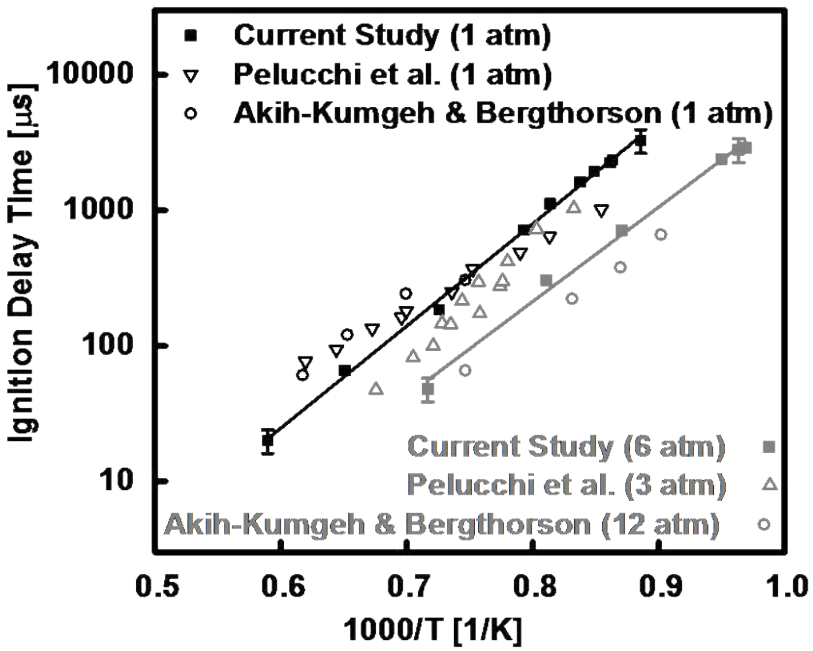

b)

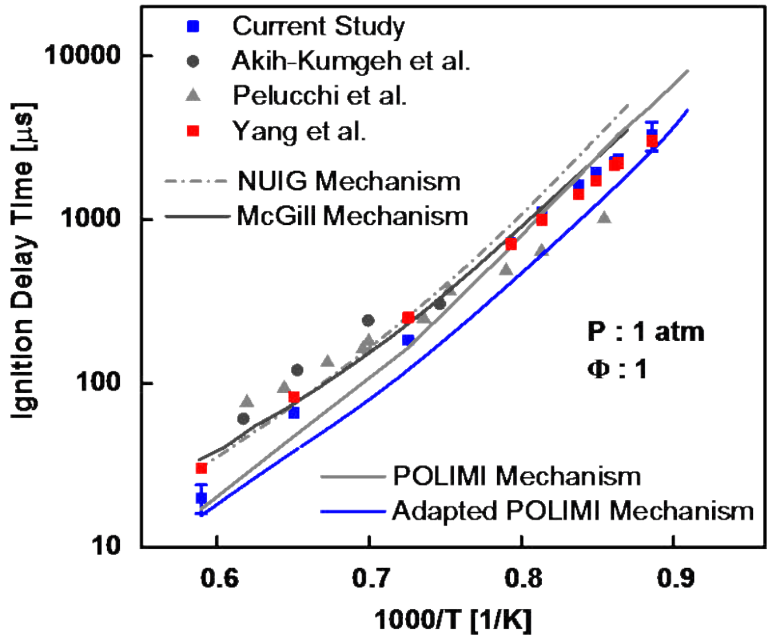

Figure 5.7 (a) Propanal ignition delay times measured behind the reflected shock waves at four different pressures around 1, 3, 6, and 12 atm. (b) The comparison of the experimental ignition delay time values with the model predictions at 1 atm.

5.4 Conclusions

Propanal is an important combustion intermediate formed during burning of both fossil and oxygenated fuels. In this study, propanal and methane concentration time-history measurements were conducted behind reflected shock waves at atmospheric conditions during 3% propanal pyrolysis (in argon) in a temperature range between 1192 and 1388 K. Measurements were conducted with a continuous wave distributed feedback interband cascade laser centered at 3403.4 nm using laser absorption strategies. The current measurements were the first methane and propanal concentration time-histories in the literature during propanal pyrolysis. In addition, ignition delay times of propanal (1% propanal in O_2/Ar, $\Phi = 1$) between 1129 K and 1696 K and at pressures of 1 and 6 atm were determined using pressure and CH* emission traces taken at the sidewall location of the shock tube test section. Current ignition data had lower scatter compared to those in the literature.

Predictions of three literature kinetics mechanisms (NUIG [44], POLIMI [44], and McGill [6] Mechanisms) indicated that POLIMI Mechanism [44] provided better agreements with the experimentally obtained ignition delay time values and propanal time histories. The large discrepancies for methane mole fraction predictions by all three mechanisms emphasized the importance of branching ratios of the methyl radical formation pathway of the propanal decomposition reactions. Modifications to the propanal decomposition as well as the H abstraction reaction rates were suggested based on sensitivity analysis using the POLIMI Mechanism. The adjusted POLIMI Mechanism showed an excellent agreement for both methane and propanal species concentration time-histories as well as the ignition delay time data. Current

experiments provide crucial validation targets for refinement of future aldehyde kinetic mechanism development.

CHAPTER 6: MEASUREMENTS IN EXCESS CO2 DILUTED OXY-METHANE COMBUSTION

6.1 Introduction

There are variations in the predictions of chemical mechanisms used for simulating the ignition delay times of natural gas such (e.g. GRI 3.0 and Aramco 1.3 Mechanisms) in CO_2 diluted gas mixtures. Figure 6.1 (a) gives the comparison of methane time-history predictions of two different reaction mechanisms; namely the GRI 3.0 and the AramcoMech 1.3 [45,46], for stoichiometric combustion of 3.5% CH_4 in argon bath gas diluted with 30% CO_2 at 1600K and 1 atm. The results were obtained using the constant- volume, constant internal energy (constant-U,V) assumption with the CHEMKIN PRO tool [18]. The discrepancy in the ignition delay time between the two mechanisms turned out to be $\Delta\tau_{ign}$ = 462.5 μs. Figure 6.1 (b) shows CH_4 time-histories during its ignition when the gas mixture contains different mole fractions of CO_2 ranging from 0 up to 60% according to the simulations done with the AramcoMech 1.3 mechanism. The differences in the ignition delay times were $\Delta\tau_{ign}$ = 293 and 236 μs when X_{CO2} was increased from 0 to 0.3 and 0.3 to 0.6, respectively.

Although not shown in Figure 6.1 (a) and (b), the discrepancies in the predicted ignition delay times between the two mechanisms were noticed in N_2 and Ar bath gasses even without any CO_2 dilution. These ignition delay time simulations at different bath gasses and CO_2 dilutions at 1600 K and 1 atm are summarized in Table 6-1. It can be seen from the table that as the CO_2 dilution was increased from 0 to 60%, the differences ($\Delta\tau_{dif}$) between the two mechanisms raised from 405.5 μs to 477.5 μs in argon bath.

a)

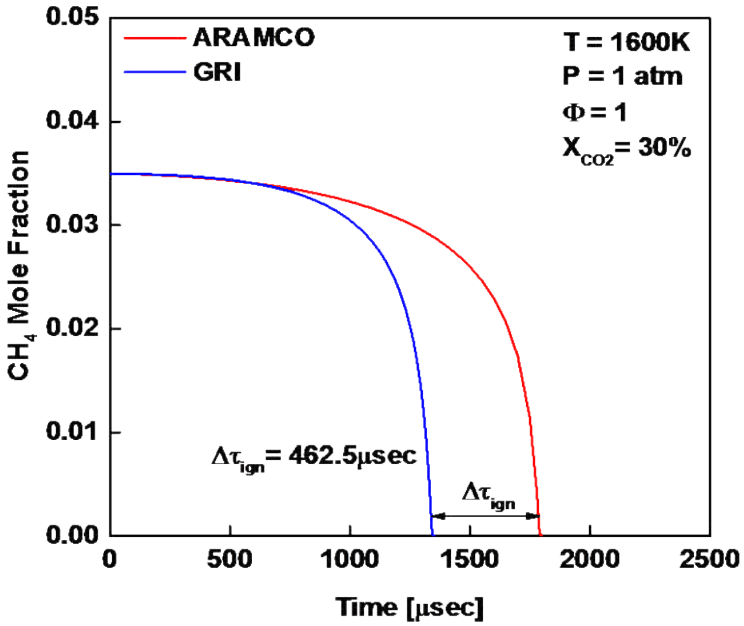

b)

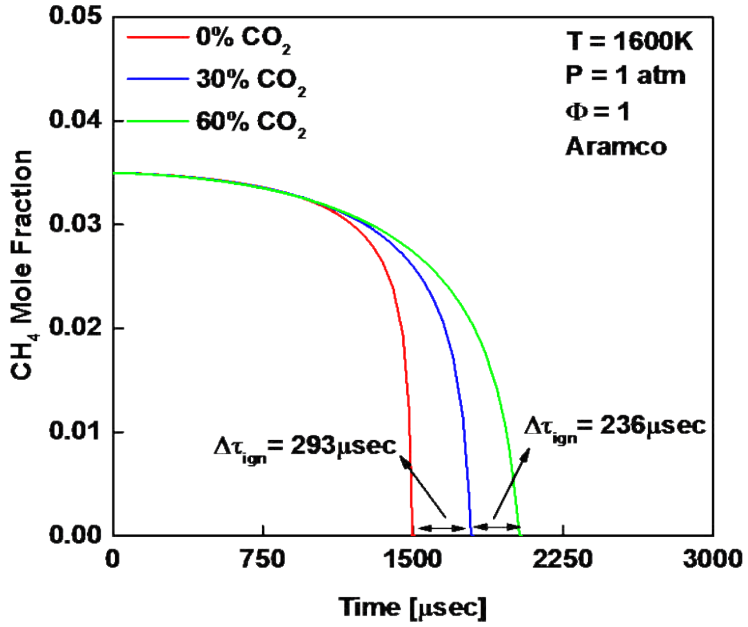

Figure 6.1 (a) Comparison of methane time-history predictions obtained from GRI 3.0 and AramcoMech 1.3 mechanisms for the stoichiometric combustion of 3.5% CH_4 and 30% CO_2 in argon bath gas at 1600K and 1 atm; (b) methane time-histories during its ignition when the bath gas contains different percentages of CO_2 ranging from 0 up to 60% according to the AramcoMech 1.3 mechanism.

Table 6-1- Ignition Delay Time Simulation Predictions at 1600 K and 1 atm

	X_{AR}	X_{N2}	X_{CH4}	X_{O2}	X_{CO2}	$\tau_{AramcoMech\ 1.3}$ [μs]	$\tau_{GRI\ 3.0}$ [μs]	$\Delta\tau_{dif}$
Ar bath	0.895	0	0.035	0.07	0	1495.5	1090.1	405.5
	0.595	0			0.3	1788.3	1325.8	462.5
	0.295	0			0.6	2024.9	1547.4	477.5
N_2 bath	0	0.895	0.035	0.07	0	1665.8	1164.8	501.0
	0	0.595			0.3	1865.8	1362.5	503.3
	0	0.295			0.6	2059.4	1560.0	499.4

However, the difference between the two mechanisms remained the same (499.4 μs < $\Delta\tau_{dif}$ < 503.3 μs) when nitrogen was used as the bath gas. Also, differences in the ignition delay times within the mechanisms themselves were seen as the CO_2 dilution was raised. This was already exemplified in Figure 6.1 (b), but further detailed in Table 6-1. As the CO_2 amount was increased, it was observed that the changes in the ignition delay time were more significant when the bath gas included argon (e.g. an increase from 1495.5 to 2024.9 μs for AramcoMech 1.3 mechanism) than nitrogen (e.g. an increase from 1665.8 to 2059.4 μs for AramcoMech 1.3 mechanism).

In this chapter ignition delay time measurements are reported for mixtures of CH_4, CO_2, and O_2 in argon bath gas at temperatures of 1577-2144 K, pressures of 0.53-4.4 atm, equivalence ratios (Φ) of 0.5, 1, and 2, and CO_2 mole fractions (X_{CO2}) of 0, 0.3, and 0.6. The measurements were done by utilizing the shock tube facility described in Chapter 3. The experimental data were compared to the predictions of two different kinetic models: GRI 3.0 and AramcoMech 1.3 mechanisms [45,46]. The ignition delay time measurements showed the influence of CO_2 dilution on the oxidation of methane. In addition, a laser absorption diagnostics was setup for measuring CH_4 time-histories behind the reflected shock waves using a continuous wave

distributed feedback interband cascade laser (DFB ICL) centered at 3403.4 nm. The present chapter also utilized the experimentally obtained correlations of absorption cross sections of CH_4 for its P(8) line in the v_3 band (λ = 3403.4 nm) in argon bath gas with (X_{CO2} = 0.3) and without (X_{CO2} = 0.0) CO_2 dilutions at temperatures of 1200 < T < 2000 K and pressures of 0.7 < P < 1.2 atm. The details of the correlations are given in Chapter 7. CH_4 time-histories during stoichiometric ignition of CH_4 with and without CO_2 dilution around 1 atm were also obtained through the aforementioned absorption cross section correlations. The current study provides the first shock tube measurements of ignition times and CH_4 time-histories in methane combustion with excess CO_2 dilution ($\geq$ 30%) in argon.

Figure 6.2 (a) shows the prediction results for the main products of ignition of stoichiometric methane and oxygen mixture (3.5% CH_4 and 7% O_2) in argon bath gas at 1600 K and 1 atm. The results were obtained from the AramcoMech 1.3 mechanism using CHEMKIN PRO simulations. Figure 6.2 (b) displays the absorption cross section of these main combustion products as well as that of methane around 3403.4 nm at 296K and 1 atm. It can be clearly seen that the main products have no or almost negligible absorption features around this wavelength region. Therefore, the measurements of the current study were done only at this peak wavelength (3403.4 nm). Note that these absorption cross section values were taken from the HITRAN database. Since the conditions behind the reflected shock wave (T_5 and P_5) are different for ignition experiments, measurements of the absorption cross section of methane at elevated temperatures were carried out. These measurements and the resulting empirical correlations for the absorption cross sections of methane are explained in Chapter 7.

a)

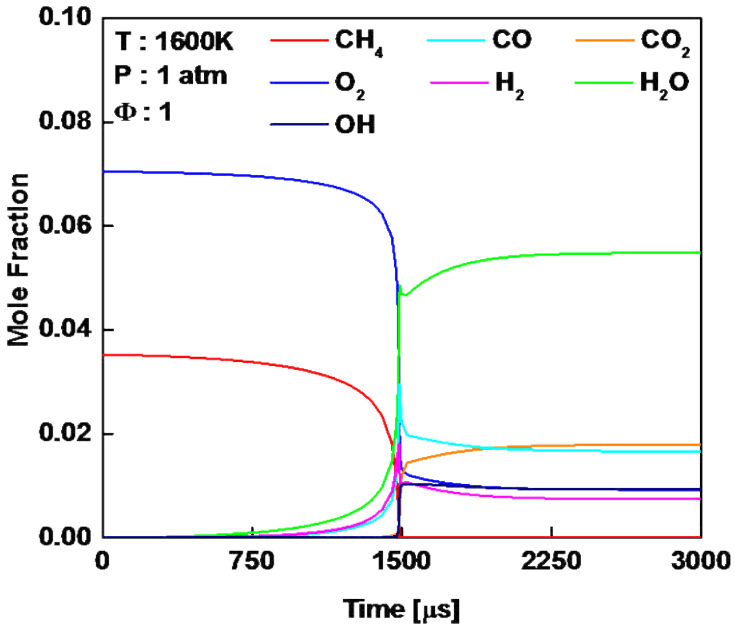

b)

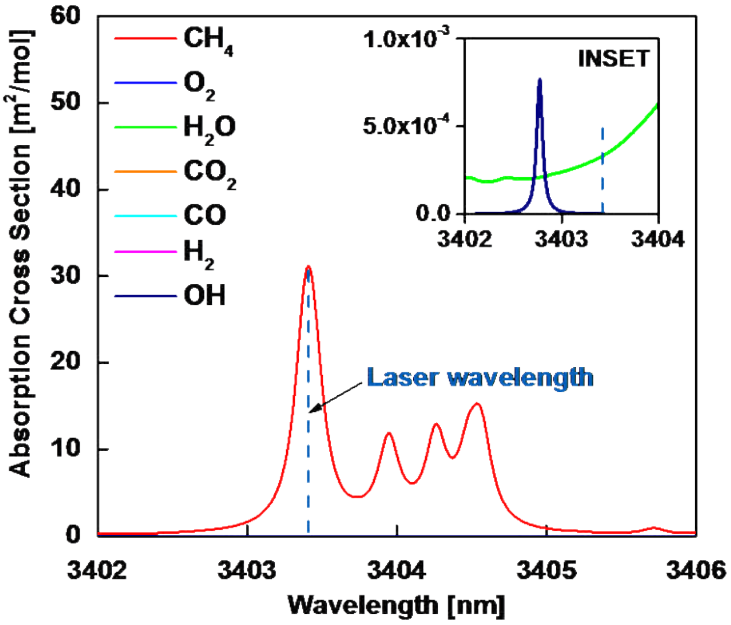

Figure 6.2 The AramcoMech 1.3 prediction results for the main products of the ignition of 3.5% CH_4 and 7% O_2 in argon at 1600K, 1atm; (b) HITRAN **[73]** absorption cross section values for the main products of the ignition of 3.5% CH_4 and 7% O_2 in argon at 296 K and 1 atm.

6.2 Results and Discussion

Table 6-2 includes a summary of the ignition delay time values measured behind the reflected shock waves for mixtures of $CH_4/CO_2/O_2$ in Ar bath gas at temperatures of 1577 < T < 2144 K, pressures around 1 and 4 atm, equivalence ratios (Φ) of 0.5, 1, and 2, and CO_2 mole fractions (X_{CO2}) of 0, 0.3, and 0.6. The uncertainties in the ignition delay time measurements were estimated to be less than ±20 %.

Table 6-2- Summary of Ignition Delay Time Experimental Data

P_5 [atm]	T_5 [K]	X_{CO2}	X_{CH4}	X_{O2}	X_{AR}	Φ	τ [μs]
0.882	1577						2142.2
0.87	1663						980.5
0.871	1792	0.0	0.035	0.07	0.895	1.0	352.1
0.835	1891						194.9
0.886	2144						38.5
0.818	1737						530.9
0.788	1801						382.3
0.776	1850	0.3	0.035	0.07	0.595	1.0	277.9
0.755	1903						185.2
0.731	1942						157.4
0.684	2022						104
4.038	1660						363.6
3.929	1706						232.0
3.868	1748	0.3	0.035	0.07	0.595	1.0	162.2
3.653	1807						100.1
3.602	1865						59.9
3.544	1904						38.9
0.814	1714						601.4
0.826	1791						370.8
0.829	1837	0.3	0.0175	0.07	0.6125	0.5	269.5
0.766	1846						262.7
0.725	1877						154.0
0.703	2012						90.3
4.104	1610						396.9
4.41	1613						391.7
4.035	1696	0.3	0.0175	0.07	0.6125	0.5	169.3
3.688	1760						105.5
3.722	1848						57.1
3.565	1881						40.5

P_5 [atm]	T_5 [K]	X_{CO2}	X_{CH4}	X_{O2}	X_{AR}	Φ	τ [μs]
0.68	1736						758.5
0.716	1812						427.6
0.721	1841						342.9
0.704	1857	0.3	0.07	0.07	0.56	2.0	311.5
0.681	1864						302.7
0.677	1921						190.3
0.615	1962						184.2
3.828	1632						535.2
3.562	1677						382.9
3.792	1684						337.9
3.897	1681	0.3	0.07	0.07	0.56	2.0	323.1
3.462	1736						233.9
3.355	1800						121.3
3.418	1884						52.3
3.288	1896						51.9
0.698	1799						465.9
0.641	1851						330.7
0.603	1960	0.6	0.035	0.07	0.295	1.0	196.4
0.528	2114						92.8
0.567	2091						89.5

6.2.1 Methane Ignition without CO_2 Dilution

Figure 6.3 shows the pressure and normalized CH* emission traces during the stoichiometric ignition of 3.5% CH_4 in argon at P_5 ~ 1.0 atm and T_5=1577 K. The CH* emission output from the detector was normalized to its peak (maximum) voltage. It can be clearly seen from Figure 6.3 that both the pressure jump and CH* emission peak occur around the same time. In this case, the ignition delay time can be obtained from either the pressure or emission; the discrepancy between them being less than 2%.

The comparison of ignition delay time measurement results of a stoichiometric mixture of 3.5% CH_4 in argon bath gas with GRI 3.0 and AramcoMech 1.3 mechanisms at different temperatures are provided in Figure 6.4. The experimental data were obtained behind reflected shock waves between 1577 K and 2144 K and at P ~ 1.0 atm. The experimental data matched the AramcoMech 1.3 mechanism predictions reasonably well for temperatures between 1600 and 1900 K; however, the GRI predictions were roughly 30% lower than the measured data. Both

mechanisms slightly over predicted the ignition delay time above 2000 K. Also, Figure 6.4 shows the shock tube ignition delay time measurements of a very recent study conducted by Aul et al. [100] for the stoichiometric ignition of methane at 1 atm in argon bath gas. The agreement between the two experimental measurements were very good especially around 1700 K. There are several other studies in the literature on methane ignition delay times [101-103]; however, the study of Aul et al. was chosen for comparison with present data due to its similarities in pressure, temperature, bath gas, and experimental setup.

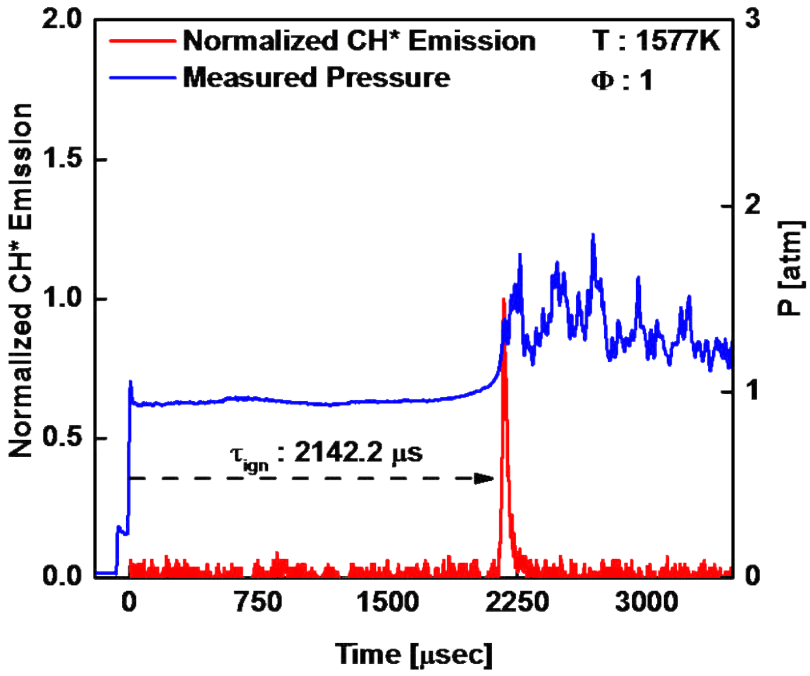

Figure 6.3 Pressure and normalized CH* emission traces during the ignition of 3.5% CH_4 and 7% O_2 in argon at P_5 ~ 1.0 atm and T_5=1577 K.

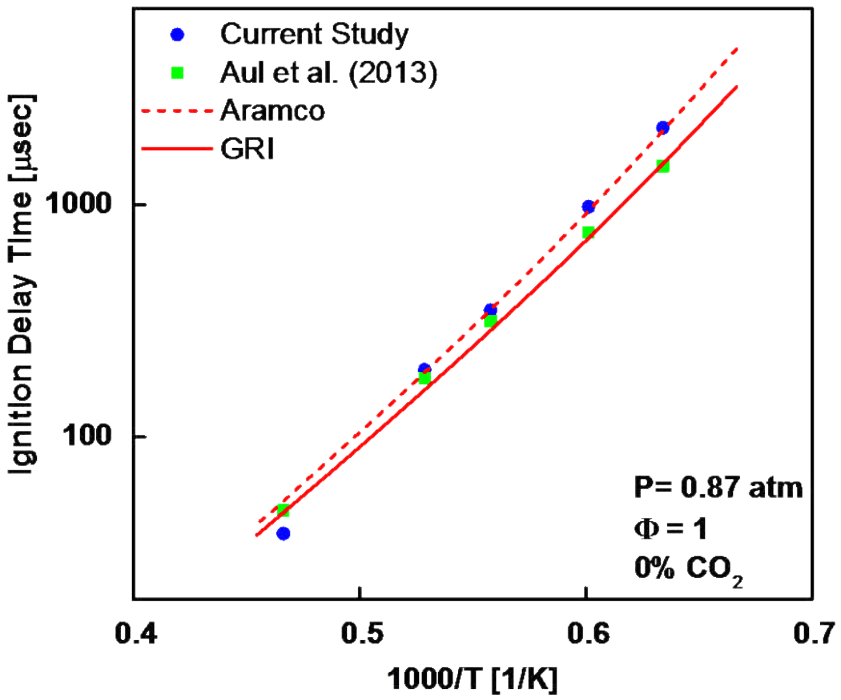

Figure 6.4 Comparison of measured ignition delay times with shock tube measurements of Aul et al. and predictions of the GRI 3.0 and the AramcoMech 1.3 mechanisms for stoichiometric (3.5% CH_4 and 7% O_2) mixtures in argon at P_5~ 1.0 atm.

Figure 6.5 provides the pressure and CH_4 mole fraction time-histories during the ignition of 3.5% CH_4 and 7% O_2 in argon. The experimental data were obtained behind the reflected shock wave at P_5 ~ 1.0 atm and T_5=1591 K. The steepest rise and fall of the pressure and methane mole fraction traces, respectively, very well matched each other at ignition. Figure 6.5 also displays the comparison of the CH_4 time-histories data with two different mechanism predictions. As shown the measured mole fraction time-histories closely followed the AramcoMech 1.3 mechanism predictions. Also, it can be seen from Figure 6.5 that the discrepancy in the ignition delay time at 1591 K between the current study and the AramcoMech 1.3 ($\Delta\tau_{ign}$ = 3 μs) was much less than that of the GRI 3.0 ($\Delta\tau_{ign}$ = 475 μs).

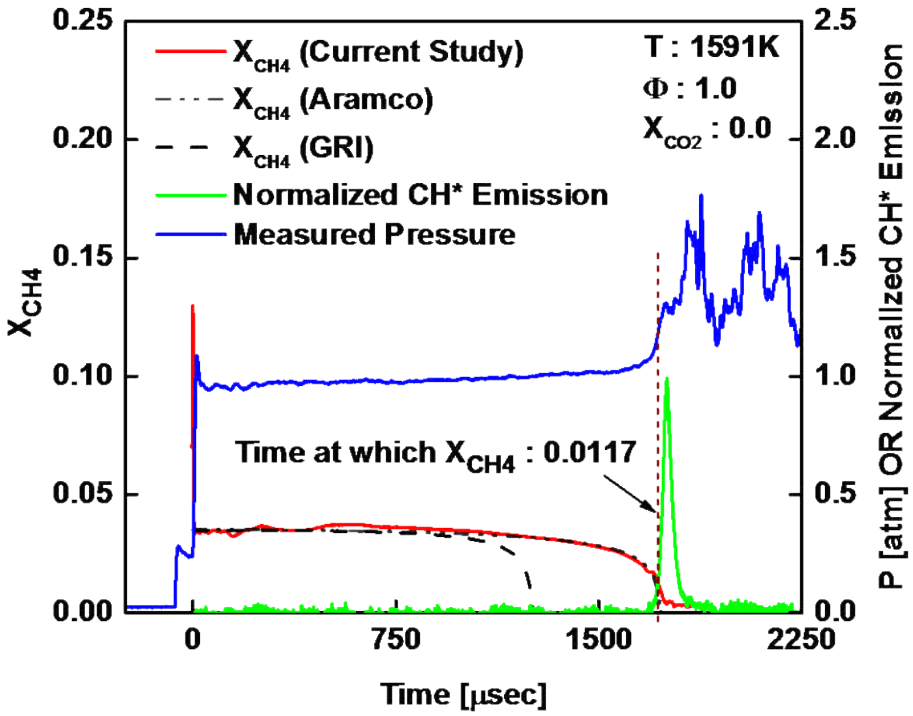

Figure 6.5 Pressure and CH_4 mole fraction time-histories during the ignition of 3.5% CH_4 and 7% O_2 in argon. The experimental data were obtained at P_5 ~ 1.0 atm and T_5=1591 K.

Note that in Figure 6.5 the measured methane mole fraction (X_{CH4}) values did not cease at zero, which might be due to the absorption of light at 3403.4 nm by water vapor as evidenced by the inset in Figure 6.2 (b) or by some other hydrocarbons that were formed as methane depleted before the ignition. However, the current experimental study results very well served for the purpose of confirming the AramcoMech 1.3 mechanism predictions by means of three different measurements: pressure, CH* emission, and CH_4 time-histories. Also, the laser schlieren spike was included in Figure 6.5. Due to the arrival of the reflected shock wave at the measurement location, abrupt density gradients occurred and they resulted in changes in the

refractive index. As a result, the schlieren spike appeared because of the deflection of the laser beam. Furthermore, Figure 6.5 included the time at which methane mole fraction decreased to one-third (X_{CH4} ~ 0.0117) of its initial value (X_{CH4} ~ 0.035). The reason for showing this mole fraction value is explained later in section 6.2.5.

The study of Pyun et al. [52] gave an empirical correlation for the differential absorption cross section of methane, measured at the peak and valley wavelength pair: λ_{peak} = 3403.4 nm and λ_{valley} = 3403.7 nm, for T=1000-2000 K and P=1.3-5.4 atm. In the current study, measurements of methane concentration time-histories were conducted during its ignition at the aforementioned peak and valley wavelength pair in order to see if the differential measurement could result in the methane mole fraction to cease at zero. The differential absorbance measurements showed complete extinction of methane when the ignition occurred. However, the use of Pyun et al. empirical correlation for these measurements resulted in the initial mole fraction of methane to be off by more than 15%. The reason for this was that the absorption cross section of methane varied significantly due to slight pressure variations and the pressure range of the present study (P ~ 1.0 atm) lied slightly out of the applicable range of the empirical correlation (1.3 < P < 5.4 atm) given by Pyun et al. [52]. In addition, measurements of methane cross section in a CO_2 diluted argon bath gas were done to see the effect of collisional broadening in the absorption cross section of methane. In the literature, there is no study giving the absorption cross section of methane measured in a bath gas of CO_2 around 3.4 μm at high temperatures pertinent to combustion. Detailed results for the absorption cross section of methane at the aforementioned peak and valley wavelengths at high temperatures around atmospheric pressures with and without CO_2 dilution are presented in Chapter 7.

6.2.2 Methane Ignition with CO2 Dilution

Provided in Figure 6.6 are the pressure and normalized CH* emission traces during the stoichiometric ignition of 3.5% CH_4 in Argon bath gas diluted with 30% CO_2 at P ~ 1.0 atm and T = 1800 K. It can be clearly seen from Figure 6.6 that the pressure rise was very gradual for this test mixture involving CO_2. Therefore, the ignition delay time measurements were consistently based off the time interval between the arrival of the shock wave obtained from the pressure trace and the onset of ignition indicated by the CH* emission.

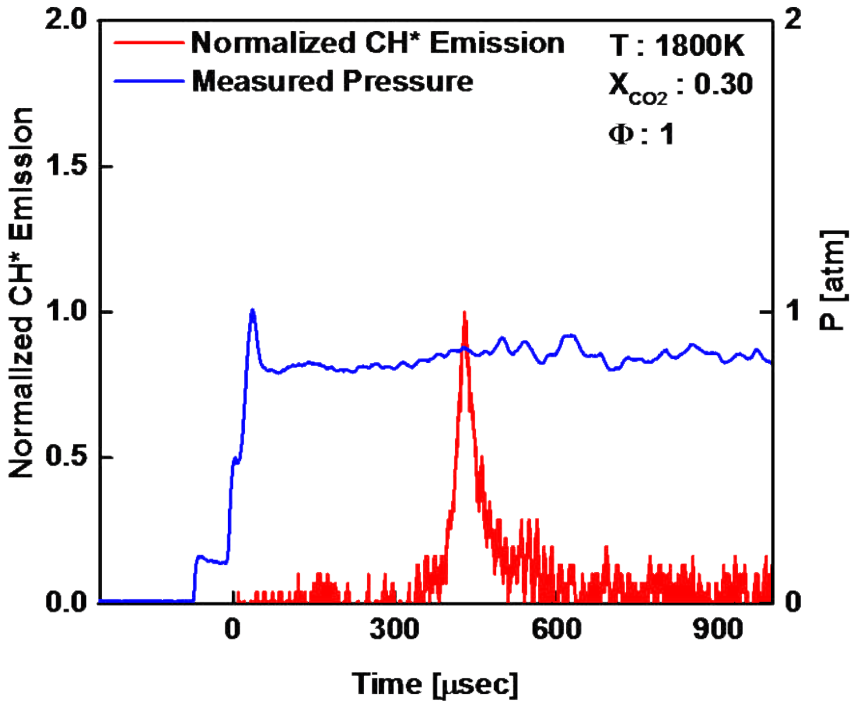

Figure 6.6 Pressure and normalized CH* emission traces during the ignition of 3.5% CH_4 and 7% O_2 in argon bath gas diluted with 30% CO_2 at P ~ 1.0 atm and T=1800 K.

Figure 6.7 plots the pressure and CH_4 time-histories during the ignition of 3.5% CH_4 and 7% O_2 in argon diluted with 30% CO_2 at P ~ 1.0 atm and T = 1801 K. Also, the comparisons of the experimental data with two different mechanisms predictions are shown. The measured mole fraction time-histories very closely followed the AramcoMech 1.3 mechanism prediction results. Also, it can be seen from Figure 6.7 that the discrepancy in the ignition delay time at 1801 K between the current study and the AramcoMech 1.3 was ($\Delta\tau_{ign}$ = 5 μs) much less than that of the GRI 3.0 ($\Delta\tau_{ign}$ = 54 μs).

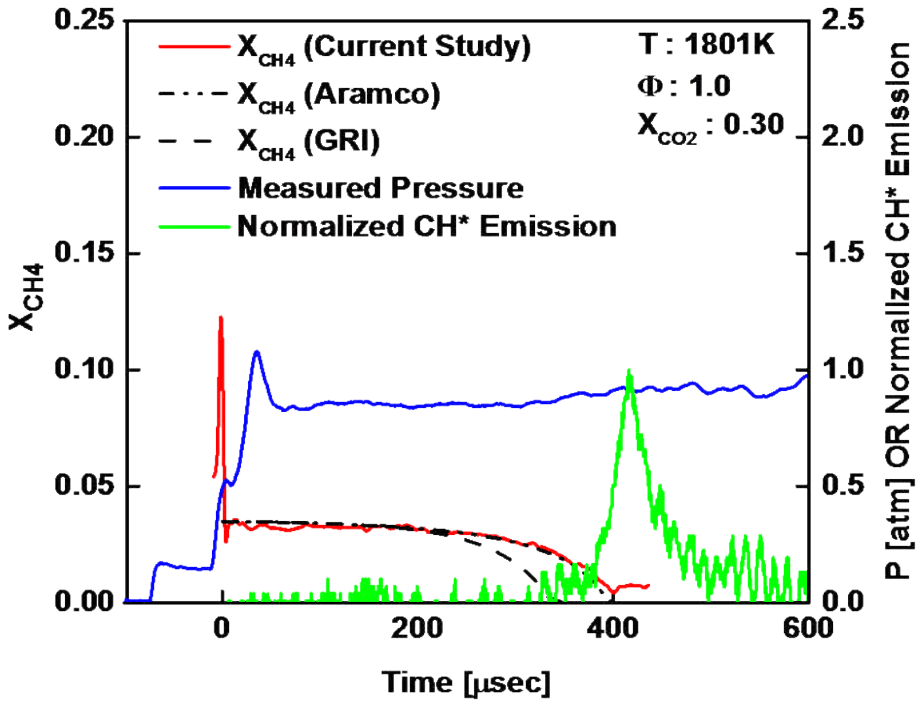

Figure 6.7 Pressure and CH_4 mole fraction time-histories during the ignition of 3.5% CH_4, 7% O_2, and 30% CO_2 in argon. The experimental data were obtained behind the reflected shock wave at P_5 ~ 1.0 atm and T_5 = 1801 K.

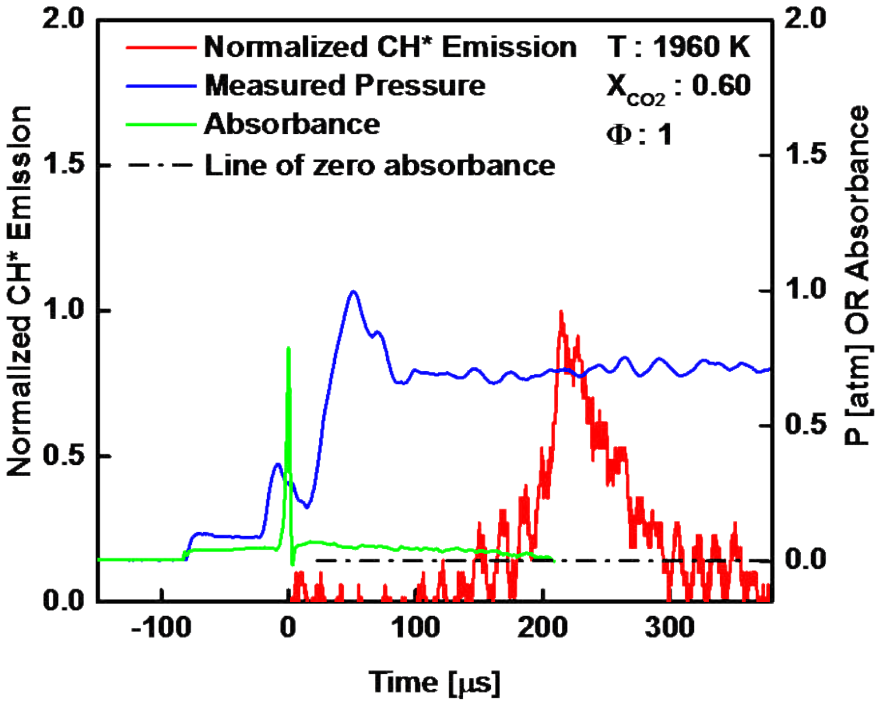

Figure 6.8 Pressure, normalized CH* emission, and the absorbance time histories during the ignition of 3.5% CH_4, 7% O_2, and 60% CO_2 in argon. The experimental data were obtained behind the reflected shock wave at P_5 ~ 0.65 atm and T_5 = 1960 K. The line of zero absorbance is also shown in the figure to indicate the time of depletion of CH_4 from the laser measurements.

Figure 6.8 shows the pressure, normalized CH* emission, and absorbance time histories during the stoichiometric ignition of 3.5% CH_4 in argon bath gas diluted with 60% CO_2 at P ~ 0.60 atm and T = 1960 K. The absorbance trace instead of methane mole fraction was displayed in the figure. The reason was that the measurements of the absorption cross section of CH_4 in 60% CO_2 diluted gas mixtures were not carried out because it was out of the scope of the current study. However, the line of zero absorbance was also given in the figure to indicate the time of depletion of CH_4. The pressure trace included in Figure 6.8 exhibited a significant bifurcation feature. The bifurcation seen in the measured pressure profiles of Figure 6.7 and Figure 6.8 occurred because the boundary layer did not have sufficient momentum to pass through the

normal reflected shock wave. The possibility of bifurcation increases with the amount of di-atomic/polyatomic molecules in the test gas mixture [104]. The severity of the bifurcation also increases as the γ (specific heat ratio) of the gas decreases. Therefore, the measured pressure profiles in Figure 6.7 and Figure 6.8 showed bifurcation since the gas mixtures involved 30 and 60% CO_2 (γ_{CO2} = 1.28), whereas no bifurcation was observed in Figure 6.5 due to the use of un-diluted monatomic bath gas Ar (γ_{Ar}=1.66). Owing to the same reasons, the pressure trace displayed a much stronger bifurcation in Figure 6.8 than that in Figure 6.8. Similarly, it was realized that the laser schlieren spikes illustrated in Figure 6.8 had higher peaks than those given in Figure 6.5 and Figure 6.7. However, the temporal width of the schlieren spikes were very similar for all three cases; namely, 0, 30, and 60 % CO_2 diluted gas mixtures. Thus the schlieren spikes indicated the arrival of the main reflected shock wave at the test location as detailed below.

When the bifurcation happens, the arrival of the main reflected shock wave (i.e. time zero) becomes questionable. However, Petersen and Hanson [105] pointed out that the arrival of the normal portion of the reflected shock wave can be accurately determined using a laser diagnostic that outputs a continuous wave (cw) beam. In fact, they provided experimentally obtained correlations based on the laser measurements to figure out the time zero from a side wall pressure measurement, if pressure is the only form of data available in a shock tube experiment. Since the current study made use of a cw laser source, the time zero was based off the laser schlieren spike during the ignition delay time measurements for CO_2 diluted gas mixtures.

The bifurcation also leads to concerns regarding the non-ideal effects due the boundary layer build up. However, the core section of the post-shock region consists of most of the flow area as discussed in [105] and therefore this portion still has the gasses at the calculated T_5 and P_5. As a result, the measured ignition delay time should not be altered due to the existence of a bifurcation feature as long as the ignition occurs at a temporal location in which the calculated P_5 (through shock velocity measurements) matches the measured P_5 (through Kistler pressure transducer). In other words, if the ignition delay time is to be accurately determined, the ignition should happen after the bifurcation is passed over (which is the case in the current study).

The comparison of ignition delay time measurement results from emission traces with the predictions of GRI 3.0 and AramcoMech 1.3 mechanisms at two different pressures around 1 and 4 atm, with 30% and 60% CO_2 dilution of the bath gas, for three different equivalence ratios: $\Phi = 1$, $\Phi = 0.5$, and $\Phi = 2$ are shown in Figure 6.9. Figure 6.9 (a) results were obtained by using 3.5% CH_4, 7% O_2, and 30% CO_2 in argon. It can be seen that the GRI 3.0 mechanism reproduced the activation energy better than the AramcoMech 1.3 predictions at low pressures. However, both mechanisms underpredicted the activation energy at high pressures. Also, at high pressures the simulation results obtained from AramcoMech 1.3 better matched the current study results at low temperatures, whereas the GRI 3.0 mechanism estimates had a smaller deviation from the experimental results at higher temperatures. Figure 6.9 (b) results were gathered from 1.75% CH_4, 7% O_2, and 30% CO_2 in argon. GRI 3.0 mechanism exhibited better agreement with regards to the activation energy and ignition delay time at both pressures in this case.

a)

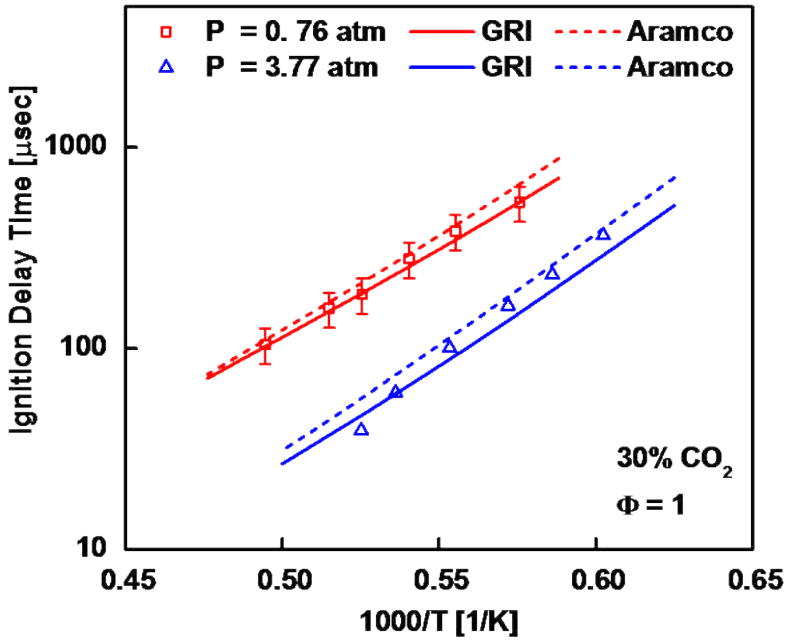
P = 0. 76 atm
GRI
Aramco
P = 3.77 atm
GRI
Aramco
Ignition Delay Time [μsec]
1000
100
10
0.45
0.50
0.55
0.60
0.65
1000/T [1/K]
30% CO2
Φ = 1

b)

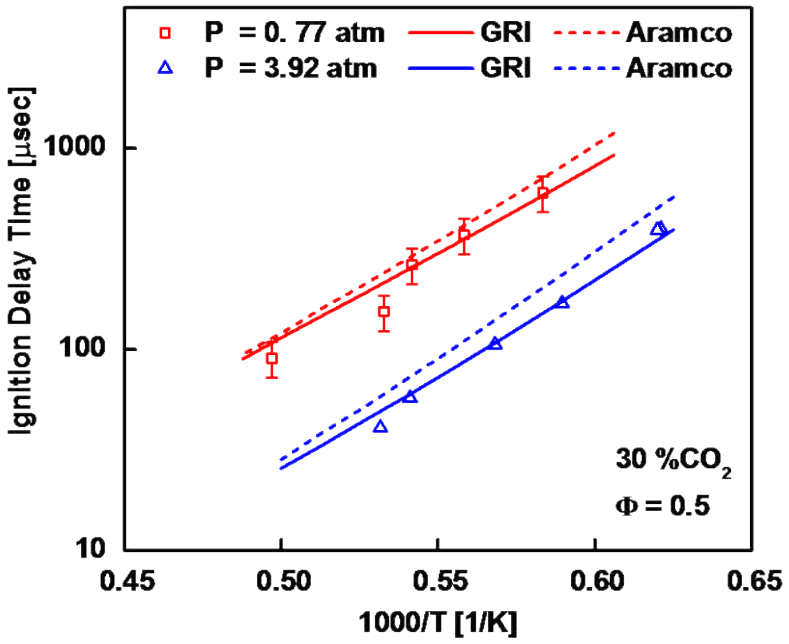
P = 0. 77 atm
GRI
Aramco
P = 3.92 atm
GRI
Aramco
Ignition Delay Time [μsec]
1000
100
10
0.45
0.50
0.55
0.60
0.65
1000/T [1/K]
30 %CO2
Φ = 0.5

c)

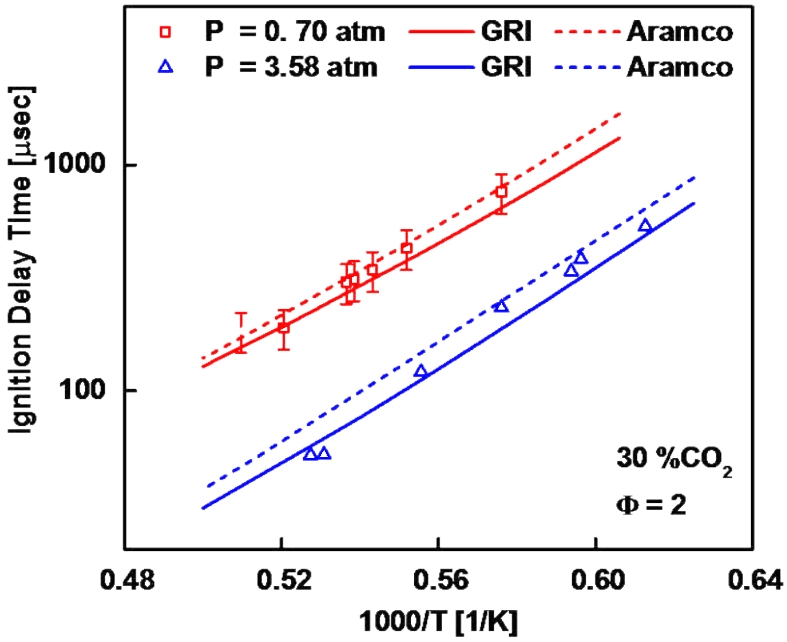

d)

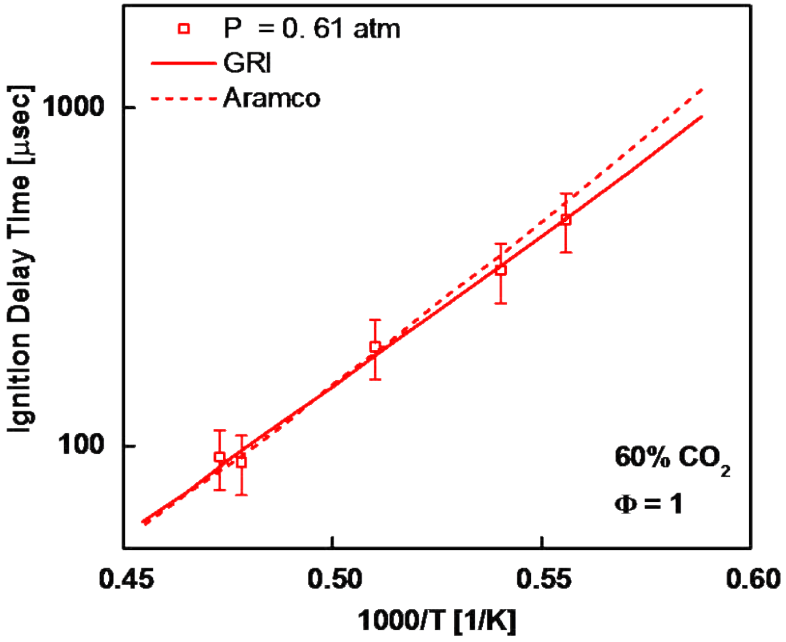

Figure 6.9 Comparison of ignition delay time data with GRI 3.0 and AramcoMech 1.3 mechanisms at different pressures around 1 and 4 atm for equivalence ratios of (a) 30%CO_2, Φ = 1, (b) 30%CO_2, Φ = 0.5, (c) 30%CO_2, Φ =2, and (d) 60%CO_2, Φ =1.

Figure 6.9 (c) compares results achieved by using 7% CH_4, 7% O_2, and 30% CO_2 in argon. The ignition delay time values of the present study at both pressures lied within the predictions of two mechanisms, however, the activation energies were underpredicted by both mechanisms. Figure 6.9 (d) shows ignition delay time results obtained from 3.5% CH_4, 7% O_2, and 60% CO_2 in argon. GRI 3.0 mechanism exhibited better agreement with regards to the activation energy and ignition delay time. In general it could be concluded that both mechanisms were able to reasonably predict the data taken with highly CO_2 diluted gas mixtures.

6.2.3 Empirical Correlations for the Current Experimental Data

The experimental data were fitted into the following form of the correlation

$$\tau = Ae^{E/RT} P^b \phi^c X_{CO2}{}^d \tag{6-1}$$

where the ignition delay times are in μs, temperatures are in K, pressures are in atm, and the activation energy is in kcal/mole. Using all the data taken with CO_2 diluted gas mixtures, the following empirical relation was obtained

$$\tau = 8.11x10^{-4}(\pm 2.50x10^{-4})e^{46,83\pm 1.10/RT} P^{-0.75\pm 0.021} \phi^{0.22\pm 0.020} X_{CO2}{}^{0.21\pm 0.058} \tag{6-2}$$

where the statistical uncertainties of the correlation parameters are also included. The curve fit represented the experimental data with a correlation coefficient greater than $R^2 > 0.98$. In order to better illustrate the effect of CO_2 dilution on the ignition delay time, the experimentally obtained correlation parameter, b, shown in Eq. (6-1) and given in Eq. (6-2) was utilized to scale the ignition delay time data to P = 1 atm as follows

$$\tau_{scaled} = \tau_{original} (1/P)^b \tag{6-3}$$

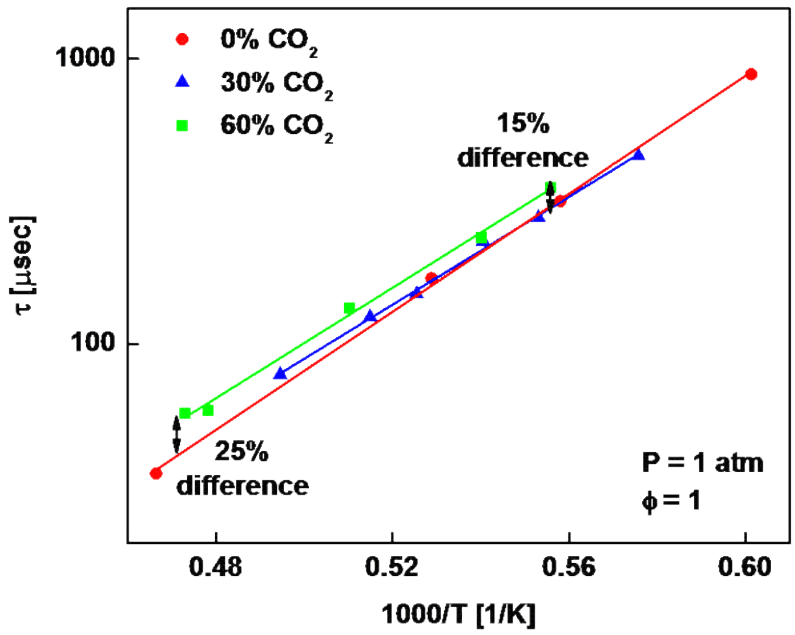

Figure 6.10 Comparison of scaled ignition delay time measurement results at 0, 30, and 60 % CO_2 dilutions. The results were scaled to 1 atm at stoichiometric conditions.

Figure 6.10 shows the scaled ignition delay time results. The scaling was implemented on the ignition delay time data taken at stoichiometric conditions (Φ =1) for three different CO_2 dilution percentages (X_{CO2} = 0, 0.3, and 0.6). For this data set, Table 6-2 showed that there were slight variations in pressure between $0.528 < P < 0.886$ atm. The scaled results of Figure 6.10 pointed out the very slight increases of ignition delay time as X_{CO2} was increased. When X_{CO2} was raised from 0 to 0.3, the increase in ignition delay time was very small (~10%) around 2000 K, whereas it became somewhat bigger (~25%) when X_{CO2} was further raised to 0.6. Similarly, the differences were small (~15%) at lower temperatures. Therefore, it can be concluded that the

changes in the ignition delay time of methane after CO_2 addition to the argon bath gas are within the experimental uncertainties.

6.2.4 Chemical and Thermodynamic Effects of CO_2 Addition

A brute force sensitivity analysis described in [106-108] was carried out for the ignition delay time measurement taken at 1737 K and 0.818 atm for stoichiometric ignition of 3.5% CH_4 in argon bath gas diluted with 30% CO_2. It was seen that the most dominant reaction in the system was the chain branching reaction as expected:

$$R_1 : H + O_2 \rightarrow O + OH$$

, whereas the seventh most dominant reaction was

$$R_2 : CO + OH \rightarrow CO_2 + H$$

It was clearly mentioned in a previous study by Liu et al. [37] that CO_2 was not an inert bath gas in the ignition of CH_4 and H_2 premixed flames. In fact, CO_2 competes for the H radicals through the reverse reaction of R_2, which results in a decrease in the concentration of the H radicals that participates in the chain branching reaction given by R_1. As a result, the fuel (CH_4) burning rate decreases as well. The current experimental results support this conclusion since ignition of methane in CO_2 diluted bath gas leads to longer ignition delay times.

There are mainly three influences of CO_2 addition on the ignition delay time of methane:

1) CO_2 can participate in chemical reactions through one of the most dominant reaction in the system which is R_2,

2) CO_2 has different third body collision efficiencies (α) in comparison to Argon or N_2,

3) CO_2 exhibits a much higher heat capacity (c_p) than argon and N_2.

The reaction rate of R_2 was determined by Joshi and Wang through RRKM/master equation analyses and Monte Carlo simulations [109]. In the present study, this reaction rate was doubled and halved in the AramcoMech 1.3 mechanism and the resulting ignition delay time results were compared to the original ones in Figure 6.11 (a). The simulations were done for stoichiometric combustion of 3.5% CH_4 in argon bath gas diluted with 60% CO_2 at 1 atm. The variation in ignition delay time due to the change in reaction rate of R_2 was insignificant with differences being slightly larger at higher temperatures. In addition, a similar ignition delay time comparison was carried out and shown in Figure 6.11 (b) by changing the collision efficiencies of CO_2. The original AramcoMech 1.3 mechanism had collision efficiencies (when compared to nitrogen) of CO_2 lying between 1.6 and 3.8 (average of them being $\alpha_{CO2} \sim 2.2$) for 29 different reactions, whereas these values were between 0.7 and 0.83 for argon (average of them being $\alpha_{Ar} \sim 0.71$). An ignition delay time comparison with the collision efficiencies of CO_2 doubled and halved was displayed in Figure 6.11 (b). When the collision efficiencies were varied, no change was noticed at low temperatures close to 1600 K, whereas somewhat larger differences (~ 37%) in the ignition delay time were seen at higher temperatures near 2000 K. Furthermore, the heat capacity of CO_2 ($c_{p,CO2}$ = 1.357 kJ/kgK) was almost three times higher than that of argon ($c_{p,Ar}$ = 0.52 kJ/kgK) above 1600 K. However, this difference manifested itself as a smaller pressure and thus temperature variation after ignition, when large amounts of CO_2 were employed in the gas mixture. This was evident by the large pressure fluctuations shown in Figure 6.3 and Figure 6.5 for the 0% CO_2 dilution case, whereas a much smaller change in pressure was observed in Figure 6.6 and Figure 6.7, and Figure 6.8 for the 30 and 60% CO_2 diluted gas mixtures, respectively.

a)

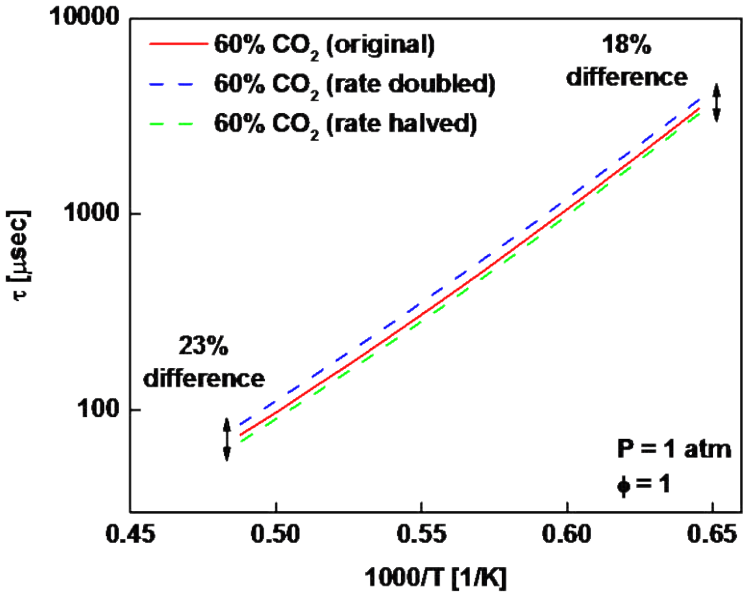

b)

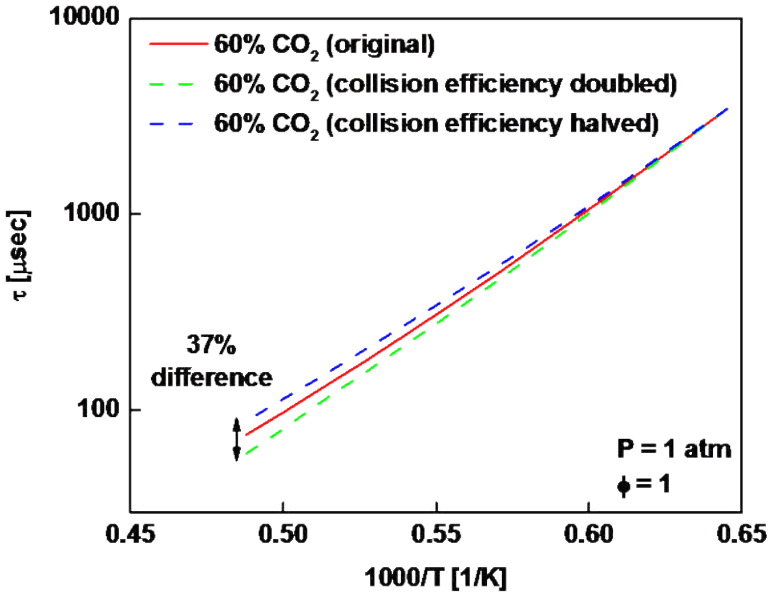

Figure 6.11 The variations in ignition delay time as a result of changing the (a) reaction rate of R_2 and (b) third body collision efficiencies of CO_2. The simulations were carried out using the AramcoMech 1.3 mechanism for the stoichiometric combustion of CH_4 at 1 atm with 60 % CO_2 dilution.

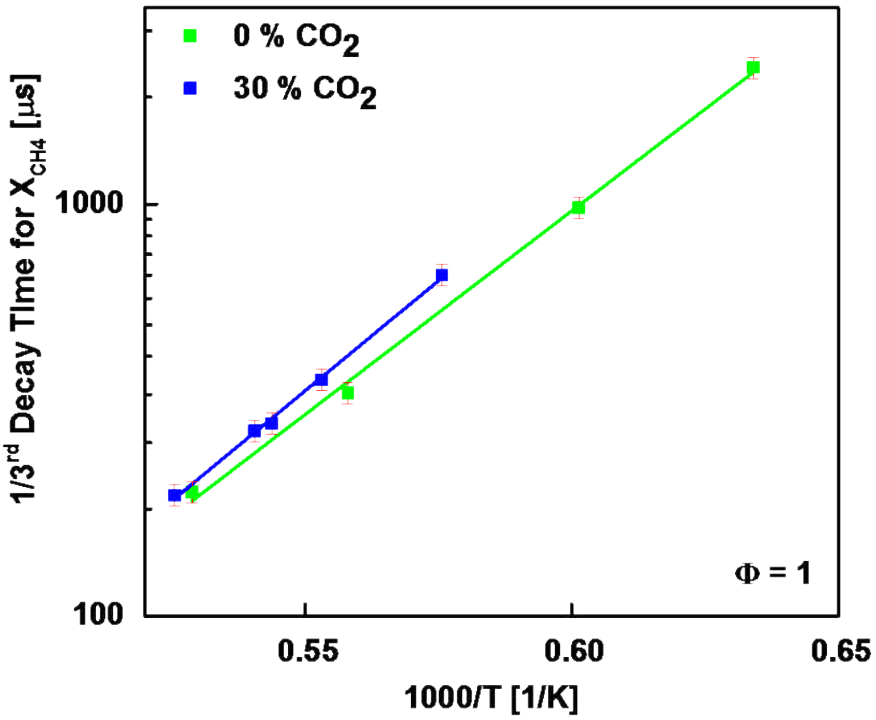

Figure 6.12 The laser absorption data for the initial CH_4 mole fraction (X_{CH4} ~ 0.0350) to fall to one-third of its initial value (X_{CH4} ~ 0.0117) for two different CO_2 dilutions (0 and 30%) at 1atm.

6.2.5 Methane Concentration Decay Times

There is uncertainty in the calculation of absorption cross section and mole fraction due to the errors in the measurements of pressure, temperature, absorbance, and path length. Similar uncertainty analyses were already detailed in section 4.4.3 of Chapter 4 as well as in section 7.3.5 of Chapter 7 and followed in this chapter as well. The resulting uncertainties of the current study were determined to be ±7% for methane mole fraction. The laser intensity fluctuations were also accounted for in this analysis. Similar uncertainties were reported for methane concentration measurements via laser absorption spectroscopy using similar types of DFB laser diodes in the infrared region [110]. The uncertainties in methane mole fraction measurements were much smaller than those of the ignition delay time measurements. Therefore, a time scale

measurement scheme according to the methane mole fraction decay was adopted in order to make a better comparison between data taken at different CO_2 dilutions. To accomplish that, the time that it takes for the initial methane mole fraction (X_{CH4} = 0.035) to decrease to one-third of its initial value (X_{CH4} = 0.0117) was plotted for different temperatures in Figure 6.12 for 0 and 30% CO_2 diluted gas mixtures. Recall that this time value was already exemplified in Figure 6.5. The increase in time for the methane mole fraction to decay as the CO_2 dilution was raised from 0 to 30% was 20% around 1740 K. Thus using the measured CH_4 time profiles, it can be concluded that the addition of CO_2 causes a delay in CH_4 decay. In summary, the CH_4 mole fraction measurements in this chapter aided in resolving the minor increase in decay times as a result of CO_2 dilution of the bath gas thanks to the low uncertainties of the mole fraction measurements.

6.3 Conclusions

In this chapter shock tube ignition delay time measurements are given for mixtures of CH_4, CO_2 and O_2 in argon bath gas at temperatures of 1577 < T < 2144 K, pressures around 1 and 4 atm, equivalence ratios (Φ) of 0.5, 1, and 2, and CO_2 mole fractions (X_{CO2}) of 0, 0.3, and 0.6. Methane concentration, CH* emission, and pressure time-histories measurements were conducted behind reflected shock waves to gain insight into the effects of CO_2 dilution on the ignition delay time of methane combustion. Current experiments are the first shock tube ignition experiments with excess CO_2 dilution (≥ 30%) for methane combustion in argon. Empirical correlations were obtained for ignition of methane at different CO_2 dilution percentages. The results pointed out that the changes in the methane ignition delay times as a result of CO_2

addition to the argon bath gas were not significant enough to be resolved in terms of the uncertainty of the ignition delay time measurements. However, the mole fraction traces had smaller uncertainties and thus helped gain insight into the changes in the methane decay time as the CO_2 dilution was increased. Also, the results were compared to the predictions of two different models: GRI 3.0 and AramcoMech 1.3 mechanisms. Both mechanisms were able to predict current data reasonably well with the AramcoMech 1.3 mechanism showing a better agreement. Sensitivity analysis was carried out to understand the important reactions. Three different influences in regards to chemistry, collision efficiencies, and heat capacities were examined as a result of CO_2 addition into the gas mixtures. The chemistry and global collision efficiency effects were found to be negligibly small to alter the ignition delay time of methane for the experimental conditions of interest.

CHAPTER 7: HIGH TEMPERATURE ABSORPTION CROSS SECTIONS OF METHANE NEAR 3.4 µm

7.1 Introduction

The use of laser absorption spectroscopy in shock tube experiments serves as a valuable tool for studying kinetics of chemical reactions. There are recent studies in the literature in regards to detecting methane in the infrared region for high temperature combustion applications. Sur et al. [110] developed a methane detection scheme by making use of two absorption lines (on-line minus off-line) in the R branch of v_3 band around 3175.8 nm and exemplified the technique for measurements of methane concentration during C_3H_8 pyrolysis in shock tube experiments. Another similar study conducted by Sajid et al. [111] used a quantum cascade laser and performed a differential wavelength scheme (peak minus valley) in the Q branch of v_4 band around 7671.7 nm. The P branch of v_3 band (asymmetric stretch) has also narrow and strong absorption lines which were utilized by Pyun et al. for developing interference-free detection of methane during n-heptane pyrolysis in shock tube experiments [52,53,92]. They reported empirical correlations for the differential absorption cross sections of methane in argon bath gas measured through the peak (λ_{peak} = 3403.4 nm) and valley wavelengths (λ_{valley} = 3403.7 nm) for temperatures of 1000 < T < 2000 K and pressures of 1.3 < P < 5.4 atm.

The effect of CO_2 on line intensities, pressure broadening, and narrowing coefficients of methane has also been investigated by very recent studies. Es-sebbar and Farooq [112] measured the aforementioned parameters for nine transitions of the P(11) manifold in the v_3 band of methane between 3438.8 and 3442.3 nm at 297 K. Various bath gases used were: N_2, H_2, He, Ar, and CO_2. Lyulin et al. [113] studied the CO_2 broadening and pressure induced shift coefficients

of methane spectral lines between 1628.7 and 1801.8 nm region at room temperature. In addition, Fissiaux et al. [114] used a tunable diode-laser spectrometer and examined the CO_2 broadening coefficients of 28 lines in the v_4 band of CH_4 between 7305.1 and 8052.8 nm. There are also studies comparing the effect of many bath gasses (Ar, He, and N_2) on the absorption cross section of methane measured using a He-Ne laser at a fixed wavelength of 3392 nm [115]. In the literature, there is no study on the absorption cross section of methane measured in CO_2 bath gas around 3403 nm at high temperatures.

In this study the absorption cross sections of methane were measured near the P(8) line in v_3 band at two wavelengths (λ_{peak} = 3403.4 nm and λ_{valley} = 3403.7 nm). Experiments were performed behind the reflected shock waves at high temperatures (1200 < T < 2000 K) and around atmospheric pressures (0.7 < P < 1.5 atm) in various methane/CO_2/Ar mixtures. The current study slightly extended the pressure range of the work of Pyun et al. [52] as well as provided the first measurements of cross sections in CH_4/CO_2 gas mixtures near 3403 nm.

7.2 Experimental Setup and Procedure

A continuous wave distributed feedback inter-band cascade laser (Nanoplus DFB ICL) was used for measuring methane (CH_4) absorption cross section and concentration time histories during methane ignition with and without CO_2 dilution. The two wavelengths were chosen near the P(8) line in v_3 band (λ_{peak} = 3403.4 nm and λ_{valley} = 3403.7 nm). This wavelength region was preferred for methane detection because methane has structurally resolved absorption features around 3.4μm, whereas most hydrocarbons have constant absorption coefficients. The interferences from other species are discussed in more detail below.

The absorption cross section of methane can be obtained from HITRAN database [73] at room temperature conditions. As a validation purpose, 0.5% CH_4 in N_2 bath gas was used to measure the absorption cross section of methane at room temperature (T = 299 K) and atmospheric pressure (P = 1 atm) in the shock tube. Current measurements were done both at the peak (λ_{peak} = 3403.4 nm) and valley wavelengths (λ_{valley} = 3403.7 nm). Table 7-1 shows the summary of results. The discrepancy between the present study and HITRAN database was less than ±1 %.

Table 7-1- Comparison of absorption cross section between the current study and HITRAN database

CH_4	Wavelength [nm]	Current Study	HITRAN	Difference
		σ_{CH4} [m^2/mol]	σ_{CH4} [m^2/mol]	%
Peak	3403.4	39.97	39.73	0.61
Valley	3403.7	3.56	3.60	-0.80

Figure 7.1 (a) shows the prediction results for the main products of ignition of stoichiometric methane and oxygen mixture (3.5% CH_4 and 7% O_2) in argon bath gas at 1600 K and 1 atm. The results were obtained from the Aramco 1.3 mechanism [46] using the constant volume and constant internal energy assumption with the CHEMKIN PRO tool [18]. Figure 7.1 (b) displays the absorption cross section of these main combustion products as well as that of methane around 3403.4 nm at 296K and 1 atm. The cross section values were taken from the PNNL and HITRAN databases [73,116]. Pyun et al. [52] measured the absorption cross sections of the interfering species (e.g. C_2H_6, C_2H_4, H_2O) at temperatures around 1200 K and pressures between 0.7 and 1.6 atm at the chosen wavelength pair. The high temperature spectra of formaldehyde can be obtained from the HITRAN database. The interferences and their effects in the uncertainty of the methane mole fraction measurement are explained in section 7.3.5.

a)

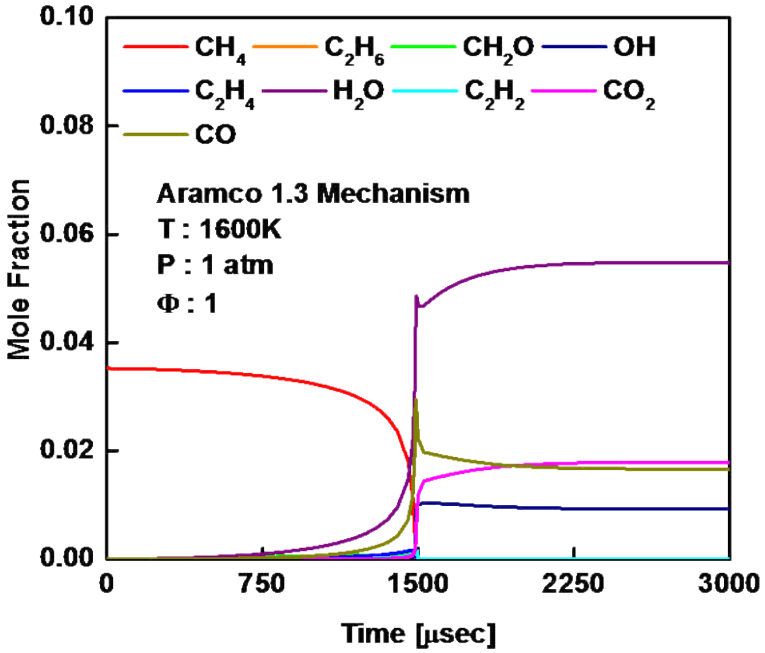

b)

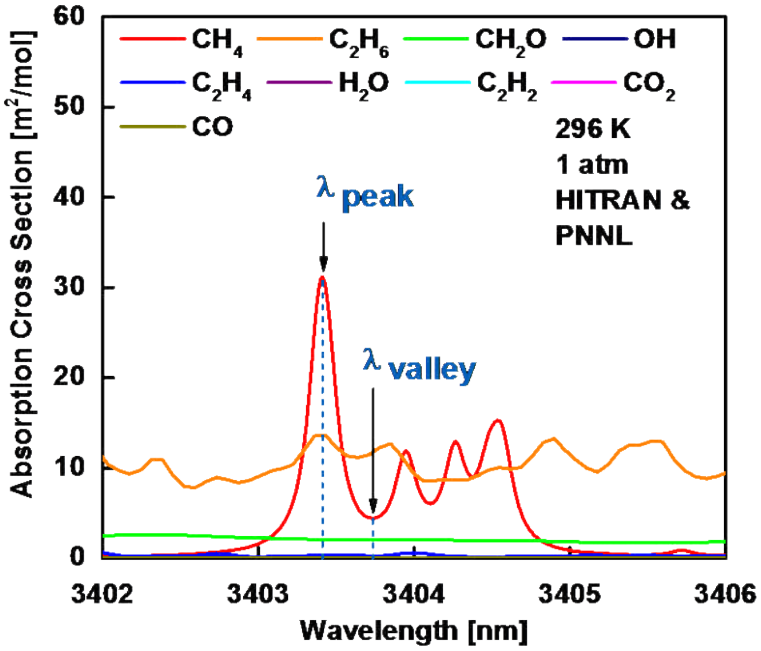

Figure 7.1 The Aramco 1.3 mechanism [13] prediction results for the main products of the ignition of 3.5% CH_4 and 7% O_2 in argon. Note: only the major interfering species until ignition is shown; (b) The absorption cross section values of major species at 296 K and 1 atm are shown.

7.3 Results and Discussion

7.3.1 Methane Absorption Cross Section in Argon Bath Gas

Figure 7.2 (a) shows a sample trace of the absorbance and pressure obtained at the peak wavelength of methane for an initial gas mixture of 2% CH_4 in argon at room temperature (T = 295 K). The mixture was shock heated to 1648 K behind the reflected wave. Figure 7.2 (b) displays the summary of the entire absorption cross section values measured between 1200 < T < 2000 K and 0.9 < P < 1.2 atm at the peak and valley wavelength pair. The peak wavelength data were fitted into the following equation

$$\sigma(T,P) = \sigma_o (\frac{T_o}{T})^{3.33} (\frac{P_o}{P})^{0.76} \tag{7-1}$$

where σ_o = 5.41 m^2/mole, T_o = 1500 K, and P_o = 1 atm. The following correlation was obtained for the differential cross section data

$$\sigma(T,P) = \sigma_o (\frac{T_o}{T})^{4.13} (\frac{P_o}{P})^{0.76} \tag{7-2}$$

where σ_o = 3.86 m^2/mole, T_o = 1500 K, and P_o = 1 atm.

a)

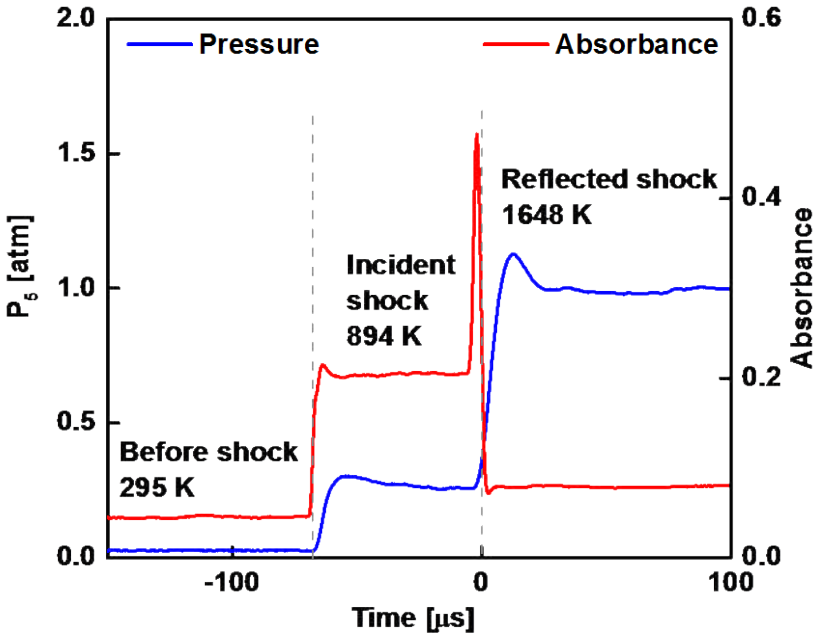

b)

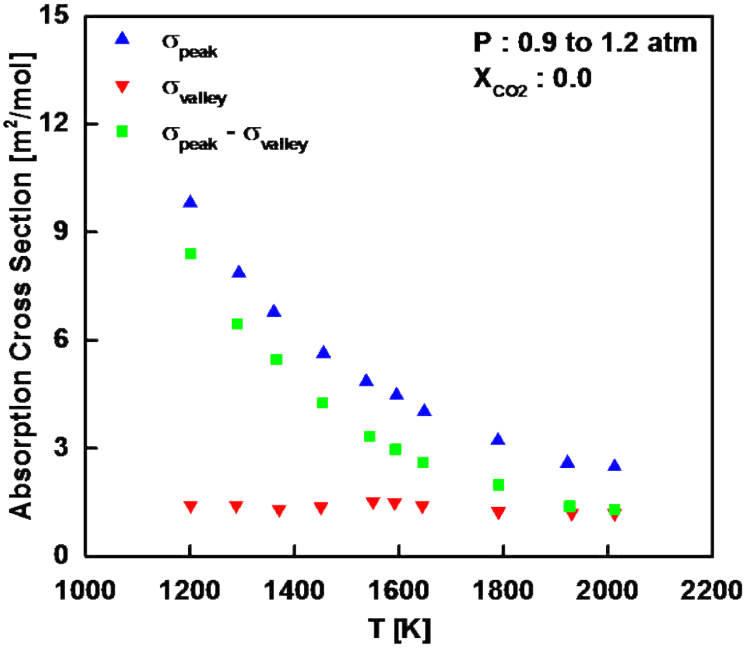

Figure 7.2 (a) Example absorbance and pressure traces for an absorption cross section measurement at the peak wavelength with an initial gas mixture of 2% CH_4 in argon, (b) the summary of the CH_4 absorption cross section values between 1200 < T < 2000 K and 0.9 < P <1.2 atm at the peak and valley wavelength pair.

The correlations given by Eq. (7-1) and (7-2) were used to achieve the concentration time histories of methane during its ignition. Figure 7.3 (a) shows the pressure and CH_4 mole fraction time histories measured at the peak wavelength during the stoichiometric ignition of 3.5% CH_4 and 7% O_2 in argon at P ~ 1.0 atm and T = 1591 K. Figure 7.3 (a) also displays the comparison of the experimental data with two different mechanisms predictions. The measured mole fraction time histories closely followed the Aramco 1.3 mechanism prediction results. Note that in Figure 7.3 (a) the measured methane mole fraction (X_{CH4}) values did not go to zero, which might be due to the absorption of light at λ_{peak} = 3403.4 nm by some other hydrocarbons that were formed as methane depleted before the ignition. Figure 7.3 (b) illustrates the results obtained through the differential absorbance measurements for the same temperature and pressure conditions as in Figure 7.3 (a). Although there was a slight deviation of the measured concentration profile from the Aramco 1.3 mechanism right before the ignition, the figure clearly shows that methane mole fraction completely went down to zero. Therefore, the interferences were completely eliminated by means of subtracting the absorbance at the valley wavelength from that at the peak. Note that the two-wavelength measurements resulted in a bigger noise compared to the single-wavelength measurement. Figure 7.3 (a) revealed that the magnitude of the concentration fluctuations at the early stages of ignition was higher than 3000 ppm, whereas Figure 7.3 (b) shows that the noise in the concentration measurement was more than 4500 ppm for two-wavelength measurements. The two-wavelength measurements were performed using a single laser with multiple runs and thus can lead to an increased noise. For example, there were temperature variations between different runs. However, these variations were kept below 10 K, which were well within the uncertainty limits.

a)

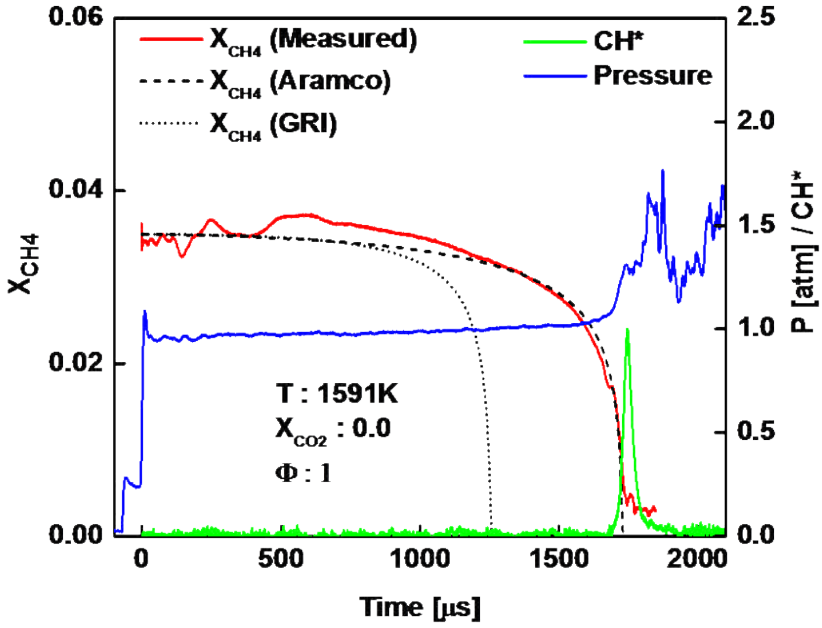

b)

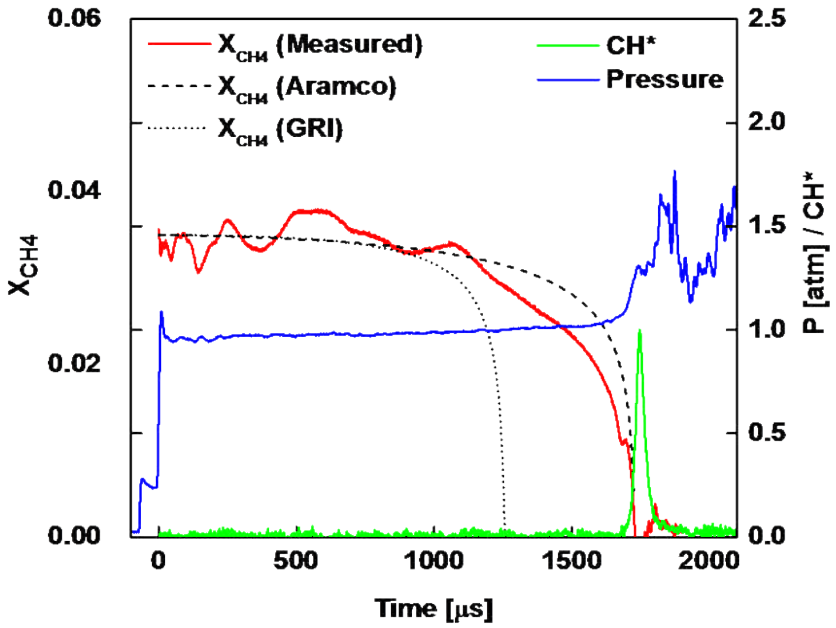

Figure 7.3 Comparison of measured methane mole fraction time history with the predictions results obtained from GRI 3.0 and Aramco 1.3 mechanisms **[45,46]** as well as the measured pressure and normalized CH* emission traces during the stoichiometric ignition of 3.5% CH_4 and 7% O_2 in argon bath at P ~ 1.0 atm and T = 1590 K: (a) at the peak wavelength, and (b) at the peak-valley wavelength pair.

7.3.2 Methane Absorption Cross Section in Argon Bath Gas Diluted with 30% Carbon-dioxide

Figure 7.4 (a) shows a sample trace of the absorbance and pressure obtained at the peak wavelength of methane for an initial gas mixture of 2% CH_4 and 30% CO_2 in argon at room temperature (T = 295 K). The mixture was shock heated to T = 1034 K behind the incident wave and then to 1830 K behind the reflected wave. Figure 7.4 (b) displays the summary of the entire absorption cross section values measured between 1400 < T < 2000 K and 0.7 < P < 1.0 atm at the peak and valley wavelength pair. The peak wavelength data were fitted into the following equation

$$\sigma(T,P) = \sigma_o (\frac{T_o}{T})^{3.39} (\frac{P_o}{P})^{0.76} \tag{7-3}$$

where σ_o = 5.14 m^2/mole, T_o = 1500 K, and P_o = 1 atm. The following correlation was obtained for the differential cross section data

$$\sigma(T,P) = \sigma_o (\frac{T_o}{T})^{4.93} (\frac{P_o}{P})^{0.76} \tag{7-4}$$

where σ_o = 3.57 m^2/mole, T_o = 1500 K, and P_o = 1 atm.

a)

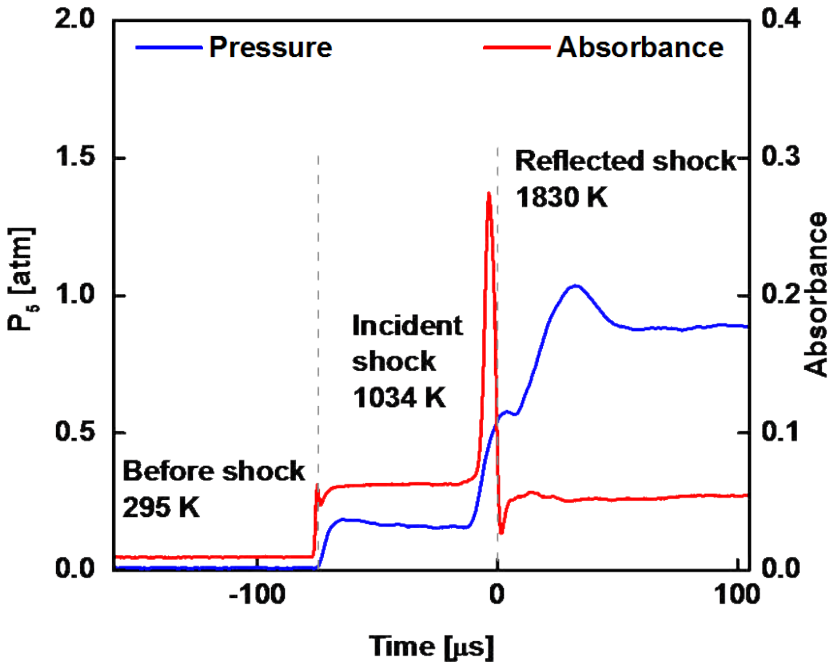

b)

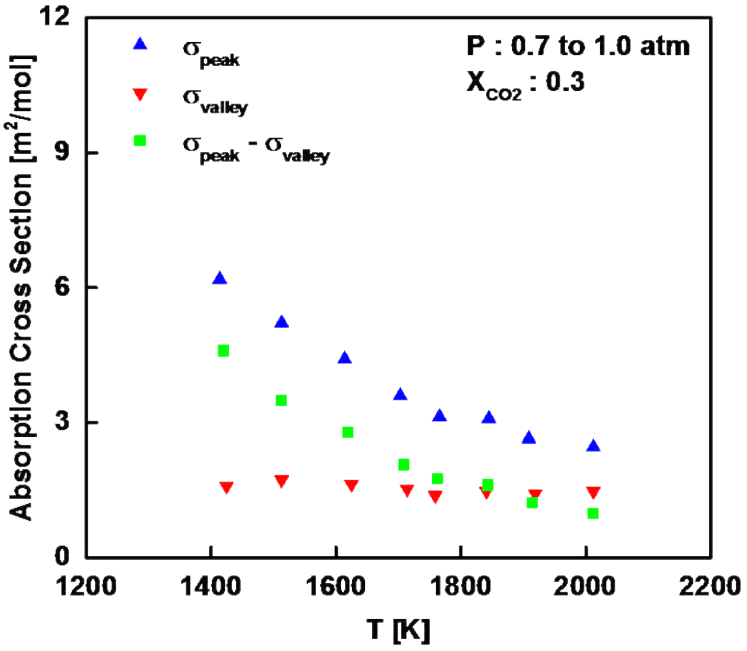

Figure 7.4 (a) Example absorbance and pressure traces for an absorption cross section measurement at the peak wavelength with an initial gas mixture of 2% CH_4 and 30% CO_2 in argon, (b) the summary of the CH_4 absorption cross section values between 1200 < T < 2000 K and 0.9 < P <1.2 atm at the peak and valley wavelength pair.

The correlations given by Eq. (7-3) and (7-4) were used to achieve the concentration time histories of methane during its ignition. Figure 7.5 (a) shows the pressure and CH_4 mole fraction time histories measured at the peak wavelength during the stoichiometric ignition of 3.5% CH_4, 7% O_2, and 30% CO_2 in argon at P ~ 1.0 atm and T = 1800 K. The measured mole fraction time histories again closely followed the Aramco 1.3 mechanism prediction results. Similar to Figure 7.3 (a) the measured methane mole fraction (X_{CH4}) values remained above zero in Figure 7.5 (a). However, Figure 7.5 (b) shows the results obtained through the differential absorbance measurements for the same temperature and pressure conditions as in Figure 7.5 (a). Similar to Figure 7.3 (b) methane mole fraction completely went down to zero with a small increase of fluctuations/noise in measured mole fraction.

a)

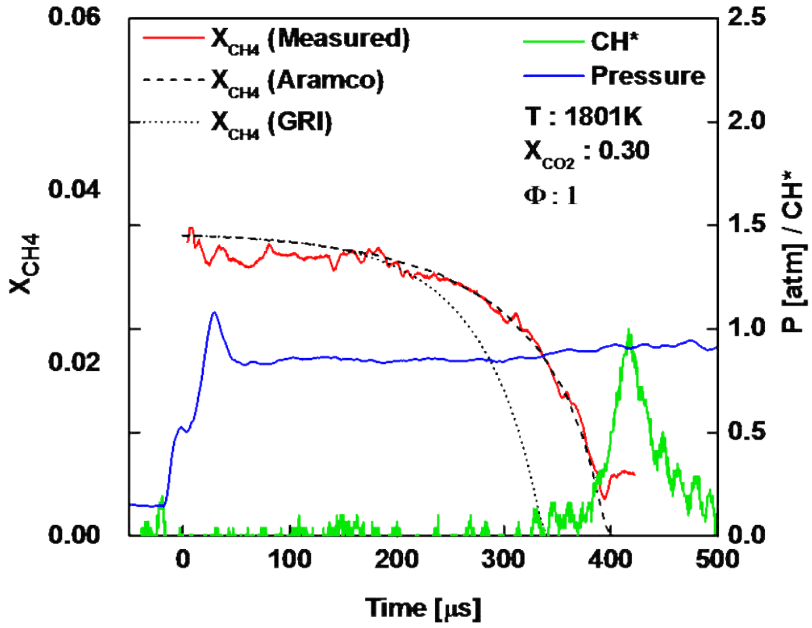

b)

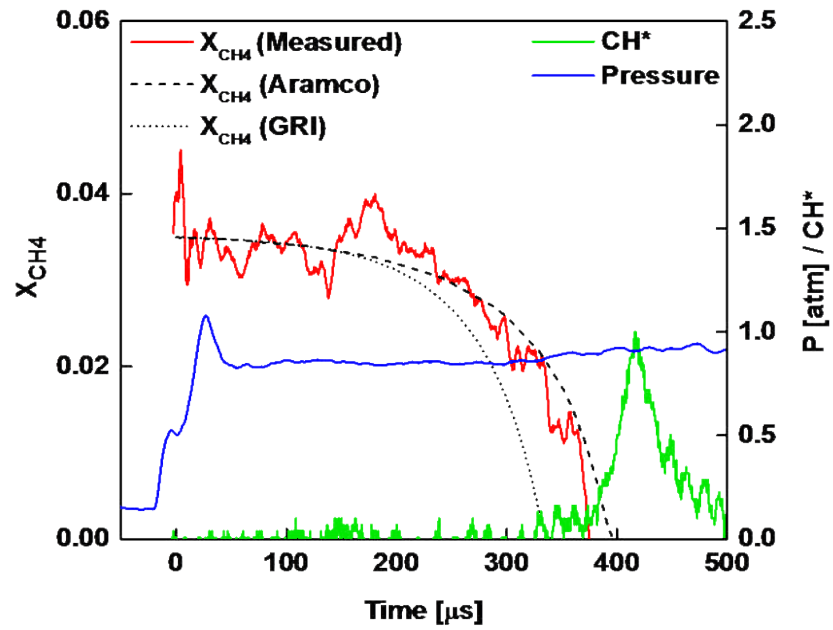

Figure 7.5 (a) Example absorbance and pressure traces for an absorption cross section measurement at the peak wavelength with an initial gas mixture of 2% CH_4 and 30% CO_2 in argon, (b) the summary of the CH_4 absorption cross section values between 1200 < T < 2000 K and 0.9 < P <1.2 atm at the peak and valley wavelength pair.

7.3.3 Methane Absorption Cross Section in 98% Carbon-dioxide Bath Gas

Figure 7.6 (a) shows a sample trace of the absorbance and pressure obtained at the peak wavelength of methane for an initial gas mixture of 2% CH_4 in carbon-dioxide at room temperature (T = 295 K). The mixture was shock heated to T_2 = 1116 K (incident wave) and then to 1885 K (reflected wave). Note that the bifurcation was observed in the measured pressure profiles of Figure 7.4 (a) and Figure 7.6 (a). It became very pronounced when the gas mixture contained 98% CO_2, and accordingly there was some variation in pressure and absorbance. The bifurcation happens when the boundary layer does not have sufficient momentum to pass through the normal reflected shock wave. The possibility of it increases with the amount of di-atomic/polyatomic molecules in the test gas mixture [104,105]. Also, the severity of bifurcation increases as the γ (specific heat ratio) of the gas decreases. Therefore, the measured pressure profiles in Figure 7.4 (a) and Figure 7.6 (a) showed bifurcation due to the gas mixtures comprised of 30 and 98% CO_2 gas (γ_{CO2} = 1.28), whereas no bifurcation was observed in Figure 7.2 (a) because of the use of un-diluted monatomic Ar bath gas (γ_{Ar}=1.66).

a)

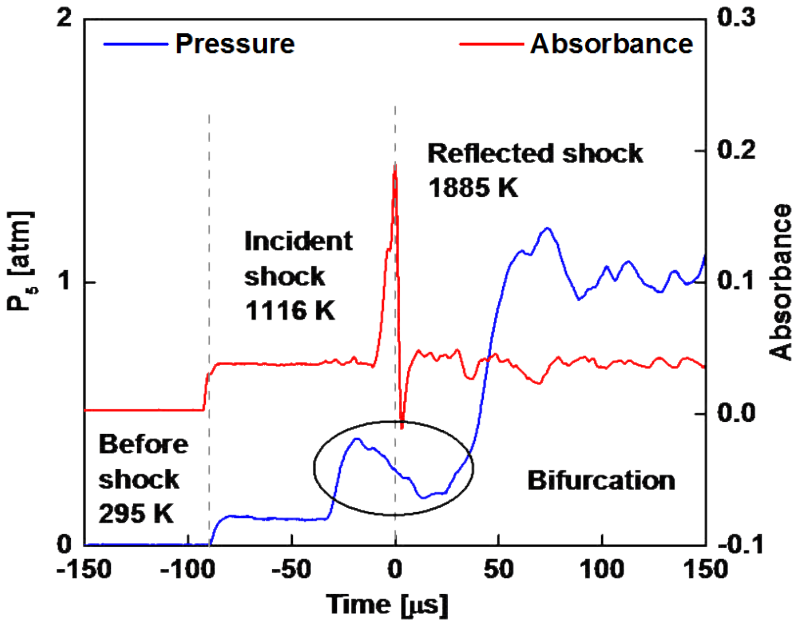

b)

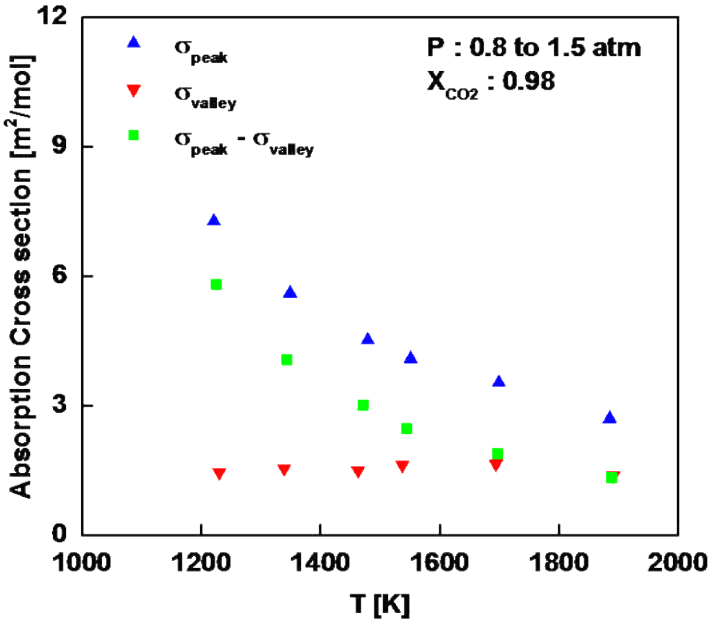

Figure 7.6 Example absorbance and pressure traces for an absorption cross section measurement at the peak wavelength with an initial gas mixture of 2% CH_4 in CO_2 bath gas, (b) the summary of the CH_4 absorption cross section values between 1200 < T < 1900 K and 0.8 < P < 1.5 atm at the peak and valley wavelength pair.

Due to the same reasons, the pressure trace displayed a much stronger bifurcation in Figure 7.6 (a) than that in Figure 7.4 (a). As a result, monoatomic bath gasses such as argon is preferred to avoid bifurcation when conducting experiments for the investigation of chemical kinetics.

Figure 7.6 (b) displays the summary of all absorption cross section values measured between 1200 < T < 1900 K and 0.8 < P < 1.5 atm at the peak and valley wavelength pair. The peak wavelength data were fitted into the following equation

$$\sigma(T,P) = \sigma_o (\frac{T_o}{T})^{3.16} (\frac{P_o}{P})^{0.76} \tag{7-5}$$

where σ_o = 5.02 m^2/mole, T_o = 1500 K, and P_o = 1 atm. The following correlation was obtained for the differential cross section data

$$\sigma(T,P) = \sigma_o (\frac{T_o}{T})^{4.44} (\frac{P_o}{P})^{0.76} \tag{7-6}$$

where σ_o = 3.14 m^2/mole, T_o = 1500 K, and P_o = 1 atm.

7.3.4 Comparison of Absorption Cross Sections at Various CO_2 Dilutions

In order to better understand the relationship between broadening of the absorption lines and absorption cross section, the following form of Beer Lambert law can be used

$$\alpha_\nu = -\ln\left(\frac{I}{I_o}\right)_\nu = S\phi_\nu PL = \sigma\frac{\chi}{RT}PL \tag{7-7}$$

where S [cm^{-2} atm^{-1}] is the line strength and ϕ_ν [cm] is the frequency-dependent lineshape function. The transitions at these pressures are almost Lorentzian and thus ϕ_ν is given by

$$\phi_\nu = \frac{1}{2\pi} \frac{\Delta\nu}{(\nu - \nu_0) + (\frac{\Delta\nu}{2})^2} \tag{7-8}$$

where ν_0 is the center frequency at which the transition occurs and $\Delta\nu$ is the width of the transition (FWHM). The frequency uncertainty because of pressure (collisional) broadening, $\Delta\nu_C$, is given by

$$\Delta\nu_C = P\sum_A \chi_A 2\gamma_{B-A} \tag{7-9}$$

where $2\gamma_{B-A}$ is the broadening coefficient. B is the species of interest (i.e. CH_4). A is the perturber (i.e. CH_4, Ar, or CO_2) that broadens the absorption line of B. Therefore, the broadening coefficient and the absorption cross section are inversely related to each other. A study conducted by Alrefae et al. [115] exemplified this point. They indicated that the methane absorption cross section measured with a HeNe laser at 3.392μm in three different bath gasses (He, Ar, and N_2) showed that the mixture of CH_4/He had the highest cross section, followed by CH_4/Ar, and CH_4/N_2 mixtures. This was explained by the fact that the broadening coefficients of CH_4 in He, Ar, and N_2 were reported in earlier studies [117,118] as 0.048, 0.056, and 0.063 cm^{-1}/ atm, respectively.

The broadening coefficients of CH_4/Ar and CH_4/N_2 mixtures at 295 K and 3403.4 nm were reported by Pine [117] as 0.04576 and 0.05271 cm^{-1}/atm, respectively. There is no study in the literature on the broadening coefficients of CH_4/CO_2 mixtures at the wavelengths studied in the present work. Figure 7.7 compares the absorption cross section of methane at 3403.4 nm for 2% CH_4 in a bath gas of argon, in a bath gas of argon diluted with 30% carbon-dioxide, and in a bath gas of carbon-dioxide. The absorption cross sections were calculated at 1 atm and at various

temperatures for three different cases based on the empirically obtained correlations given by Eqs. (7-2), (7-4), and (7-6) in order to better quantify the change in absorption cross section. It was seen that the absorption cross sections of methane at low temperatures decreased as the carbon-dioxide percentage in the mixture was increased. This might indicate that the broadening coefficient of a CH_4/CO_2 mixture was higher than that of a CH_4/Ar mixture. As the temperature was increased, the cross section values for different gas mixtures lied within the uncertainty limits. Although not shown in Figure 7.7, the same trends were observed at different pressures as well (e.g. 0.9 and 1.1 atm).

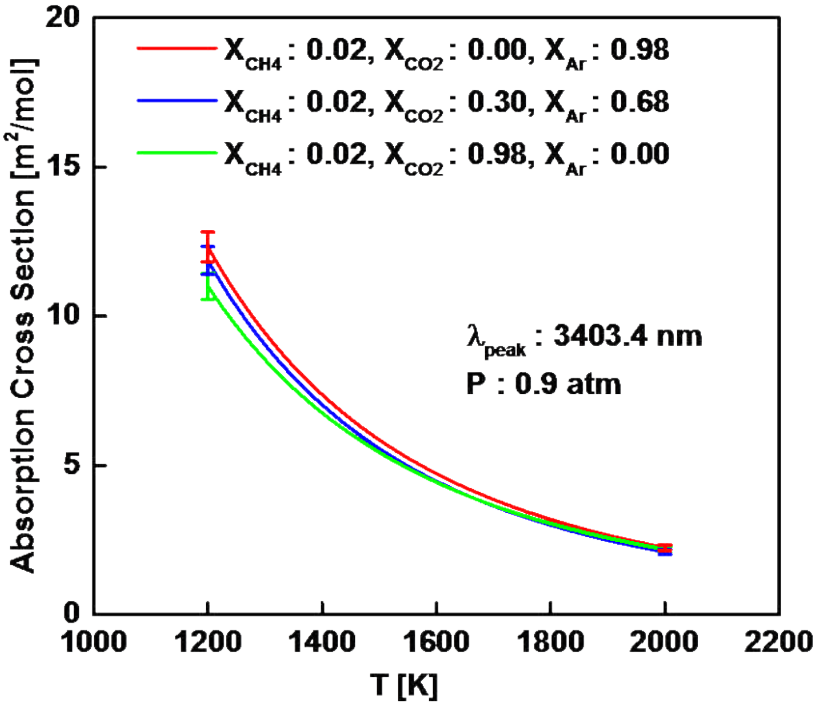

Figure 7.7 Comparison of absorption cross section of methane at 3403.4 nm measured with 2% CH_4 in argon (X_{CO2}=0), argon diluted with CO_2 (X_{CO2}=0.30, X_{Ar}=0.68), and in CO_2 (X_{CO2}=0.98).

7.3.5 Uncertainties in the Measurements of Absorption Cross-section and Mole Fraction

There is uncertainty in the calculation of absorption cross section and mole fraction due to the errors in the measurements of pressure, temperature, and path length. The resulting uncertainties of the current study were determined to be ±4 and ±7% for methane absorption cross section and mole fraction, respectively. The laser intensity fluctuations, the errors introduced due to the use of curve-fit equations for the methane absorption cross sections, and the interferences due to other species discussed earlier were all accounted for in this uncertainty analysis. Similar uncertainties were reported for methane concentration measurements via laser absorption spectroscopy using similar types of DFB laser diodes in the infrared region [110]. Note that methane mole fraction measurement results shown in Figure 7.3 and Figure 7.5 were obtained assuming constant temperature (T_5) and pressure (P_5) behind the reflected shock waves, which were calculated using the ideal shock relations [119]. However, the changes in T_5 and P_5 can influence the absorption cross-section and thus the mole fraction of methane. Therefore, simulations were run using the CHEMKIN PRO tool [18] and the Aramco 1.3 Mechanism [46] based on the constant volume-internal energy (constant-U,V) assumption. A very good agreement, which is within the uncertainty limits, between the measured and predicted pressure profiles was seen. Therefore, T_5 and P_5 time history predictions obtained from the Aramco 1.3 Mechanism were used in the conversion of the absorbance data into mole fraction. These mole fraction results were compared with the results shown in Figure 7.3 and Figure 7.5. The differences between the two profiles were within the uncertainties of the measurements.

7.4 Conclusions

The absorption cross sections of methane at two different wavelengths (λ_{peak} = 3403.4 nm and λ_{valley} = 3403.7 nm) were measured for three non-reactive gas mixtures: 2% CH_4 in argon and 2% CH_4 in argon diluted with 30% CO_2, and 2% CH_4 in CO_2. Present experiments were performed behind the reflected shock waves at high temperatures (1200 < T < 2000 K) and around atmospheric pressures (0.7 < P < 1.5 atm). The empirically obtained correlations indicated that CO_2 diluted gas mixtures decreased the absorption cross section of methane, which could be attributed to the broadening coefficient of a CH_4/CO_2 mixture being higher than that of a CH_4/Ar mixture. The laser absorption scheme was applied for measuring the methane mole fraction time histories during stoichiometric combustion of methane in argon bath gas with and without CO_2 dilution around atmospheric pressures. The results were compared to the predictions of two kinetics models: GRI 3.0 and Aramco 1.3 mechanisms [45,46] and indicated excellent agreement with predictions by the Aramco 1.3 mechanism. The current study presents the first high temperature measurements of the cross section of methane in CO_2 bath gas around 3403 nm. In addition, the current technique will enable measurements of methane concentration in CO_2 diluted combustion systems such as the oxy combustion systems.

CHAPTER 8: CONCLUSIONS

8.1 Summary of Results

A shock tube experimental setup was designed, built, and assembled by the current author during his doctorate study at UCF for studying chemical kinetics of propanal (CH_3-CH_2-CHO) pyrolysis and ignition as well as oxy-methane (CH_4) combustion. A laser absorption setup was built for propanal and methane detection at wavelengths of λ_{peak} = 3403.4 nm and λ_{valley} = 3403.7 nm. The gas phase infrared spectra of propionaldehyde (also called propanal, CH_3-CH_2-CHO) was studied using high resolution Fourier Transform Infrared (FTIR) spectroscopy over the wavenumber range of 750−3300 cm^{-1} and at room temperature 295 K. The calculated band-strengths were reported and the integrated band intensity results were compared with values taken from the Pacific Northwest National Laboratory (PNNL) database (showing less than 2% discrepancy). The peak positions of the 19 different vibrational bands of propanal were also compared with previous studies taken at a lower resolution of 1 cm^{-1}.

This dissertation also discusses the ignition delay times of propanal measured behind reflected shock waves for stoichiometric (Φ = 1) mixtures of propanal and oxygen in argon bath gas at temperatures of 1129 K < T < 1696 K and pressures around 1 and 6 atm. The results were compared to the data available in the literature as well as to the predictions of three propanal combustion kinetic models: POLIMI, NUIG, and McGill mechanisms. In addition, methane and propanal time-histories were measured during propanal pyrolysis behind the reflected shock waves using a continuous wave distributed feedback interband cascade laser at wavelengths of λ_{peak} = 3403.4 nm and λ_{valley} = 3403.7 nm. Methane and propanal concentration time-histories

were obtained during the pyrolysis of propanal at temperatures between 1192 K and 1388 K near 1 atm. Sensitivity analysis was carried out to understand the important reactions that were crucial during the pyrolysis of propanal. The large discrepancies for methane mole fractions predictions by all reaction mechanisms (POLIMI, NUIG, and McGill mechanisms) emphasized the importance of the branching ratios of the methyl radical formation pathway of the propanal decomposition reactions. Modifications to the propanal decomposition as well as the H abstraction reaction rates were suggested. The adjusted POLIMI Mechanism showed an excellent agreement for both methane and propanal species concentration time-histories as well as the ignition delay time data. Current experiments provide crucial validation targets for refinement of future aldehyde kinetic mechanism developments. Also the current measurements were the first methane and propanal concentration time-histories in the literature during propanal pyrolysis.

In this doctoral study, methane time-histories, CH* emission profiles, and pressure time-histories measurements were conducted behind reflected shock waves to gain insight into the effects of CO_2 dilution of the gas mixtures on the ignition of methane. The measurements were carried out for mixtures of CH_4, CO_2 and O_2 in argon bath gas at temperatures of 1577-2144 K, pressures of 0.53-4.4 atm, equivalence ratios (Φ) of 0.5, 1, and 2, and CO_2 mole fractions (X_{CO2}) of 0, 30%, and 60%. The laser absorption measurements were conducted using a continuous wave distributed feedback interband cascade laser (DFB ICL) centered at 3403.4 nm. The results showed the decrease of activation energy and the increase of ignition delay time as the amount of CO_2 dilution was increased. However, the changes were minor and within the experimental uncertainties of the measurements. Also, the results were compared to the predictions of two different natural gas mechanisms: GRI 3.0 and Aramco 1.3 mechanisms. In general the

predictions were reasonable when compared to the experimental data; however, there were discrepancies at some conditions. Three different influences of CO_2 addition to the argon bath gas in regards to chemistry, collision efficiencies, and heat capacities were examined. Current experiments were the first shock tube ignition experiments with excess CO_2 dilution ($\geq$ 30%) for methane combustion in argon. Empirical correlations were obtained for ignition of methane at different CO_2 dilution percentages. In addition, the shock tube and the laser system were used for measuring the absorption cross sections of CH_4 at two wavelengths (λ_{peak} = 3403.4 nm, λ_{valley} = 3403.7 nm) for three different non-reactive gas mixtures containing CH_4/Ar/CO_2 at 1200 < T < 2000 K and 0.7 < P < 1.5 atm. Three non-reactive gas mixtures were as follows: 2% CH_4 in argon and 2% CH_4 in argon diluted with 30% CO_2, and 2% CH_4 in CO_2. The empirically obtained correlations indicated that CO_2 diluted gas mixtures decreased the absorption cross section of methane, which could be attributed to the broadening coefficient of a CH_4/CO_2 mixture being higher than that of a CH_4/Ar mixture. The current absorption cross-section measurements provided the first high temperature methane cross sections data with excess CO_2 dilution ($\geq$ 30%) in a shock tube.

8.2 Publications

The research detailed in this dissertation has been published in the following journal papers:

- Koroglu B., Vasu S. S., "*Measurements of Propanal Ignition Delay Times and Species Time-Histories using Shock Tube and Laser Absorption*, International Journal of Chemical Kinetics, paper in review, 2016 [48].

- Koroglu B., Vasu S. S., "*High Temperature Absorption Cross Sections of Methane near 3.4 μm in Carbon-dioxide Diluted Gas Mixtures*", Chemical Physics Letters , paper in review, 2016 [50].
- Koroglu B., Pryor O., Lopez J., Nash L., Vasu S. S., "*Shock tube ignition delay time and methane time-history measurements during excess CO_2 diluted oxy-methane combustion*, Combustion and Flame, Vol. 164, pp. 152-163, 2016 [49].
- Koroglu B., Loparo Z, Peale R. E., Nath J., Vasu S. S., "*Propionaldehyde Infrared Cross-Sections and Band Strengths",* Journal of Quantitative Spectroscopy and Radiative Transfer, Vol. 152, pp.107-113, 2015 [47].

8.3 Recommendations for Future Work

In this doctoral study, a shock tube experimental facility was designed, assembled and tested. Shock tube is a very useful tool for studying the kinetics of chemical reactions. Measurements of ignition delay times for gas mixtures comprised of propanal/oxygen/argon as well as methane/oxygen/argon were taken behind the reflected shock waves at temperatures above 1200 K and at pressures around 1, 4, and 6 atm. However, this pressure range could be extended to higher values such as 10 and even 20 atm in order to have a better understanding of the ignition and thermal decomposition characteristics of these fuels for real engineering applications such as automotive engines and gas turbines.

The current research highlighted the need to investigate the propanal decomposition pathways because the experimental methane concentration profiles were quite off from the predictions of the reaction mechanisms. This indicated that the branching ratio of the propanal

decomposition reactions favoring the methyl radical formation channel was not correctly assigned by the previous studies. Although the current study provided both propanal and methane concentration time-histories during propanal pyrolysis, more species are required to be detected during the course of the experiments in order to better quantify the branching ratio. The FTIR measurements of the current study indicated that propanal does not have any absorption feature between 4.54 and 4.62 μm. In this wavelength region, carbon-monoxide (CO) has very strong and resolved absorption features. Therefore, measurements of carbon-monoxide during propanal pyrolysis between 1200 and 1500 K and at pressures around 1 atm are definitely suggested as another future work in order to accurately quantify the branching ratios of the propanal decomposition reactions.

LIST OF REFERENCES

[1] G. Oladosu, Applied Energy 99 (2012) 85.

[2] Y. Yang, J.E. Dec, SAE Technical Paper 2013-01-2627 (2013).

[3] G. Barari, B. Koroglu, S.S. Vasu, J.E. Dec, C.A. Taatjes, ESS Fall Technical meeting, Clemson, SC (2013).

[4] J. Badra, A. Elwardany, F. Khaled, S.S. Vasu, A. Farooq, Combust. Flame accepted, available online (2013).

[5] J.W. Allen, A.M. Scheer, C.W. Gao, S.S. Merchant, S.S. Vasu, O. Welz, J.D. Savee, D.L. Osborn, C. Lee, S. Vranckx, Z. Wang, F. Qi, R.X. Fernandes, W.H. Green, M.Z. Hadi, C.A. Taatjes, Combust. Flame 161 (2014) 711.

[6] B. Akih-Kumgeh, J.M. Bergthorson, Combustion and Flame 158 (2011) 1877.

[7] D.L. Ginnebaugh, J. Liang, M.Z. Jacobson, Atmospheric Environment 44 (2010) 1192.

[8] M.Z. Jacobson, International Journal of Biotechnology 11 (2009) 14.

[9] M.Z. Jacobson, Journal of Geophysical Research D: Atmospheres 115 (2010).

[10] M.Z. Jacobson, Environmental Science and Technology 41 (2007) 4150.

[11] J.S. Gaffney, N.A. Marley, Atmospheric Environment - Part A General Topics 24 (1990) 3105.

[12] J.S. Gaffney, N.A. Marley, Environmental Science and Technology 35 (2001) 4957.

[13] J.S. Gaffney, N.A. Marley, Atmospheric Environment 43 (2009) 23.

[14] J.S. Gaffney, N.A. Marley, D.R. Blake, Atmospheric Environment 56 (2012) 161.

[15] J.S. Gaffney, N.A. Marley, R.S. Martin, R.W. Dixon, L.G. Reyes, C.J. Popp, Environmental Science and Technology 31 (1998) 3053.

[16] A.S. Raquel, J.J. West, Z. Yuqiang, C.A. Susan, L. Jean-François, T.S. Drew, J.C. William, D. Stig, F. Greg, F. Gerd, W.H. Larry, N. Tatsuya, N. Vaishali, R. Steven, S. Ragnhild, S. Kengo, T. Toshihiko, B. Daniel, C.-S. Philip, C. Irene, M.D. Ruth, E. Veronika, J. Beatrice, I.A. MacKenzie, P. David, R. Mattia, S.S. David, S. Sarah, S. Sophie, Z. Guang, Environmental Research Letters 8 (2013) 034005.

[17] J.T. Herbon, R.K. Hanson, D.M. Golden, C.T. Bowman, Proceedings of the Combustion Institute 29 (2002) 1201.

[18] M. Chai, M. Lu, F. Liang, A. Tzillah, N. Dendramis, L. Watson, Environmental Pollution 178 (2013) 159.

[19] G. Karavalakis, V. Boutsika, S. Stournas, E. Bakeas, Science of The Total Environment 409 (2011) 738.

[20] L.L.N. Guarieiro, P.A.d.P. Pereira, E.A. Torres, G.O. da Rocha, J.B. de Andrade, Atmospheric Environment 42 (2008) 8211.

[21] G. Fontaras, G. Karavalakis, M. Kousoulidou, L. Ntziachristos, E. Bakeas, S. Stournas, Z. Samaras, Environmental Pollution 158 (2010) 2496.

[22] L.L.N. Guarieiro, A.F. de Souza, E.A. Torres, J.B. de Andrade, Atmospheric Environment 43 (2009) 2754.

[23] M.S. Graboski, R.L. McCormick, Progress in Energy and Combustion Science 24 (1998) 125.

[24] P.A. Glaude, O. Herbinet, S. Bax, J. Biet, V. Warth, F. Battin-Leclerc, Combustion and Flame 157 (2010) 2035.

[25] J. Biet, M.H. Hakka, V.r. Warth, P.-A. Glaude, F.d.r. Battin-Leclerc, Energy & Fuels 22 (2008) 2258.

[26] H. Bennadji, P.A. Glaude, L. Coniglio, F. Billaud, Fuel 90 (2011) 3237.

[27] D. Liu, C. Togbé, L.-S. Tran, D. Felsmann, P. Oßwald, P. Nau, J. Koppmann, A. Lackner, P.-A. Glaude, B. Sirjean, R. Fournet, F. Battin-Leclerc, K. Kohse-Höinghaus, Combustion and Flame 161 (2014) 748.

[28] S. Dooley, H.J. Curran, J.M. Simmie, Combustion and Flame 153 (2008) 2.

[29] Reaction Design, CHEMKIN-PRO 15112, San Diego, 2011.

[30] S. Wang, D.F. Davidson, R.K. Hanson, Combustion and Flame 160 (2013) 1930.

[31] C.N. Harward Sr, W.D. Thweatt, R.E. Baren, M.E. Parrish, Spectrochimica Acta Part A: Molecular and Biomolecular Spectroscopy 63 (2006) 970.

[32] L.-H. Xu, X. Jiang, H. Shi, R.M. Lees, A.R.W. McKellar, D.W. Tokaryk, D.R.T. Appadoo, Journal of Molecular Spectroscopy 268 (2011) 136.

[33] Annual Energy Outlook 2014. US Energy Information Administration, 2014.

[34] X. Hu, Q. Yu, J. Liu, N. Sun, Energy 70 (2014) 626.

[35] P. Heil, D. Toporov, M. Förster, R. Kneer, Proceedings of the Combustion Institute 33 (2011) 3407.

[36] A. Di Benedetto, F. Cammarota, V. Di Sarli, E. Salzano, G. Russo, Chemical Engineering Science 84 (2012) 142.

[37] F. Liu, H. Guo, G.J. Smallwood, Combustion and Flame 133 (2003) 495.

[38] A.A. Konnov, I.V. Dyakov, Experimental Thermal and Fluid Science 29 (2005) 901.

[39] A. Mazas, D.A. Lacoste, T. Schuller, Experimental and numerical investigation on the laminar flame speed of CH4/O2 mixtures diluted with CO2 and H2O, ASME Turbo Expo 2010: Power for Land, Sea, and Air. American Society of Mechanical Engineers, 2010, p. 411.

[40] S. de Persis, F. Foucher, L. Pillier, V. Osorio, I. Gökalp, Energy 55 (2013) 1055.

[41] B. Almansour, J. Lopez, L. Thompson, G. Barari, S.S. Vasu, Proc. of the ASME Turbo Expo: GT2015-43355. (2015).

[42] S.S. Vasu, D.F. Davidson, R.K. Hanson, Energy & Fuels 25 (2011) 990.

[43] M. Holton, P. Gokulakrishnan, M. Klassen, R. Roby, G. Jackson, Journal of Engineering for Gas Turbines and Power 132 (2010) 091502.

[44] M. Pelucchi, K.P. Somers, K. Yasunaga, U. Burke, A. Frassoldati, E. Ranzi, H.J. Curran, T. Faravelli, Combustion and Flame 162 (2015) 265.

[45] G.P. Smith, D.M. Golden, M. Frenklach, N.W. Moriarty, B. Eiteneer, M. Goldenberg, C.T. Bowman, R.K. Hanson, S. Song, W.C. Gardiner Jr, GRI-Mech 3.0, 1999.

[46] W.K. Metcalfe, S.M. Burke, S.S. Ahmed, H.J. Curran, International Journal of Chemical Kinetics 45 (2013) 638.

[47] B. Köroğlu, Z. Loparo, J. Nath, R.E. Peale, S.S. Vasu, Journal of Quantitative Spectroscopy and Radiative Transfer 152 (2015) 107.

[48] B. Koroglu, S.S. Vasu, International Journal of Chemical Kinetics (2016).

[49] B. Koroglu, O.M. Pryor, J. Lopez, L. Nash, S.S. Vasu, Combustion and Flame 164 (2016) 152.

[50] B. Koroglu, S.S. Vasu, Chemical Physics Letters in review (2016).

[51] I.R.H. A.G. Gaydon, Reinhold, New York, 1963 (1963).

[52] S.H. Pyun, J. Cho, D.F. Davidson, R.K. Hanson, Measurement Science and Technology 22 (2011).

[53] S.H. Pyun, W. Ren, D.F. Davidson, R.K. Hanson, Fuel 108 (2013) 557.

[54] K.A. Heufer, H. Olivier, Shock Waves 20 (2010) 307.

[55] Z. Hong, D. Davidson, R. Hanson, Shock Waves 19 (2009) 331.

[56] K.Y. Lam, Z. Hong, D.F. Davidson, R.K. Hanson, Proceedings of the Combustion Institute 33 (2011) 251.

[57] H. Mirels, The Physics of Fuilds 6 (1963) 1201.

[58] H. Mirels, AIAA J. 2 (1964) 84.

[59] H. Mirels, The Physics of Fuilds 9 (1966) 1265.

[60] H. Mirels, The Physics of Fuilds 9 (1966) 1907.

[61] H. Mirels, J. Hamman, The Physics of Fuilds 5 (1962) 91.

[62] E.L. Petersen, R.K. Hanson, Shock Waves 10 (2001) 405.

[63] I. Stotz, G. Lamanna, H. Hettrich, B. Weigand, J. Steelant, Review of Scientific Instruments 79 (2008).

[64] R.S. Tranter, K. Brezinsky, D. Fulle, Review of Scientific Instruments 72 (2001) 3046.

[65] D.F. Davidson, D.R. Haylett, R.K. Hanson, Combustion and Flame 155 (2008) 108.

[66] S.S. Vasu, D.F. Davidson, R.K. Hanson, Combustion and Flame 152 (2008) 125.

[67] J.T. Herbon, Mechanical Engineering, Stanford University, Dissertation 2004.

[68] B. Esser, PhD thesis, RWTH Aachen (1991).

[69] Z. Hong, G.A. Pang, S.S. Vasu, D.F. Davidson, R.K. Hanson, Shock Waves 19 (2009) 113.

[70] A E Klingbeil, J B Jeffries, R.K. Hanson, Measurement Science and Technology 17 (2006).

[71] A.E. Klingbeil, J.B. Jeffries, R.K. Hanson, Journal of Quantitative Spectroscopy and Radiative Transfer 107 (2007) 407.

[72] T.J.J. Steven W. Sharpe, Robert L. Sams, Pamela M. Chu, George C. Rhoderick, and Patricia A. Johnson, Applied Spectroscopy 58 (2004) 1452.

[73] L.S. Rothman, I.E. Gordon, Y. Babikov, A. Barbe, D. Chris Benner, P.F. Bernath, M. Birk, L. Bizzocchi, V. Boudon, L.R. Brown, A. Campargue, K. Chance, E.A. Cohen, L.H. Coudert, V.M. Devi, B.J. Drouin, A. Fayt, J.M. Flaud, R.R. Gamache, J.J. Harrison, J.M. Hartmann, C. Hill, J.T. Hodges, D. Jacquemart, A. Jolly, J. Lamouroux, R.J. Le Roy, G. Li, D.A. Long, O.M. Lyulin, C.J. Mackie, S.T. Massie, S. Mikhailenko, H.S.P. Müller, O.V. Naumenko, A.V. Nikitin, J. Orphal, V. Perevalov, A. Perrin, E.R. Polovtseva, C. Richard, M.A.H. Smith, E. Starikova, K. Sung, S. Tashkun, J. Tennyson, G.C. Toon, V.G. Tyuterev, G. Wagner, Journal of Quantitative Spectroscopy and Radiative Transfer 130 (2013) 4.

[74] J. Randell, J.A. Hardy, A.P. Cox, J. Chem. Soc, Faraday Trans. 2 84 (1988) 1199.

[75] H.M. Pickett, The Journal of Chemical Physics 61 (1974) 3954.

[76] G.A. Guirgis, B.R. Drew, T.K. Gounev, J.R. Durig, Spectrochimica Acta Part A: Molecular and Biomolecular Spectroscopy 54 (1998) 123.

[77] J.R. Durig, D.A.C. Compton, A.Q. McArver, The Journal of Chemical Physics 73 (1980) 719.

[78] J.R. Durig, G.A. Guirgis, S. Bell, W.E. Brewer, Journal of Physical Chemistry, A 101 (1997) 9240.

[79] S.G. Frankiss, W. Kynaston, Spectrochimica Acta Part A: Molecular Spectroscopy 28 (1972) 2149.

[80] G. Sbrana, V. Schettino, Journal of Molecular Spectroscopy 33 (1970) 100.

[81] A.V.M. R. E. Peale, C. J. Fredricksen, G. D. Boreman, H. Saxena, G. Braunstein, V. L. Vaks, A. V. Maslovsky, S. D. Nikifirov, Proc. Intl. Symp. Spectral Sensing Research, Bar Harbour ME June 2006 (2006).

[82] E.-t. Es-sebbar, M. Alrefae, A. Farooq, Journal of Quantitative Spectroscopy and Radiative Transfer 133 (2014) 559.

[83] S. Wang, D.F. Davidson, R.K. Hanson, Proceedings of the Combustion Institute in press, available online (2014).

[84] A. Lifshitz, C. Tamburu, A. Suslensky, The Journal of Physical Chemistry 94 (1990) 2966.

[85] P.S. Veloo, P. Dagaut, C. Togbe, G. Dayma, S.M. Sarathy, C.K. Westbrook, F.N. Egolfopoulos, Proceedings of the Combustion Institute 34 (2013) 599.

[86] E.W. Kaiser, International Journal of Chemical Kinetics 15 (1983) 997.

[87] R. Thévenet, A. Mellouki, G. Le Bras, International Journal of Chemical Kinetics 32 (2000) 676.

[88] J.-P. Le Crâne, E. Villenave, M.D. Hurley, T.J. Wallington, J.C. Ball, The Journal of Physical Chemistry A 109 (2005) 11837.

[89] T. Kasper, U. Struckmeier, P. Oßwald, K. Kohse-Höinghaus, Proceedings of the Combustion Institute 32 (2009) 1285.

[90] J. Gong, S. Zhang, Y. Cheng, Z. Huang, C. Tang, J. Zhang, Proceedings of the Combustion Institute (2014).

[91] A.A. Burluka, M. Harker, H. Osman, C.G.W. Sheppard, A.A. Konnov, Fuel 89 (2010) 2864.

[92] K.-Y. Lam, W. Ren, S.H. Pyun, A. Farooq, D.F. Davidson, R.K. Hanson, Proceedings of the Combustion Institute 34 (2013) 607.

[93] B. Koroglu, O. Pryor, J. Lopez, L. Nash, S.S. Vasu, Combustion and flame accepted (2015).

[94] F. Winther, S. Meyer, F.M. Nicolaisen, Journal of Molecular Structure 611 (2002) 9.

[95] J.S. Kwiatkowski, J. Leszczyński, Journal of Molecular Structure: THEOCHEM 342 (1995) 43.

[96] W.F. Arendale, W.H. Fletcher, The Journal of Chemical Physics 26 (1957) 793.

[97] J.T. Sharpe S, Sams R, Chu P, Rhoderick G, Johnson P. Gas, Applied Spectroscopy 58 (2004) 1452.

[98] E. Ranzi, A. Sogaro, P. Gaffuri, G. Pennati, C.K. Westbrook, W.J. Pitz, Combustion and Flame 99 (1994) 201.

[99] K. Yang, C. Zhan, X. Man, L. Guan, Z. Huang, C. Tang, Energy & Fuels 30 (2016) 717.

[100] C.J. Aul, W.K. Metcalfe, S.M. Burke, H.J. Curran, E.L. Petersen, Combustion and Flame 160 (2013) 1153.

[101] A. Lifshitz, K. Scheller, A. Burcat, G.B. Skinner, Combustion and Flame 16 (1971) 311.

[102] N. Lamoureux, C.E. Paillard, V. Vaslier, Shock Waves 11 (2002) 309.

[103] V.P. Zhukov, V.A. Sechenov, A.Y. Starikovskii, Combustion, Explosion, and Shock Waves 39 (2003) 487.

[104] R.A. Strehlow, A. Cohen, The Journal of Chemical Physics 30 (1959) 257.

[105] E.L. Petersen, R.K. Hanson, Shock Waves 15 (2006) 333.

[106] S.S. Vasu, D.F. Davidson, R.K. Hanson, J. Prop. Power 26 (2010) 776.

[107] S.S. Vasu, D.F. Davidson, Z. Hong, V. Vasudevan, R.K. Hanson, Proc. Combust. Inst. 32 (2009) 173.

[108] S.S. Vasu, D.F. Davidson, Z. Hong, R.K. Hanson, Energy & Fuels 23 (2009) 175.

[109] A.V. Joshi, H. Wang, International Journal of Chemical Kinetics 38 (2006) 57.

[110] R. Sur, S. Wang, K. Sun, D.F. Davidson, J.B. Jeffries, R.K. Hanson, Journal of Quantitative Spectroscopy and Radiative Transfer 156 (2015) 80.

[111] M.B. Sajid, T. Javed, A. Farooq, Journal of Quantitative Spectroscopy and Radiative Transfer 155 (2015) 66.

[112] E.-t. Es-sebbar, A. Farooq, Journal of Quantitative Spectroscopy and Radiative Transfer 149 (2014) 241.

[113] O.M. Lyulin, T.M. Petrova, A.M. Solodov, A.A. Solodov, V.I. Perevalov, Journal of Quantitative Spectroscopy and Radiative Transfer 147 (2014) 164.

[114] L. Fissiaux, Q. Delière, G. Blanquet, S. Robert, A.C. Vandaele, M. Lepère, Journal of Molecular Spectroscopy 297 (2014) 35.

[115] M. Alrefae, E.-t. Es-sebbar, A. Farooq, Journal of Molecular Spectroscopy 303 (2014) 8.

[116] S.W. Sharpe, T.J. Johnson, R.L. Sams, P.M. Chu, G.C. Rhoderick, P.A. Johnson, Appied Spectroscopy 58 (2004) 1452.

[117] A.S. Pine, Journal of Quantitative Spectroscopy and Radiative Transfer 57 (1997) 157.

[118] W.G. Mallard, W.C. Gardiner, Journal of Quantitative Spectroscopy and Radiative Transfer 20 (1978) 135.

[119] A.G. Gaydon, I.R. Hurle, Reinhold, New York, 1963 (1963).